Constitutive Modeling of the Finite Deformation Behavior of Membranes Possessing a Triangulated Networked Microstructure

by

Melis Arslan

B.S. Mechanical Engineering
Middle East Technical University, Ankara, Turkey, 2003

SUBMITTED TO THE DEPARTMENT OF MECHANICAL ENGINEERING IN PARTIAL
FULFILLMENT OF THE REQUIREMENTS FOR THE DEGREE OF

MASTER OF SCIENCE IN MECHANICAL ENGINEERING
AT THE
MASSACHUSETTS INSTITUTE OF TECHNOLOGY

[September 2005]
AUGUST 2005

Signature of Author: ______________________________ ____________________
Department of Mechanical Engineering
Aug 5, 2005

Certified by: ____
Professor Mary C. Boyce
Kendall Family Professor of Mechanical Engineering

Accepted by: ____
Professor Lallit Anand, Chairman
Department Committee on Graduate Students

Constitutive Modeling of the Finite Deformation Behavior of Membranes Possessing a Triangulated Networked Microstructure

by

Melis Arslan

Submitted to the Department of Mechanical Engineering
on Aug 5, 2005, in partial fulfillment of the
requirements for the degree of
Master of Science in Mechanical Engineering

ABSTRACT

Many biological, natural and synthetic materials possess a networked or micro-truss-like microstructure. In this thesis work, a general microstructurally-informed continuum level constitutive model of the large stretch behavior of membranes possessing a triangulated network or truss-like structure is developed. As a specific example, a constitutive model of the stress-strain behavior of the red blood cell membrane is developed. The mechanical behavior of the membrane of the red blood cell is governed by two primary microstructural features: the lipid bilayer and the underlying spectrin network. The lipid bilayer is analogous to a 2D fluid in that it resists changes to its planar area, yet poses little resistance to planar shear. A skeletal network of spectrin molecules is crosslinked to the lipid bilayer and provides the shear stiffness of the membrane. The planar triangulated structure of the spectrin network is used to identify a representative volume element (RVE) for the model. A strain energy density function in terms of an arbitrary planar deformation field is proposed using the RVE. Differentiation of the strain energy density function provides expressions for the general multiaxial stress-stretch behavior of the material. The stress-strain behavior of the membrane when subjected to uniaxial and simple shear loading conditions in different directions is given, showing the capabilities of the proposed microstructurally-detailed constitutive modeling approach in capturing the evolving anisotropic nature of the mechanical behavior. The proposed constitutive model also provides a framework to explore the contributions of mechanically-induced unfolding. The force-extension behavior of a single modular macromolecule exhibits a "saw-tooth" pattern due to unfolding giving a sequence of force rise to a peak followed by a load drop. Using the introduced continuum approach together with single molecule force-extension behavior and a transition state model of unfolding, large deformation behavior of two-dimensional networks of biomacromolecules is studied for various loading conditions. The effect of the strain-rate on the mechanical response is investigated.

Thesis Supervisor: Dr. Mary C. Boyce
Title: Kendall Family Professor of Mechanical Engineering

Acknowledgements

I am grateful to my advisor, Professor Mary Boyce, for her guidance and support. I feel fortunate to have her as my mentor, with her drive for perfection, vision and passion for science. I would also like to acknowledge Professor Ali Argon for guiding me into the field of Mechanics and Materials and for his precious advice. I would also like to express my sincere thanks for Dr. Hang Qi for his valuable ideas that were essential for the progress of my research. I would like to express my sincere thanks and appreciation for Mohit Garg for the inspiring discussions we had that were encouraging for the development of my thesis.

This degree is a milestone in my career and while I was going through mild storms, my friends and my family gave me invaluable inspiration and guidance for survival.

First of all, I would like to thank the smartest and coolest people here at MIT.
Sai, thank you for being a great office buddy, and a good friend who is there in ups and downs. I appreciate your valuable advice, and also thank you for proof-reading this document!
Anastassia and Kristin, thank you for showing me a different side of this whole MIT notion and for understanding me in all I go through.
Cathal, thanks for the breaks from work, for making me laugh the whole time and for all the beers! It's always good fun with you. You have the power to make a change.
Angelina, thanks for finding me in Strang's class! I'm glad to have you as my friend and my fashion accomplice!
Mohit, thanks again for your support and patience with my millions of Matlab questions, and also thanks for your friendship.
Adam, thanks for making ISN a more lively place to work.

I would also like to thank my friends in Turkey: Orcun, Narin, and Didem for always reminding me how it feels to be home and that home is a place in Turkey and it always will be so.

I would like to thank the two most vigorous people I have known: my aunt Nazan and my grandma Nazike for always believing in me. I would also like to thank my cousin Ayse for always being there to listen to me enthusiastically and helping me out, no matter what. I would like to thank Ahmet for always being the best friend in the whole world to listen to me, to laugh it out and to show me the light.

Finally and above all, I would like to thank my parents Nurhan and Korkmaz, my sister Selin and my brother Cem for encouraging me in the beginning, in the middle and today. I am so lucky to have you as my family. Thank you for letting me find who I am and celebrating it with me. Without you, all this would never happen.

To Selin & Cem

Table of Contents

Chapter 1

Chapter 2

Chapter 3

Chapter 4

List of Figures

Chapter 1

Background

The structure of cellular solids has been studied since Robert Hooke in the 1660s. A low density cellular solid is a network of solid struts and/or plates which form the edges and/or faces of cells.

There are three kinds of cellular solids as grouped by Gibson, L. J. (Gibson and Ashby, 1997):

- 2-D honeycombs,
- 3-D foam with open cells,
- 3-D foam with closed cells.

Cellular solids are found abundantly in nature. Natural cellular materials are often mechanically efficient. Inspired from natural cellular materials, man-made cellular solids have been constructed and found to have a variety of applications.

In addition to cellular solids, there are also macromolecular networked structures. There is on-going research in the field of determining mechanical responses of these networks by properly incorporating constitutive member behaviors. Some of the example network structures are: *elastomers* and biological networks such as: *auditory outer hair cells, cytoskeleton and soft tissues (collagen).*

This thesis work will focus on developing constitutive models for two-dimensional truss-like networked microstructures and Chapter 1 will give a brief background on cellular solids and macromolecular networked structures.

1.1 Major Areas of Structural Application of Man-Made Cellular Solids

Cellular solids are utilized in many applications due to their mechanical properties:

- Cellular materials are used in *packaging* applications. The material that is used for packaging should be able to absorb energy without subjecting the contents to damaging stresses. The strength of the foam can be changed by changing the relative density of the foam. Also, foams can undergo large compressive strains at a constant stress, resulting in the possibility of absorbing large amounts of energy without generating high stresses. Therefore they are also used in protective structures such as helmets and automobile bumpers. In addition to that, their low densities allow the design of light structures that are easily shipped and handled with lower cost.
- Man-made foams and honeycombs are used as an integral part of *structural materials*, such as sandwich plates. Modern aircraft industry uses honeycomb cores for providing high bending stiffness to the sandwich plates. Sandwich plate technology has other applications where a combination of high stiffness at low weight is important in the design (skis, space vehicles, etc.).
- Closed cell foams are used as the support material for floating structures. Foams are damage tolerant in comparison to flotation chambers, because of their closed cell structure, they retain their *buoyancy* even when they are damaged. They are used as the core of the sandwich structures in the deck and the hull of ships for their role in enhancing the structural stiffness and strength as well as their buoyancy features.

Some examples of the engineering cellular materials are given in Figure 1.1.

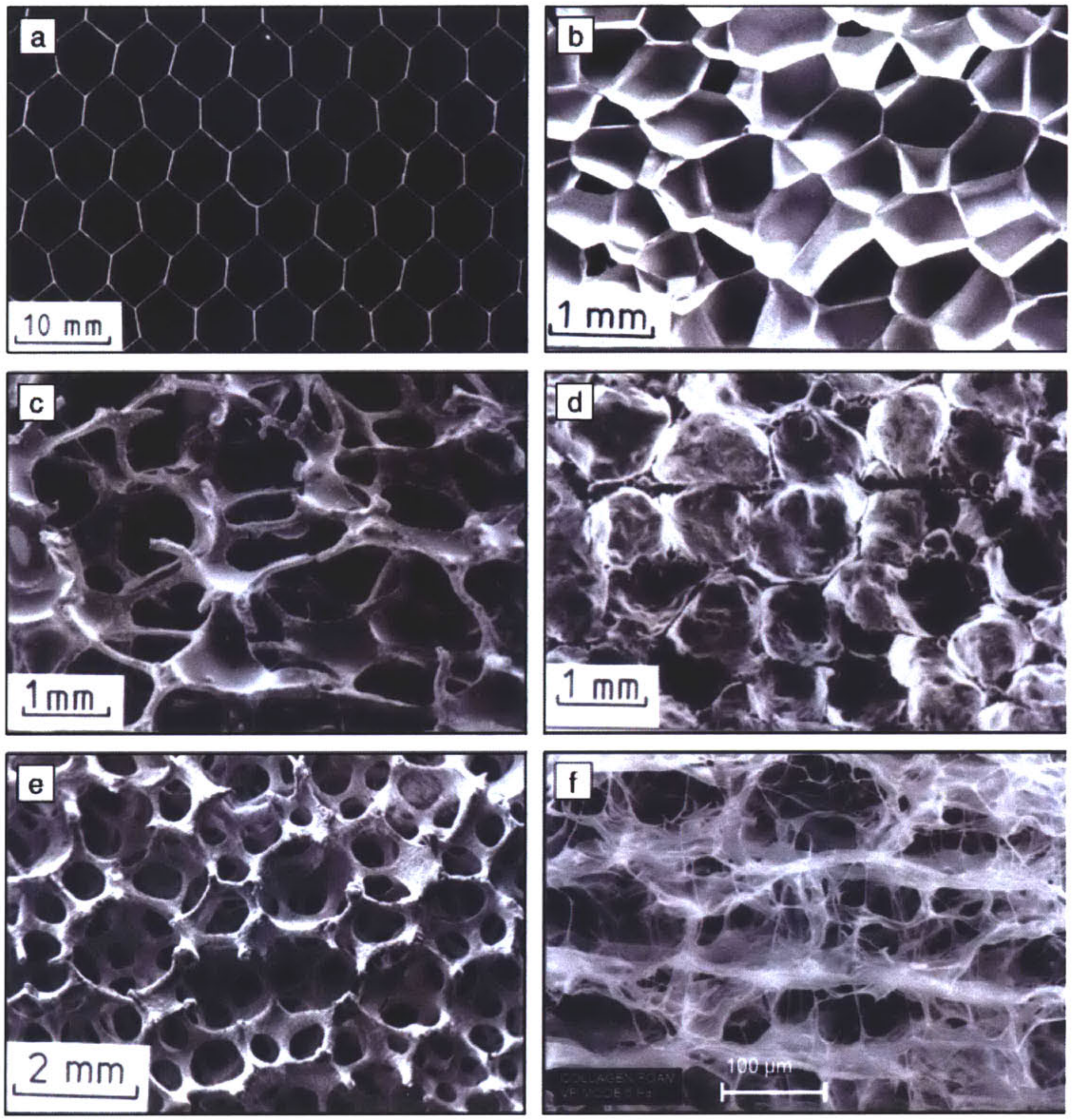

Fig.1.1: *Engineered Cellular Materials:* ***(a)*** *aluminum honeycomb,* ***(b)*** *closed–cell polyethylene foam,* ***(c)*** *open-cell nickel foam,* ***(d)*** *closed-cell glass foam,* ***(e)*** *open-cell zinc foam, and* ***(f)*** *collagen-based porous scaffold used in tissue engineering (Gibson and Ashby, 1997).*

1.2 Natural Cellular Solids

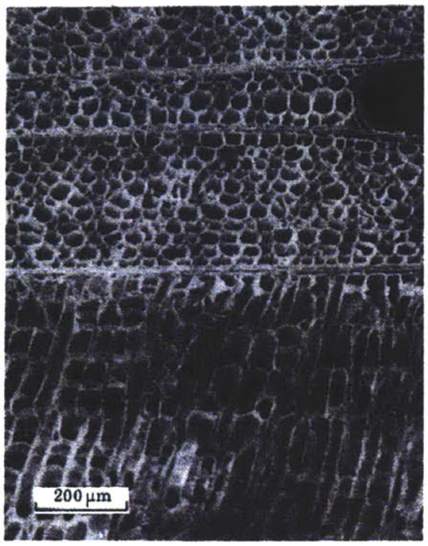

(1.A)

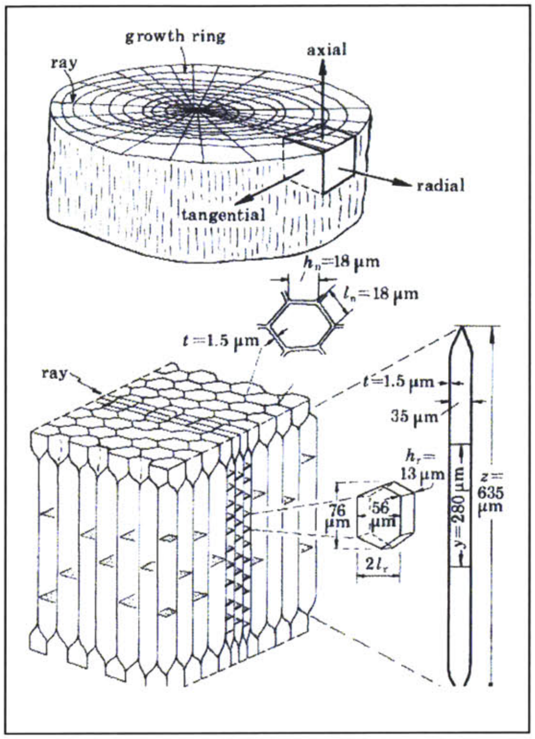

(1.B)

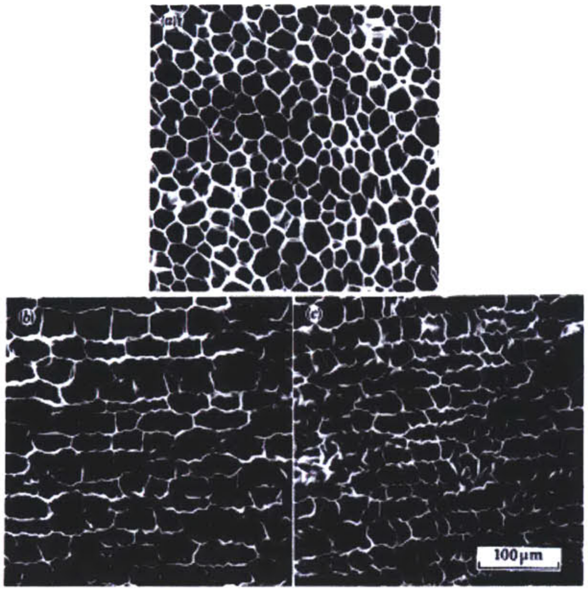

(2.A)

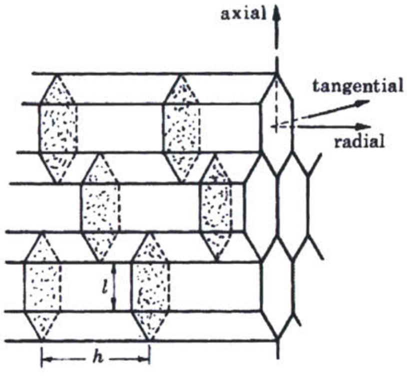

(2.B)

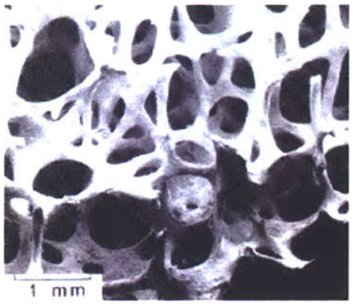

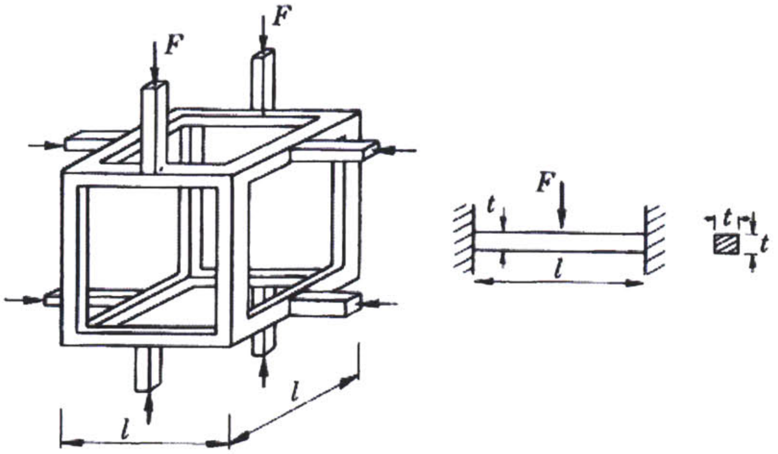

(3.A) *(3.B)*

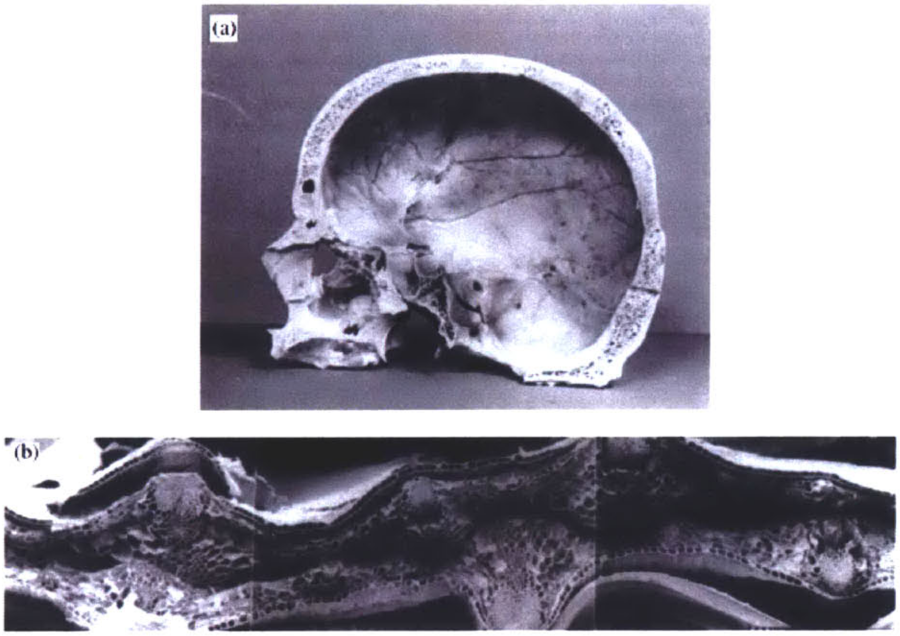

(4)

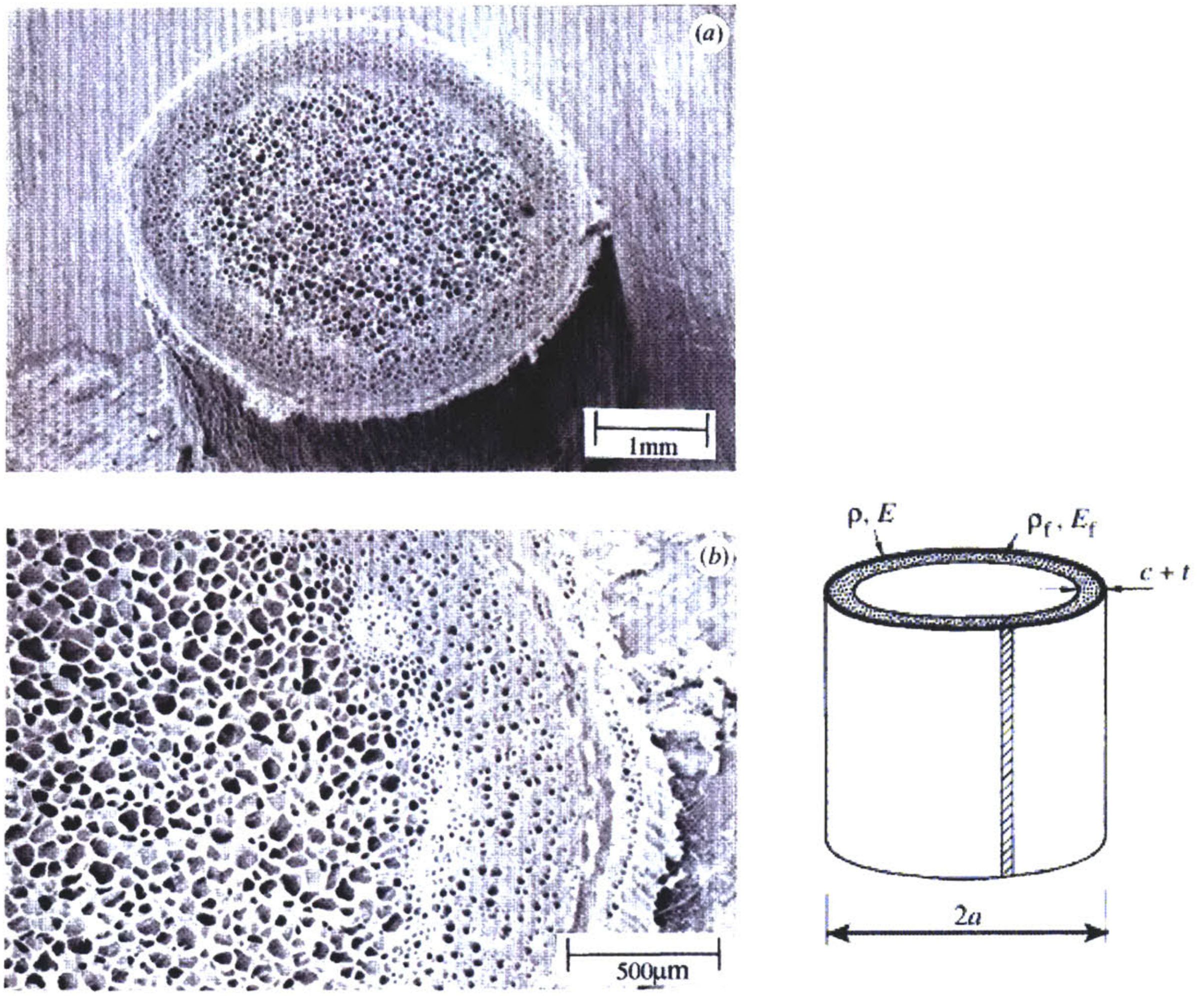

(5.A) ***(5.B)***

Fig.1.2: ***(1.A)*** *Schematic of Balsa Wood,* ***(1.B)*** *Micrograph of Balsa showing axial (top) and tangential (bottom) faces. (Easterling et al., 1982)* ***(2.A)*** *The micrograph of* ***(a)*** *radial,* ***(b)*** *axial and* ***(c)*** *tangential sections of cork. The cell walls are corrugated in the undeformed configuration.* ***(2.B)*** *Schematic of cork cells, hexagonal prisms with 8 faces, 18 edges and 12 vertices. (Gibson et al., 1981)* ***(3.A)*** *Micrograph of the trabecular bone, showing the open-cell structure. (Vajjhala et al., 2000)* ***(3.B)*** *Open cellular structure used to model the open-cell structure of a typical trabecular bone. (Gibson et al., 1982)* ***(4)*** *Natural sandwich structure:* ***(a)*** *skull* ***(b)*** *iris. (Gibson et al., 1988)* ***(5.A)*** *Micrograph of hawthorn showing the cylindrical shell with the inner foam like cells.* ***(5.B)*** *Plant stems are modeled as cylindrical tubes with foam cores. (Gibson et al., 1995)*

In this section some examples of natural cellular solids, their microstructure and mechanical responses as calculated by researchers (Gibson, Ashby, and Easterling) will be discussed.

1.2.1 Wood: Balsa

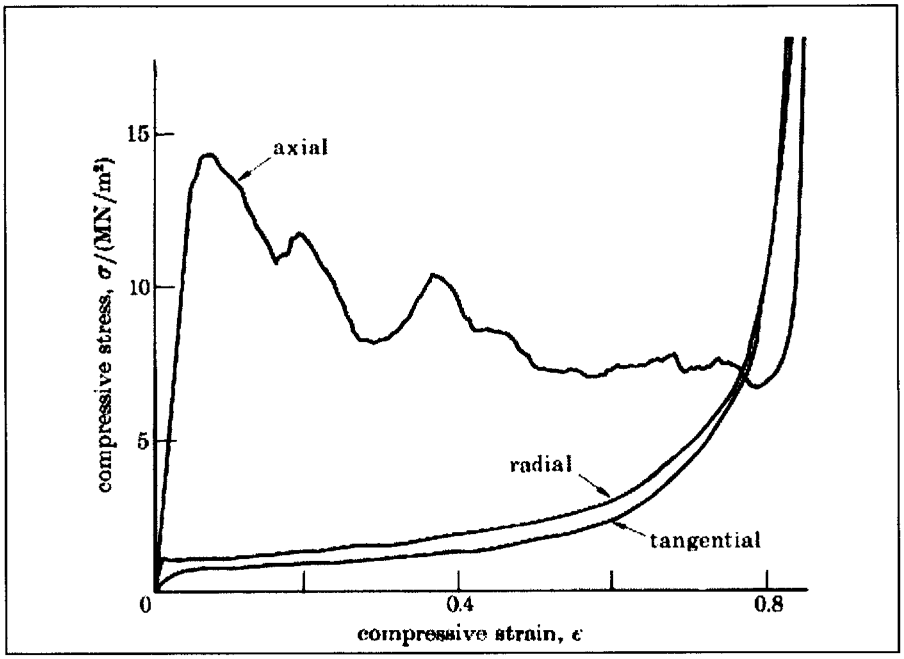

Fig.1.3: *Uniaxial compression stress-strain curve for medium-density balsa, tested in radial, axial and tangential directions (Easterling et al., 1982).*

The stiffness and the strength of a tree in the axial direction is as large as 20 times that of the stiffness and strength of the tree in the radial and tangential directions.

There are three features that characterize the microstructure of wood (Figure 1.2.1):

1. The highly elongated cells which make up the bulk of the wood are called "trancheids" in softwoods and "fibres" in hard woods,
2. The "rays" made up of radial arrays of smaller cells,

3. The "sap channels" which are large cells with thin walls that carry water up the tree.

Cubes from balsa wood were cut parallel to the radial, axial and tangential faces. The compressive stress-strain curves for the samples were recorded (Figure 1.3).

The compression in the tangential and radial directions were found to be almost identical, except from the subtle drop at the yield stress point. This difference is due to how "rays" lie in the direction of compression. Compression in the axial direction is different than in the other directions. The yield stress is much higher in the axial direction and the curve shows a much different trend than in the other directions. The compression plots show the anisotropic structure of the balsa wood.

Easterling et al. (1982) also worked on theoretically modeling the balsa wood, considering the microstructure to be a 2-D honeycomb network. Only in-plane deformation was taken into account, neglecting the stiffening effect of the transverse walls. The Young's modulus of the network was calculated using *simple beam theory* for the cell wall. Using this approach, the modulus in the radial direction was found to be twice the modulus in the tangential direction because of the restraining effect of the "rays" in the radial direction. Another important observation made using the microstructure geometry and beam theory was that, the moduli depend on the third power of the relative density as given in Equation (1.1).

The radial modulus was found to be:

$$E_R = 2\,E_T = E_S\,(\rho/\rho_S)^3, \qquad (1.1)$$

Here E_T is the tangential modulus and E_S is the modulus of the cell wall material.

The theory almost agrees with what was found in the experiments. The axial modulus, E_A, unlike the other two, varies linearly with the relative density. This shows that the anisotropy in wood increases as the relative density decreases.

1.2.2 Cork

The microstructure of cork resembles that of wood (Figure 1.2.2). In the radial view, the cells are hexagonal cells and in tangential and axial views, the cells resemble rectangular bricks. Cubes from cork were cut parallel to the radial, axial and tangential faces. They were deformed in compression and tension. The uniaxial compressive stress-strain curves of the cork cubes is given in Figure 1.4.

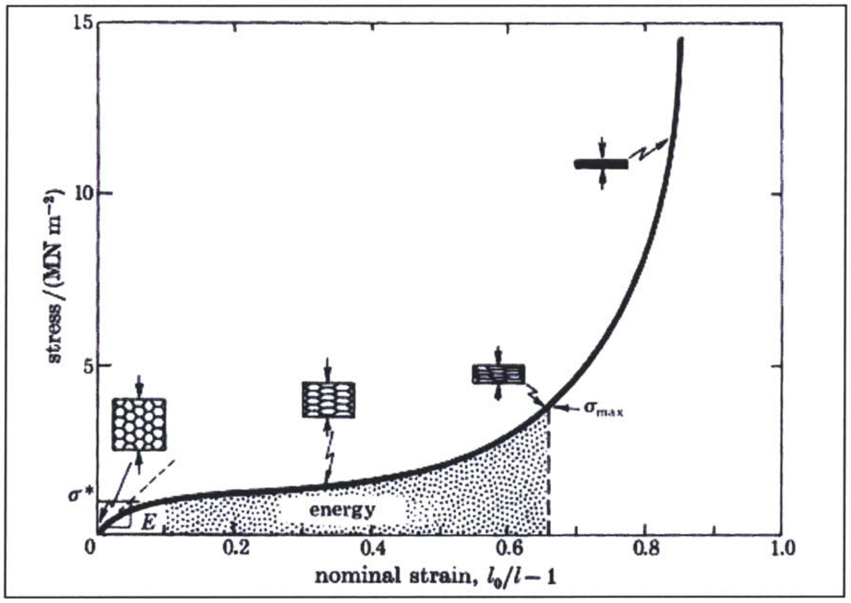

Fig.1.4: *Uniaxial compressive stress-strain curve of cork (Gibson et al, 1981).*

The difference in the response of cork and balsa wood is that cork can be assumed to be isotropic in the plane, because of its rather simple in-plane geometry. When cork deforms, the cell walls buckle and bend. After the maximum stress, σ_{max}, shown in Figure 1.5, the cells completely collapse. The response in the radial direction has been found to be significantly different than the in-plane direction. Tensile deformation along the prism axis unfolds the corrugated cell walls. Compressive deformation folds the corrugations even more.

Gibson et al. (1981) also worked on theoretically modeling cork. They found the relative density from the geometry, in terms of the thickness of the cell walls, length of the hexagonal sides and the height of the unit prisms. The in-plane deformation of 2-D hexagonal cells was analyzed in the same manner that Easterling et al. (1982) analyzed the balsa wood. The material has been treated as a network of connected elastic beams that bend and buckle. The moduli in the axial, E_A, and tangential, E_T directions were found in terms of the relative density, and the modulus of the cell wall material, E_S:

$$E_A = E_T = 0.5\, E_S\, (\rho / \rho_S)^3 . \qquad (1.2)$$

The radial stiffness is found from the stiffness of a corrugated hexagonal prism. The radial modulus was found to be:

$$E_R = 0.70\, E_S\, (\rho / \rho_S) . \qquad (1.3)$$

This equation predicted the modulus to be a factor of 50 higher than that found in the experiments. A possible reason for this difference can be the corrugation of the cell walls in the calculation which had been neglected in the calculations.

Another interesting feature of cork is that compression in the axial direction does not result in any lateral expansion giving a Poisson ratio of zero. The reason behind this is noted to be the corrugation of the cell walls.

1.2.3 Trabecular Bone

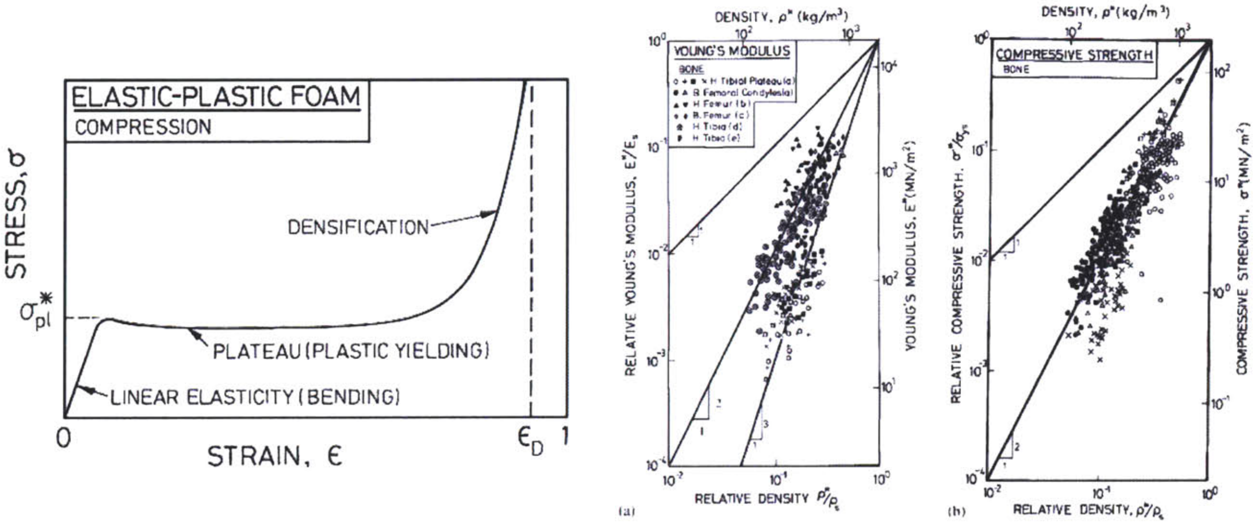

(A) *(B)*

Fig.1.5: ***(A)*** *A schematic stress-strain curve for a foam,* ***(B)*** *Young's moduli of cancellous bone plotted by Ashby and Gibson 1997****(a)****, The compressive strength of cancellous bone* ***(b)*** *plotted by Ashby and Gibson 1997.*

Trabecular (cancellous) bone is commonly found at the center of long bones and consist of regularly ordered plates and struts. Bone grows in response to load such that the density of the bone depends on how much load it is carrying. Also, the orientation of the trabeculae depends on the direction of loading. If loads are equal in all three dimensions, equiaxed cells form in the bone. For lighter loads, rod like open cells form and for higher loads, perforated plates form. Because of this variation in trabecular architecture, there is also a variation in the mechanical responses of different trabecular bones. If the structure contains rod like open cells, then it is modeled as given in Figure 1.2.3.A. For this model the elastic modulus is proportional to the square of the ratio of the relative density:

$$\frac{E^*}{E_S} = C_1\left(\frac{\rho^*}{\rho_S}\right)^2 \qquad (1.4)$$

The basic uniaxial compression stress-strain curve of a trabecular bone is given in Figure 1.5.A.

The typical compression stress-strain curve (Figure 1.5,A) has three parts: (i) linear elastic region, (ii) plateau (plastic yielding and buckling) region, and (iii) densification region. The equiaxed cells first deform in a linear elastic behavior by bending or extension of trabeculae. For a trabecular bone with relative density of $\rho^*/\rho_S = 0.4$, a typical value for the plateau stress is $\sigma_{pl}^* = 37$ MN/m^2 (Hayes and Carter, 1976).

1.2.4 Sandwich Structures: Iris Leaf, Skull

Many natural materials possess a sandwich beam structure. The skull has two outer faces of dense bone separated by trabecular bone. The iris leaf has two outer membrane faces which are similar to fiber composite materials separated by a core of thin walled cells (Figure 1.2.4). The sandwich structure provides the leaf structural stiffness and strength and low mass to keep the upright position in the plant.

Mechanically, sandwich plates are efficient at resisting bending and buckling. The separation of the faces by the foamed core section can dramatically increase the moment of inertia, *I*, of the structure, while only slightly increasing the weight. The deflection of the structure depends on *1/EI*, so that the core of the structure increasing the moment of inertia of the structure results in increased stiffness of the structure.

The bending stiffness, *EI*, of a sandwich beam can be approximated by:

$$(EI)=\frac{E_f btc^2}{2}, \qquad (1.5)$$

where E_f is the Young modulus of the faces, *t* and *c* are the thicknesses of the faces and the core respectively and *b* is the width of the beam. Here it was assumed that the Young's modulus of the core was much smaller than the Young's modulus of the faces. Also the faces are assumed to be much thinner than the core. The core gives rise to shear deflections. The shear stiffness of the core is given as:

$$(AG)=bcG_C. \qquad (1.6)$$

1.2.5 Tubular Structures: Plant Stems, Animal Quills

The tube structure with the foam core (Figure 1.2.5, A) provides the stem of a plant a high resistance against buckling failure due to the weight of the plant. The plant stems resist the bending moment from their own mass as well as that from applied loads. Plant stems were modeled by Gibson et al. (1995) as axisymmetric, cylindrical tubes with foam cores (Figure 1.2.5,B).

Using the axisymmetric cylinder model for plant stems, under uniaxial compression the shell with a foam core has a higher resistance to both global and local buckling than a hollow shell due to the enhanced global bending resistance and due to the foam core also providing a resistance against local buckling of the outer shell. The shell with a foam core was found to have a higher buckling resistance for thin and thick shells (Figure 1.6).

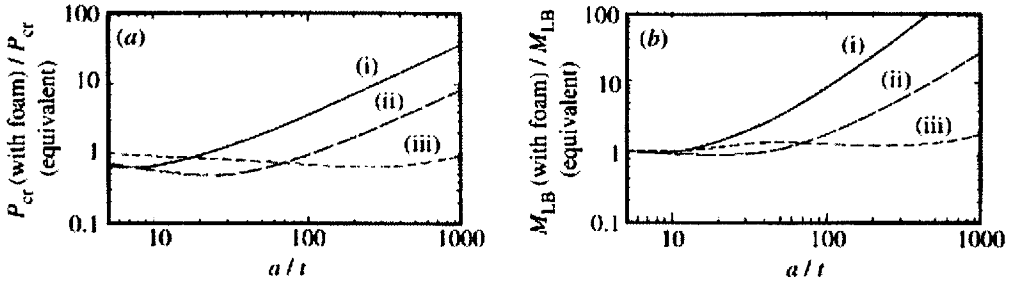

(A) (B)

Fig.1.6: *The buckling resistance of the foam core cylindrical shell to that of the hollow cylindrical shell **(A)** for uniaxial compression, **(B)** for bending; the relative density of the foam is decreased as: **(i)**, **(ii)**, **(iii)** Gibson et al. (1995).*

Experiments have also been conducted to compare with the theoretical model. Silicon rubber cylindrical shells with and without foam cores were tested under uniaxial compression and four point bending. The experimental results agreed with the theoretical results.

1.3 Man- Made Cellular Materials

In addition to natural cellular materials, there are also man-made cellular materials. There is on-going research in the field of man-made cellular materials (Ashby et al., 2000, Brittain et al., 2001, Chiras et al., 2002, Evans et al., 2001, Wallach and Gibson, 2001, Wicks and Hutchinson, 2001).

In this section we will look at some of the approaches taken to model truss-structured materials recently being developed and used in applications that typically had used foams and/or honeycomb cores. These structures are not only light-weight, but also possess high stiffness and strength due to the constitutive members' ability to carry axial loads and the tailoring of the truss geometry to optimize the positioning for efficient utilization of the member stiffness and strength contribution to the structure as a whole.

There are three methods to model cellular materials:

i. Dimensional arguments,
ii. Analysis using repeating unit cells,
iii. Numerical micromechanical modeling using finite element methods.

Wallach and Gibson, 2001 used the approaches: (ii) and (iii) to model materials with periodic, three-dimensional truss-like structures (Figure 1.7).

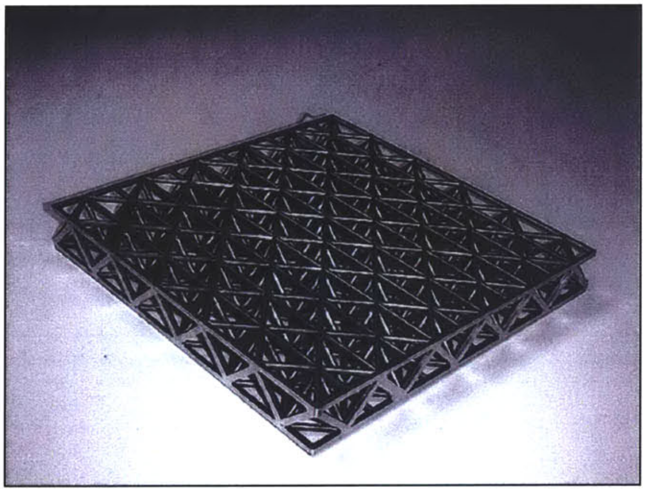

Fig.1.7: *Photograph of a 3D truss structure made from an aluminum casting alloy (Wallach and Gibson, 2001).*

They worked on a millimetric periodic array of an aluminum alloy. The mechanical response of an infinite plane of truss materials was calculated from that of the unit cell. A unit cell isolates a repeating structural unit of the material and accounts for the influence of its neighbours through proper periodic and symmetric boundary conditions (Figure 1.8).

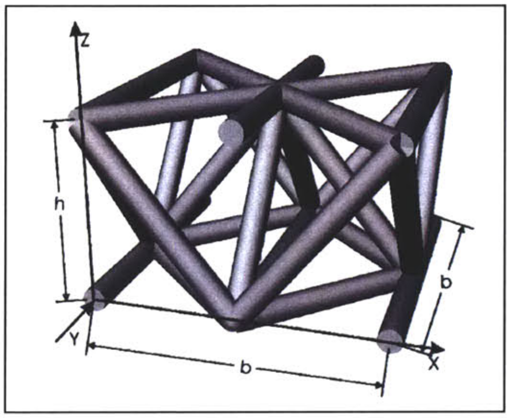

Fig.1.8: *The sketch of the unit cell used for the infinite plane of truss materials. The triangles are isosceles right triangles with the inclined members at* 45^0 *to the horizontal member. Here, h/b is the aspect ratio of the unit cell (Wallach and Gibson, 2001).*

Wallach and Gibson (2001)'s analysis of uniaxial tension included two steps of numerical simulations. They conducted numerical analysis using MATLAB for the case of a linear-elastic material. And then studied the non-linear response at large deformations employing a finite-element code: ABAQUS.

In addition to looking at the infinite number of cells in the x and y planes, they also looked at finite number of cells' responses with respect to an infinite sized array of unit cells. The truss elements in the structure carry axial loads, the effective Young's moduli and shear moduli are noted to vary linearly with the relative density as given in Equation (1.7).

$$E^*/E_s = C_1\,(\rho^*/\rho_s),$$

$$G^*/G_s = C_2\,(\rho^*/\rho_s). \qquad (1.7)$$

The stress-strain curves for a network made of several cells under compression was plotted (Figure 1.9,A.).

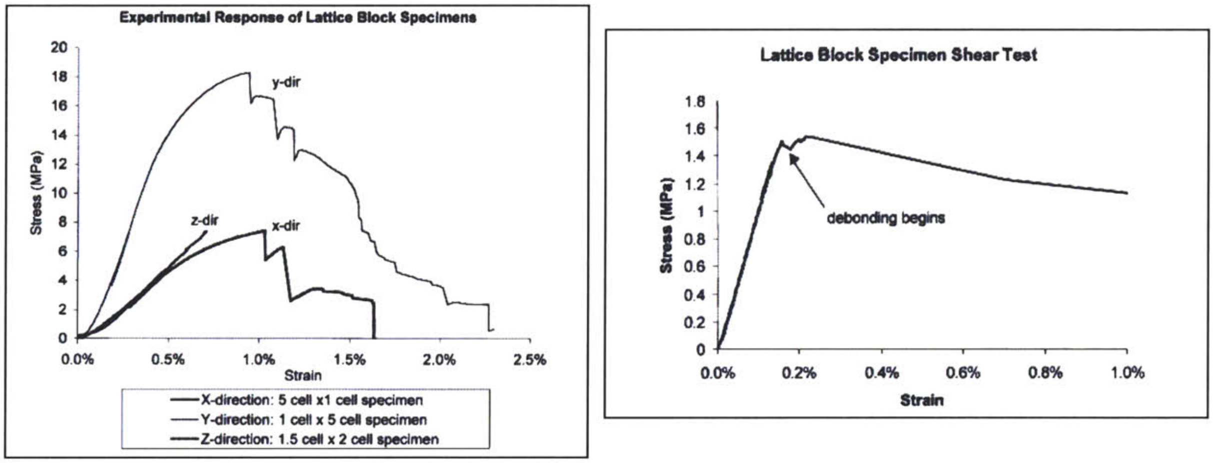

(A) *(B)*

Fig.1.9: ***(A)*** *Measured compressive stress-strain behavior for loading the truss material in x, y, z directions,* ***(B)*** *Measured shear stress-strain behavior for loading the truss material in x-z plane.*

In the x and z directions, the initial slope was found to be the same. In the z direction, the curve has a linear trend up until a strain about 0.7%, and because of the measuring difficulties, there were two tests they carried out which determined the failure stress and the linear trend up to that point. In the x direction, when the members failed there was a sudden drop in stress. The failure in the y direction was because of fracture in the top and bottom face members and buckling in the core members. The buckling is seen in the Figure 1.13 for the y direction.

The measured shear stress- strain curve gave an initial shear modulus of 1.17 GPa. Because of the debonding (Figure 1.14) of the specimen from the aluminum plates, the failure in shear was not measured. The measured moduli were compared to the calculation. Figure 1.10 gives the comparison for loading in the x direction. The discrepancy between experiment and model for E_x, E_y, E_z and G_{xz} has been found to be -15%, +3%, +7% and -27%, respectively.

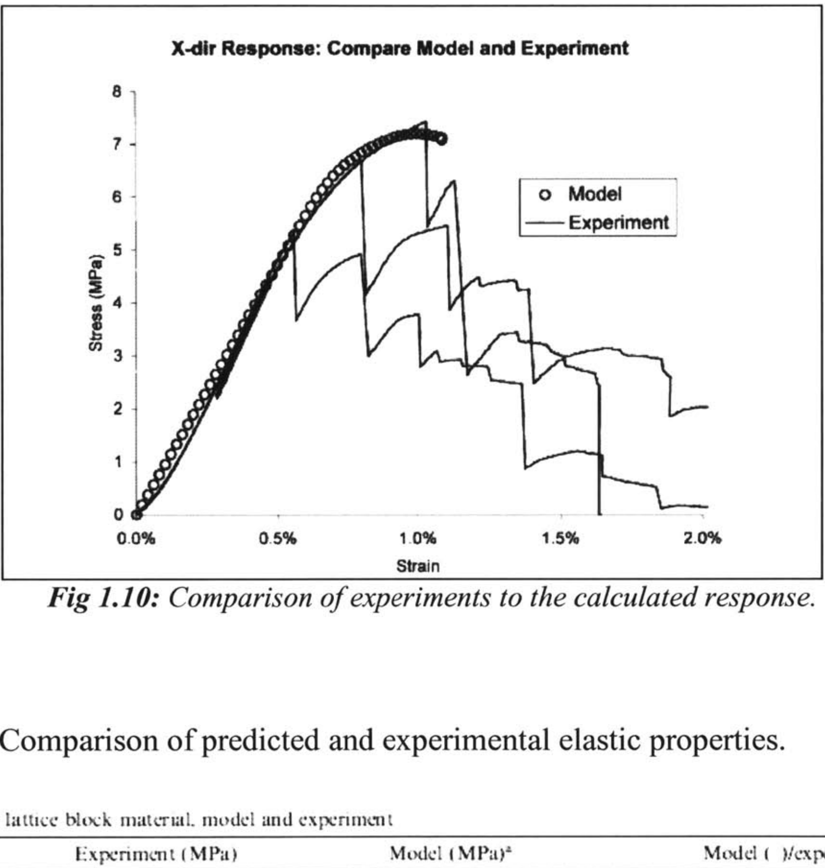

Fig 1.10: Comparison of experiments to the calculated response.

Table 1.1: Comparison of predicted and experimental elastic properties.

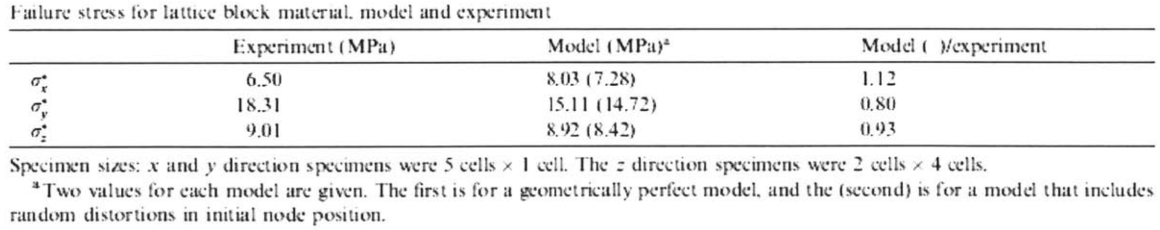

Failure stress for lattice block material, model and experiment

	Experiment (MPa)	Model (MPa)[a]	Model ( )/experiment
σ_x^*	6.50	8.03 (7.28)	1.12
σ_y^*	18.31	15.11 (14.72)	0.80
σ_z^*	9.01	8.92 (8.42)	0.93

Specimen sizes: *x* and *y* direction specimens were 5 cells × 1 cell. The *z* direction specimens were 2 cells × 4 cells.

[a] Two values for each model are given. The first is for a geometrically perfect model, and the (second) is for a model that includes random distortions in initial node position.

Ultra Light Structures

Minimum weight designs are identified by the failure modes. For flat panels subject to bending, honeycomb core panels are always found to be lighter for the same performance (Figure 1.11.A). However, foam core sandwich structures have superior performances in specific cases, because of their isotropic nature when compared with the honeycomb structures. Examples of designs that require that specific loads be supported at minimum weight are given in Figure 1.11.B.

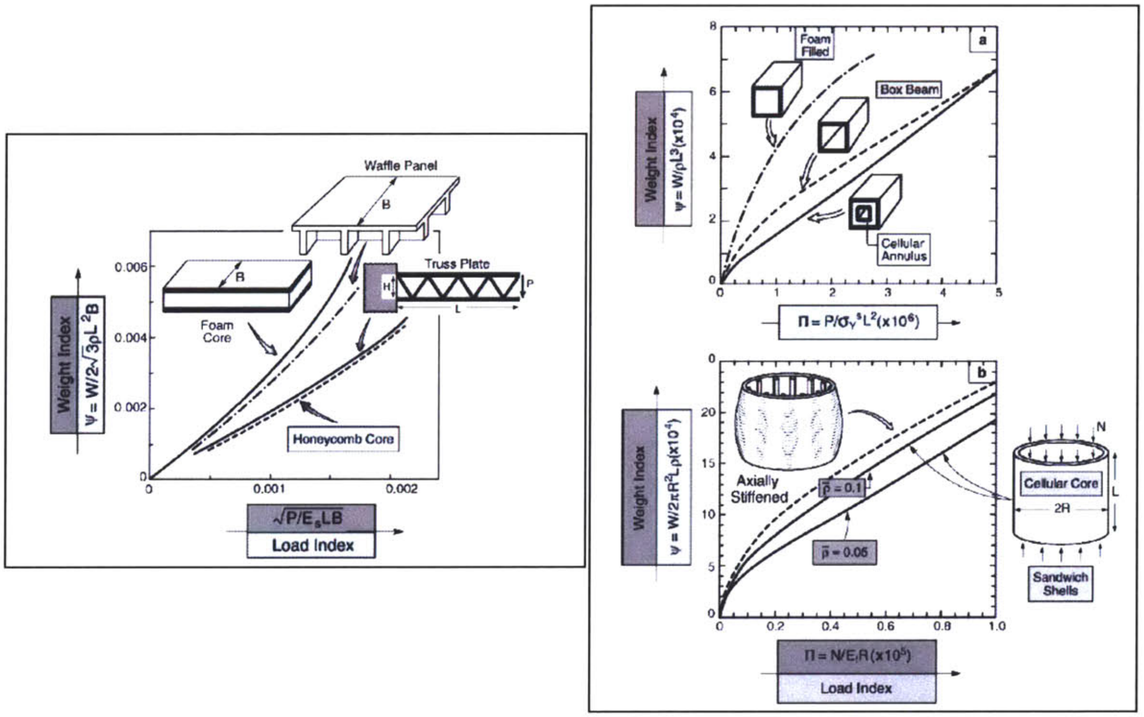

(A) ***(B)***

Fig.1.11: ***(A)*** *Comparison of four core configurations. The minimum weight as a function of collapse load P.* ***(B)*** *Minimum weights is compared for axially compressed configurations as a function of load index.* ***(a)*** *Annual design has the lowest weight.* ***(b)*** *Sandwich structures have lower weight than axially stiffened structures. (Evans et al., 2001)*

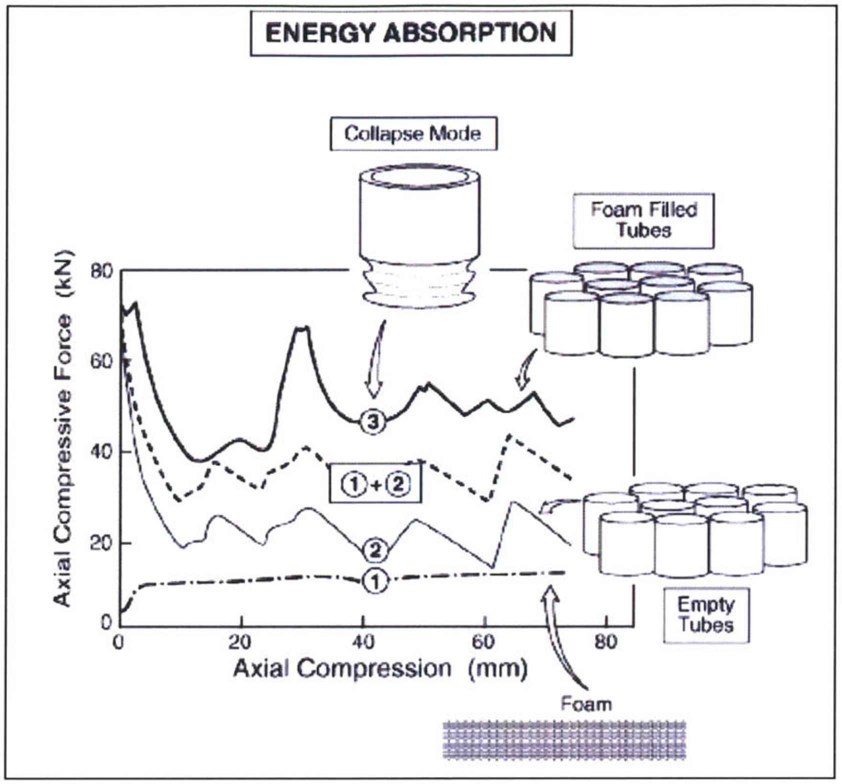

Fig.1.12: *Crushing force as a function of axial compression for foams, empty tubes and tubes with foam cores.(1)+(2) refers to the expected experimental result from crushing the tubes with foam cores (Evans et al., 2001).*

High Energy Absorption

Cellular materials are noted to have the highest energy absorption per unit mass of any material as given by Ashby et al. (2000). The isotropy of the foam is a superior feature for impacts. Figure 1.12 gives the crushing force vs. axial compression for empty tubes and tubes filled with foam cores. The result is interesting in the sense, Evans et al. (2001) showed that the addition of the responses of the empty tubes and the foam itself gives rise to lower crushing force than the actual case they found from the experiments when they compressed the tubes with foam cores, They explained this phenomenon as a "synergistic effect". This is analogous to the plant stems in the sense of the foam core acting to increase the global bending stiffness and buckling loads as well as the local buckling conditions.

1.4 Fabrication of photonic crystals with fcc, bcc and cubic symmetries using interference lithography

Interference litography can be used to fabricate 3D nanoscale structures which are analogous to truss-like mechanical structures. They have the potential to provide high stiffness, strength, as well as low density and enhanced energy absorption properties. The periodic microstructure is generated by interfering four coplanar or noncoplanar laser beams in a film of photoresist (Campbell et al., 2000, Ullal et al., 2004, Yang et al., 2005). Photolithography is the process of applying a pattern to a substrate material. The material can be anything of interest, typically it is semiconductor material either in wafer or piece form. The lithography process consists of several key steps:

- Mask fabrication
- Photoresist application
- Mask alignment
- Development

Thomas' Group Work

The Thomas Group (MIT, Materials Science) constructed 2D and 3D periodic structures in polymeric thin films using interference lithography. 2D and 3D nanotrusses were fabricated using multibeam holographic interference lithography (Figure 1.13).

Fabrication Procedure

1. Making the Solution (Solution: Raw SU8 + initiator + base + solvent),
2. Pre-baking: to evaporate the solvent,
3. Exposure: to produce the interference pattern on the epoxy based photoresist (the interference of three of four equal amplitude beams of visible light from a continuous wave laser),
4. Post baking: to move the polymer for reaction and to crosslink,
5. Development: washing away (in PGMEA-colorless liquid) unexposed parts,
6. Drying.

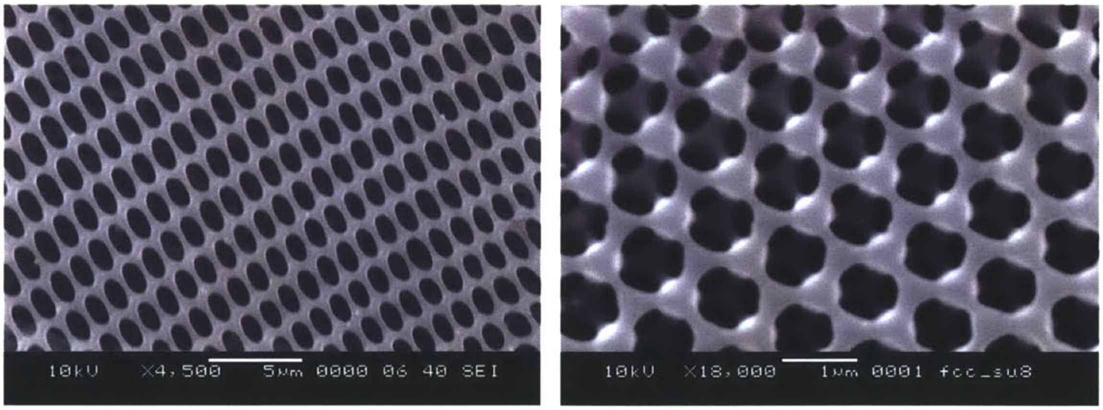

(A) ***(B)***

Fig.1.13: ***(A)*** *2-D and* ***(B)*** *3-D periodic nano structures fabricated from holographic interference lithography (Choi et al., 2005).*

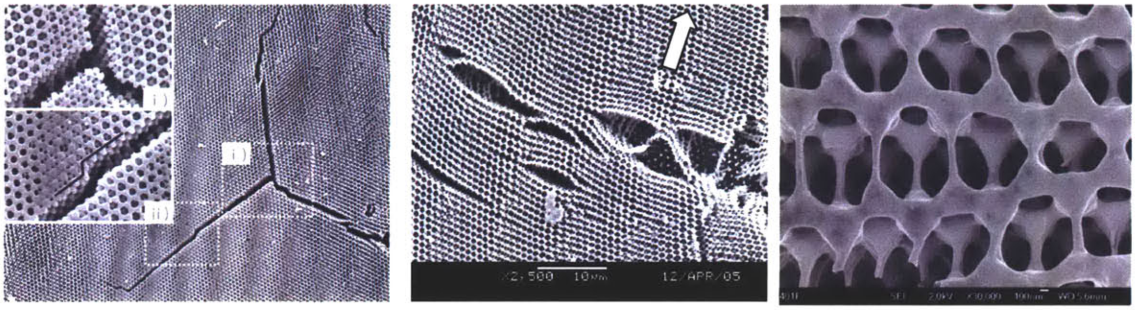

(A) ***(B)*** ***(C)***

Fig. 1.14: *SEM images showing the deformation of SU8:* ***(A)*** *cracks propagating at* 120^o*,* ***(B)*** *large openings with bent ligaments bridging opposite sides and* ***(C)*** *overstretched and fractured beams in the vicinity of crack tip showing plasticity in the top and sub-layer struts. (Choi et al., 2005).*

Although the mechanical behavior of the micro truss structured materials have not yet been quantified, the materials have been deformed (however forces and strains were not measurable). The "struts" of the microtruss are observed to undergo large strain plastic deformation. The extensive deformability of these struts may be a length scale effect (the struts are *~150 nm* in diameter) imparting ductility to the SU8 (which is brittle at the macro-level, Figure 1.14) or it maybe a lower cure than thought.

1.5 Macromolecular Networked Structures

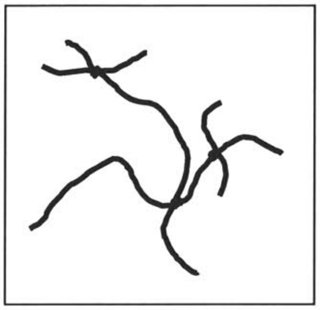

(1)

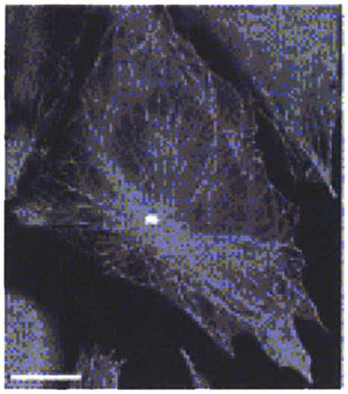

(2)

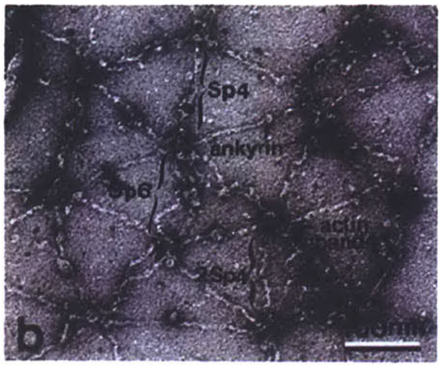

(3)

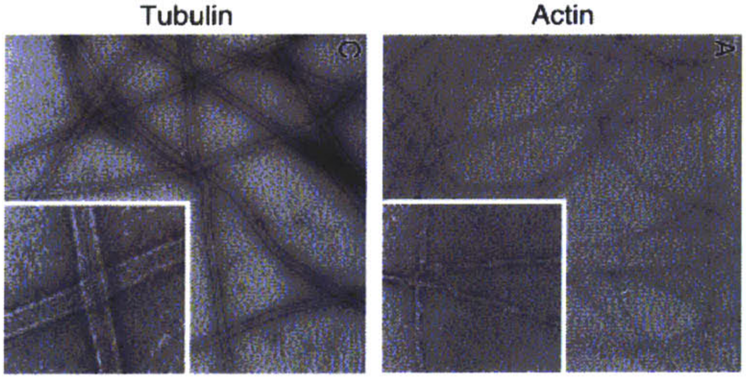

(4)

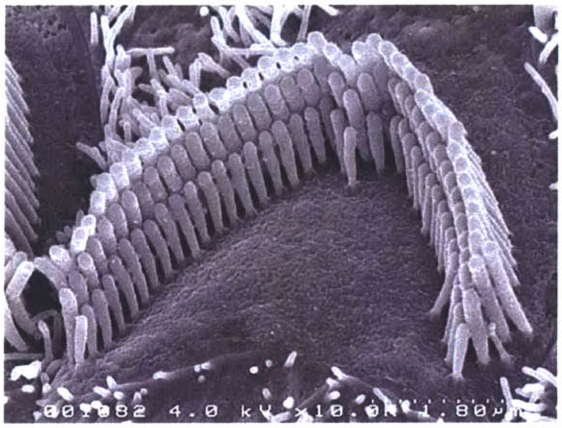

(5)

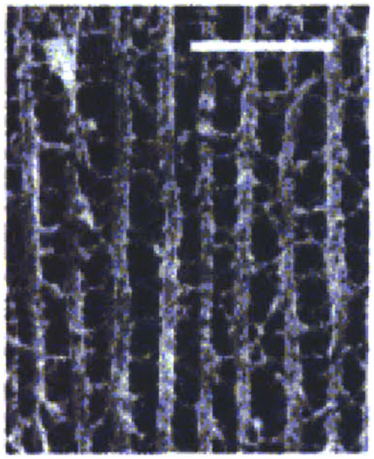

(6)

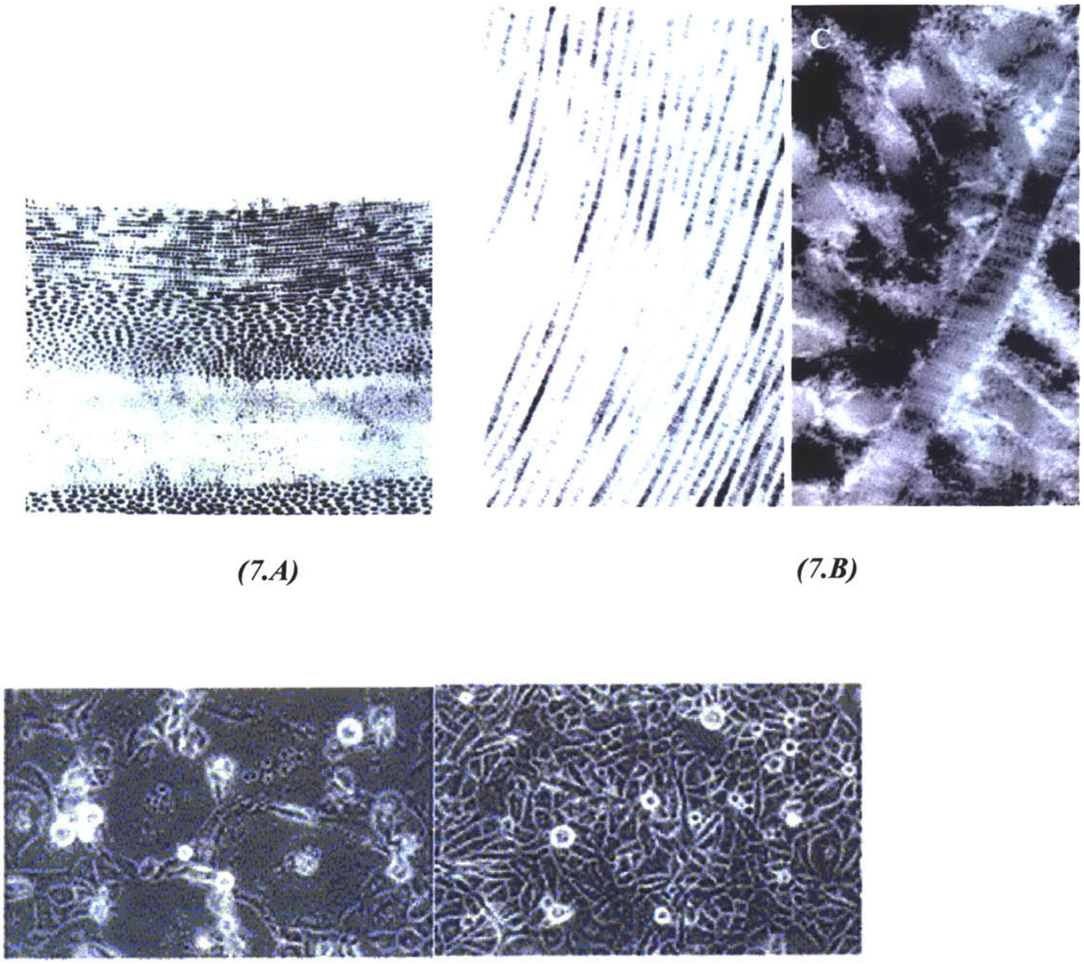

(7.A) *(7.B)*

(8)

Fig. 1.15: ***(1)*** *A schematic of an elastomer microstructure showing the long-chain molecules and the crosslinks that bind them,* ***(2)*** *The array of microtubules in a fibroblast. The bar is 10μm.(Boal, 2003) ,* ***(3)*** *2-D network of spectrin protein in the red blood cell membrane (Liu et al., 1987),* ***(4)*** *A micrograph of the rabbit muscle actin and tubulin (Nakamura, 2001),* ***(5)*** *Single hair cell bundle in the inner ear (Furness and Hackney, 1990),* ***(6)*** *Crosslinked filaments inside a nerve cell from a frog. The bar is 0.1 μm. (Boal, 2003),* ***(7.A)*** *Arrangement of collagen fibrils in corneal stroma (Miller and Benedek, 1973),* ***(7.B)*** *Collagen type I fibril (left) in tendon and type II fibril (right) in cartilage (Gelse et al., 2003),* ***(8)*** *A micrograph of infected mouse keratinocytes (Roper et al., 2001).*

In addition to cellular solids which can be considered as networks of solid struts and walls, there are also macromolecular networked structures. Elastomers (Figure 1.15.1) are the basic family of these type of microstructures. The presence of long chain molecules with freely jointed links and weak secondary forces between the molecules are the basic characteristics of rubbers (Treloar, 1958 and Flory, 1953). Crosslinking of the molecules at junctions along their lengths form a three dimensional network.

Biological networks are another class of molecular networked structures. There exist many examples of these structures in nature (Figure 1.15.2-8). One of the examples of two dimensional networks in the animal cell is the spectrin network (Figure 1.15.3). The spectrin network is a 2-D triangulated network of protein molecules; micrographs usually show the stretched form and make the six-fold symmetry clear. There are also three-fold coordinated biological networks, such as the auditory outer hair cell (Figure 1.15.5).

In addition to the 2-D networks existing in the cell, there are also 3-D networks in the cell. For example, keratin intermediate filaments (Figure 1.15.8) extend through the cytoplasm and are attached to the cell nucleus and plasma membrane (Boal, 2003). Actin network is another example of the 3-D networks present in the cytoskeleton where the actin molecules are crosslinked by other protein filaments to form networks (Figure 1.15.4). There is also a microtubule network in the cytoskeleton, where the microtubules are very stiff elements. Figure 1.15.2 gives the microstructure of microtubules which are polymeric protein filaments of tubulin monomers present in the cytoskeleton (Boal, 2003). Some soft tissues have networked structures as well. An example of this class is the connective tissue which contains collagen, the fibrous protein (Figure 1.15.7). Collagen is the most abundant protein in animals, mainly supporting skin, tendon, bone, cartilage and connective tissue.

The following chapters in this thesis will concentrate on deriving a constitutive model for the two dimensional macromolecular triangulated networked structures. Specifically the spectrin network will be studied in the following chapters.

In Chapter 2, basic red blood cell membrane properties and the importance of modeling the spectrin network (which resembles a two dimensional triangulated network) in investigating the mechanical properties of the red blood cell membrane will be discussed. Previous work on the constitutive modeling of the mechanical properties of the red blood cell membrane and the previous approaches in modeling triangulated nets will be studied. Then the chapter will mainly concentrate on the proposed general continuum level constitutive model of the large stretch behavior of the red blood cell membrane that directly incorporates the microstructure of the spectrin network.

In Chapter 3, the previous theoretical and experimental studies on the unfolding of single molecules possessing folded domains will be given. Then later in the chapter, using the introduced continuum approach and statistical mechanics based models of the chain force-extension behavior together with a transition state model of unfolding, a constitutive model for the membrane stress-stretch behavior will be constructed.

Chapter 4 will provide a summary of the proposed model and will elaborate on possible applications of the same methodology to explore additional complexities in various other microstructures. The methodology will further be extended to investigate three-dimensional structures.

Chapter 2

Constitutive Modeling of the Stress- Stretch Behavior of the Triangulated Spectrin Network

2.1 Introduction

In this chapter, a general continuum level constitutive model of the large stretch behavior of the red blood cell membrane that directly incorporates the microstructure of the spectrin network is developed. The triangulated structure of the spectrin network is used to identify a representative volume element (RVE) for the model. A strain energy density function in terms of an arbitrary planar deformation field is constructed using the RVE together with various representations of the underlying molecular chain force-extension behaviors. Expressions for the nonlinear finite deformation stress-strain behavior of the membrane are obtained by proper differentiation of the strain energy function. The stress-strain behavior of the membrane when subjected to tensile and to simple shear loading in different directions are obtained, demonstrating the capabilities of the proposed microstructurally-detailed constitutive modeling approach in capturing the small to large strain nonlinear, anisotropic mechanical behavior. The sources of nonlinearity and evolving anisotropy are delineated by simultaneous monitoring of the evolution in microstructure including chain extensions, forces and orientations as a function of macroscopic stretch.

2.2 Red Blood Cell Membrane Properties

Human red blood cells are disc-shaped. Red blood cells experience deformation when they travel through the circulatory system. These deformations can be quite large especially when the red blood cells enter a capillary, where the human red blood cell diameter is approximately 8 μm, while the diameter of a capillary is around 3 μm. In the capillary blood vessels, the blood cell shape becomes bullet-like (Figure 2.1) (Fung, 1993).

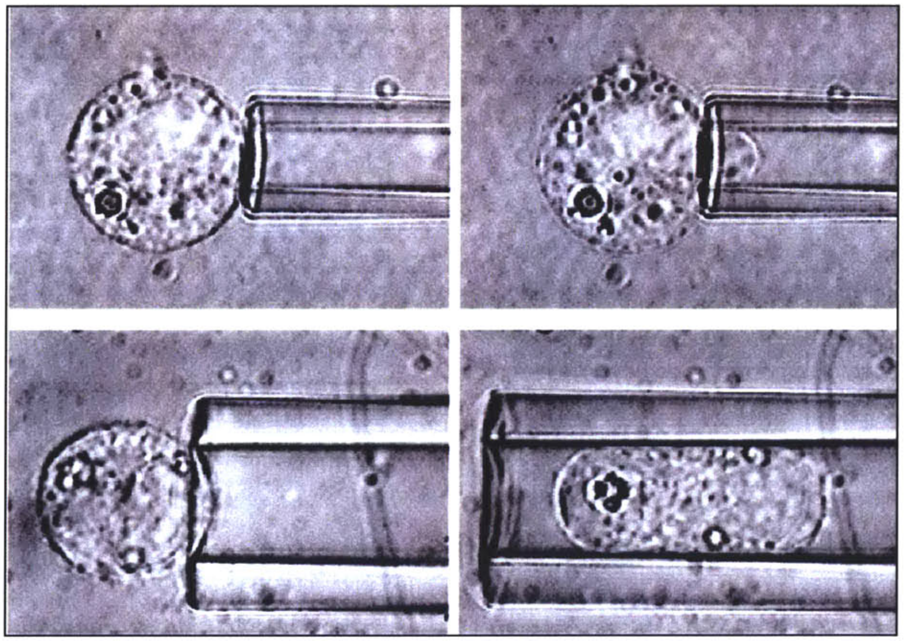

Fig. 2.1: *The video-micrograph of a red blood cell drawn into a pipette (Jones et al., 1999).*

In spite of the large deformations that the Red Blood Cells go through, they recover their shape once the applied load is released. The shear modulus of the cell membrane should be small enough to accommodate the shape change but should be large enough so that the membrane will recover its shape.

To model the elastic response of the membrane, one should take a look at the components of the membrane that provide the mechanical responses.

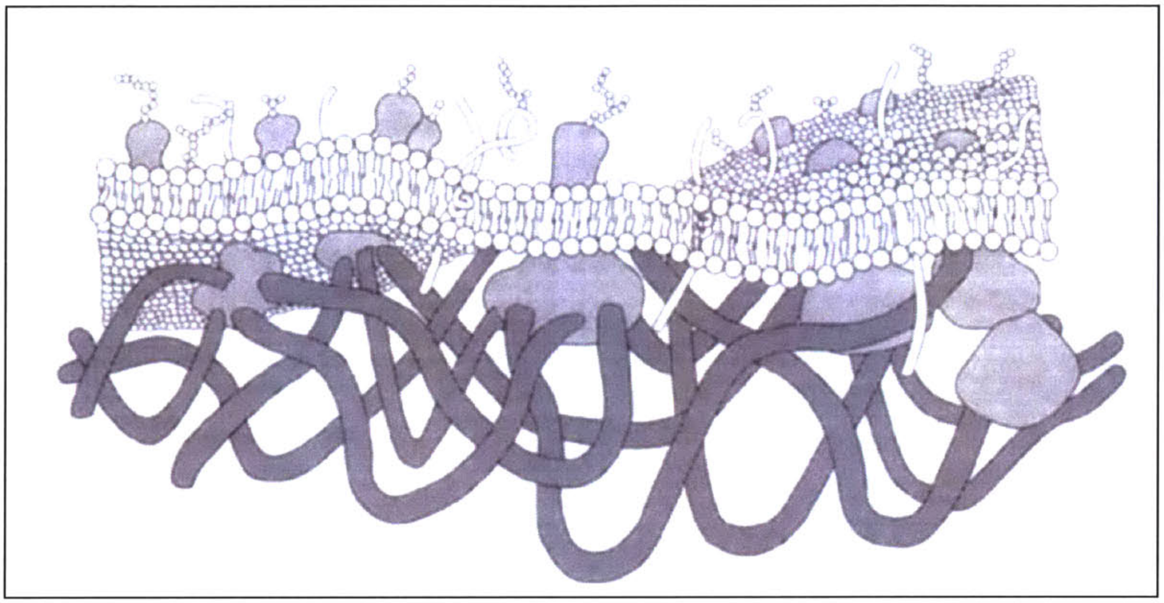

Fig. 2.2: *The sketch of the lipid bilayer and the underlying spectrin network (Mohandas and Evans, 1994).*

The interior contents of a cell excluding the nucleus is called *cytoplasm*. The fluid component of the cytoplasm is called *cytosol*. The fluid-like membrane that bounds the cell is called *the lipid bilayer*. *Cytoskeleton* lies beneath the lipid bilayer and, in most cells, also throughout the cytoplasm and is attached to the bilayer. The cytoskeleton is the filamentous network composed of *microtubules, intermediate filaments, actin* and *spectrin* (Figure 2.3). In the red blood cell, a network of spectrin molecules lies tangential to the bilayer and is connected to the bilayer through transmembrane proteins. The spectrin network is constituted with α- and β- protein chains. The α and β protein chains form a heterodimer; 2 heterodimers combining back-to-back to form a spectrin tetramer

(Figure 2.4). The contour length of the heterodimer is 100nm while the heterodimers associate head to head to form tetramers of contour length of 200nm (Mohandas and Evans, 1994).

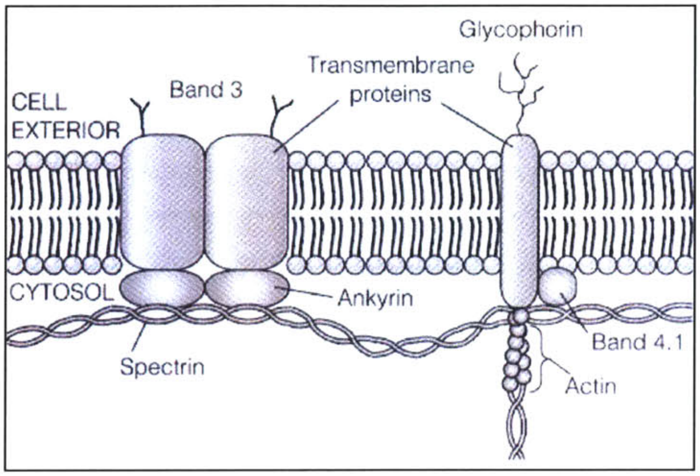

Fig. 2.3: *A picture of the lipid bilayer and the protein network attached to it (Becker et al., 2000).*

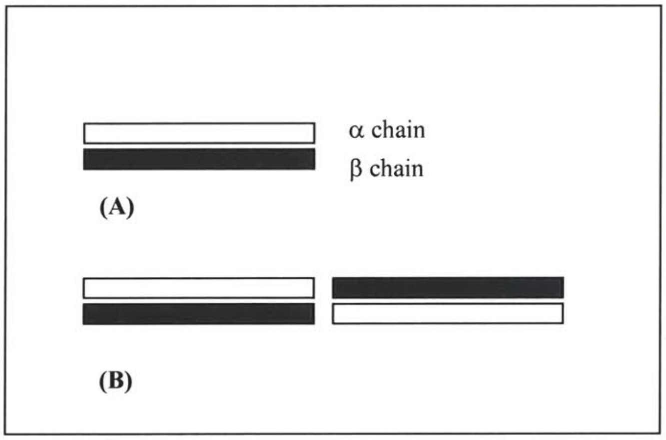

Fig. 2.4: *Sketch of* ***(A)*** *spectrin heterodimer, composed of an* α *and a* β *polymer chain,* ***(B)*** *2 heterodimers back to back form a spectrin tetramer.*

The lipid bilayer is analogous to a two-dimensional fluid in that it resists changes to its planar area, yet poses little resistance to planar shear as noted as early as 1948 by Ponder (Ponder, 1948). A skeletal network of spectrin molecules is crosslinked to the lipid bilayer and provides the shear stiffness of the membrane. Experiments have documented a membrane planar area modulus of approximately $5(10^2)$ *dyn/cm* and a membrane planar shear modulus of approximately $6(10^{-3})$*dyn/cm* (Mohandas and Evans, 1994).

2.3 Previous Work on Red Blood Cell Mechanical Properties

2.3.1 Constitutive Modeling: ***Skalak, Evans, Mohandas, Hocmuth***

Fung and Tong (1968) first introduced a relationship between the principal stresses and the principal strains in terms of the isotropic elastic Lame` constants μ and λ:

$$\begin{aligned} T_1 &= h\left(\mu e_{11} + \lambda(e_{11}+e_{22})\right), \\ T_2 &= h\left(\mu e_{22} + \lambda(e_{11}+e_{22})\right). \end{aligned} \qquad (2.1)$$

Here, h is the thickness of the membrane. These equations hold for small strains.

Skalak et al. (1973) noted that the strain energy function for the human red blood cell membrane contains two terms in it, one related to the area change, and the second related to the elastic modulus at constant area, i.e the shear modulus. Evans (1973), Skalak et al. (1973), and Evans and Hochmuth (1977) emphasized that the membrane behavior is essentially a two-dimensional analogue to a rubbery solid which shears readily, yet is nearly incompressible.

Skalak et al., (1973) used alternative forms of the invariants defined as: $I_1=2(e_{11}+e_{22})$ and $I_2= 4e_{11}e_{22}+2(e_{11}+e_{22})$, where $e_{11}= \frac{1}{2}(\lambda_1^2 -1)$ and $e_{22}=\frac{1}{2}(\lambda_2^2-1)$.

These definitions give:

$$\begin{aligned} I_1 &= \lambda_1^2 + \lambda_2^2 - 2, \\ I_2 &= \lambda_1^2\lambda_2^2 - 1 = \left(\frac{dA}{dA_0}\right)^2 - 1. \end{aligned} \qquad (2.2)$$

The preservation of the area constraint gives:

$$I_2 = 0. \tag{2.3}$$

Then Skalak et al. (1973) postulated a hyperelastic constitutive model, considering a plane thin rectangular element, to define the stress-stretch relationships.

The simple form of strain energy density equation Skalak et al. (1973) used was in the Neo-Hookean form of:

$$W = \frac{B}{4}\left(\frac{1}{2}I_1^2 + I_1 - I_2\right) + \frac{C}{8}I_2^2; \tag{2.4}$$

where B and C are taken to be constant material properties.

Using continuum mechanics approaches:

The first Piola Kirchoff Stress is found from:

$$S_{ij} = \frac{\partial W}{\partial e_{ij}}; \tag{2.5}$$

and, the Cauchy Stress is found from:

$$T_{ij} = \frac{1}{J} S_{kl} \frac{\partial x_i}{\partial X_k} \frac{\partial x_i}{\partial X_l}. \tag{2.6}$$

Here x_i is the final coordinate, and X_k is the initial coordinate, and J is the determinant in the form of:

$$J = \left|\frac{\partial x_i}{\partial X_j}\right| = \lambda_1 \lambda_2 \text{ (i, j = 1, 2, 3).} \tag{2.7}$$

The uniaxial tension-stretch curves introduced by Skalak et al. (1973) agreed with Hochmuth and Mohandas (1972) results.

Evans represented the energy per unit area of the hyperelastic membrane network as:

$$E = \mu\left(\lambda_1^2 + \lambda_2^2\right)/2, \qquad (2.8)$$

where λ_1 and λ_2 are principal stretch ratios for a unit rectangle element and μ is the shear modulus of the membrane. Note that Equation (2.8) should read $E = \mu\left(\lambda_1^2 + \lambda_2^2 - 2\right)/2$, to account for zero energy when $\lambda_1 = \lambda_2 = 1$.

Mohandas and Evans, in their review paper from 1994, examined the outcomings of the experiments conducted over the period from 1974 to 1994. They studied the relations between the architecture and the mechanical properties of the cell membrane.

The structural determinants of the membrane elastic properties can be summarized as follows:

A. Membrane Area (Dilatation Elasticity)
B. Membrane Bending Elasticity
C. Membrane Extensional Elasticity

A. Membrane Area (Dilatation Elasticity)

Evans showed the area restrictions using Micro-pipette aspiration techniques comparing an osmotically preswollen red cell and a bilayer vesicle (Figure 2.5). He showed that the red blood cells and the lipid bilayer rupture at an expansion of only 2-3%. Meaning, the surface area change that a cell can undergo is negligible. However red cells lyse at lower tension levels than the bilayer vesicles, meaning, the underlying protein network somehow weakens the red cell. From here, it can be concluded that the resistance to change in surface area is due to the lipid bilayer. They derived, from the micro-pipette aspiration experiments, that the planar area modulus of the membrane is 500 dyn/cm.

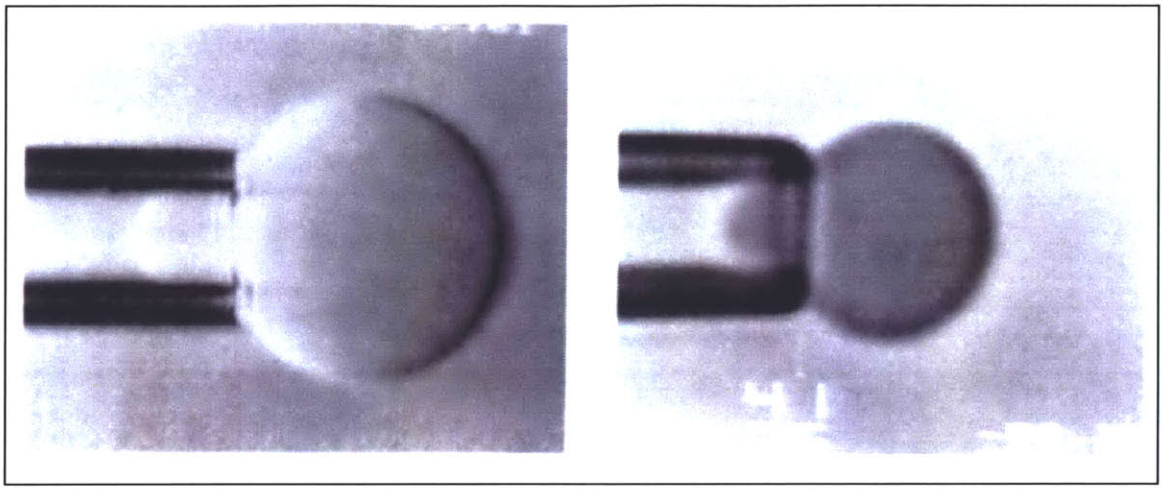

***Fig. 2.5:** The video-micrograph of a phospholipid bilayer (left, diameter=20μm) and a pre-swollen red cell (left, diameter=6μm) drawn into a pipette showing the change in the surface area of the membrane is correlated with the bilayer in the red blood cell (Mohandas et al., 1994).*

B. Membrane Bending Elasticity

The lipid bilayer dominates the opposition to bending (Evans et al., 1980). When the red cell membrane is deformed by aspiration into a micropipette (Figure 2.5), the bending stiffness regulates the shape of the membrane at the entrance.

C. Membrane Extensional Elasticity

To look at the extensional elasticity of the membrane, demonstrations are done by aspiration of a flaccid discocyte in a small suction pipette (Figure 2.6). The lipid bilayer dominates the planar area modulus and bending stiffness of the cell (Evans et al., 1980). However, the lipid bilayer contributes negligibly to the extensional rigidity of the red cell as it is similar to a liquid layer. The suction pressure is much bigger than the threshold stress required to overcome the bending rigidity of the membrane, therefore the plots of the suction pressure vs. the aspiration length gives the coefficient of extensional rigidity of the red cell, μ. From the mechanics point of view, μ is a measure of the planar shear stiffness.

Extensional elasticity represents the major reason of the recovery of the cell's shape after deformation and it is mainly due to the shear response of the protein network underneath the bilayer.

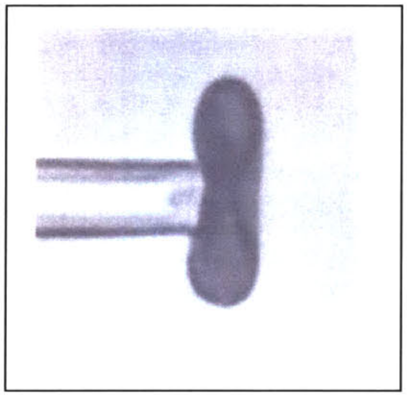

Fig. 2.6: *The video-micrograph of the red blood cell discocyte aspiration(Mohandas et al., 1994).*

2.3.2. Triangulated Nets: *Discher, Boal, Boey, Wintz*

Discher et al. (1997) modeled the spectrin network as a C6 network of Hookean springs. Discher et al.'s triangulated network (Figure 2.7):

i. Maintains connectivity at all times, long-range atomic diffusion or self avoiding elements do not exist in the network.
ii. It is constructed of linear elements which are thin rods that do not overlap, except at the vertices.
iii. Defects in the triangulated network are excluded.
iv. Any energy storage due to angle change between elements in the strain energy function is excluded.

v. Only in-plane motions are allowed in the model (i.e. out of plane buckling is excluded).

These researchers (Discher et al., 1997) formulated the expressions for the elastic strain energy for triangulated networks as a function of the distance between vertices and the area of the triangles.

Wintz et al. (1997) referred to the network as a hexagonal network of chains with Hookean spring behavior. They noted that the constituent chains have a non-zero end-to-end distance since they have a self-avoiding nature and the network has a non-vanishing area.

Wintz et al. (1997) discussed a phenomenon called the "collapse" phenomenon. At low temperatures, the networks undergo a "collapse transition" with increasing compression. In the 2-phase region, collapsed and non-collapsed triangles coexist. Discher et al. (1997) also defined the collapse state as the state at which the triangle completely transforms/crushes into a line (Figure 2.7). Since this state is against the assumption of bond interactions and area diminishing, it is called "collapse" state. This state is not reached for the real network. This collapsed state is impossible because of the existence of the bilayer which constrains the area change needed for such a collapse.

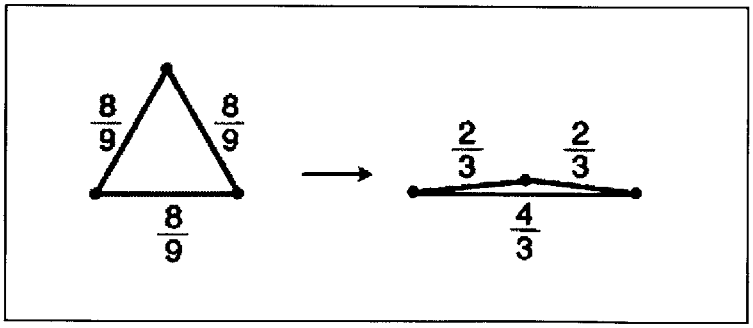

Fig. 2.7: C6 to C2 transition of the network unit cell (Discher et al., 1997).

Wintz et al. (1997) mentioned in his paper that, one application of the hexagonal network formulation is the protein skeleton of the red blood cell membrane. These researchers also noted that when the membrane is compressed, instead of buckling into the third-dimension, if the bending modulus of the membrane is large enough, lateral compression of a network patch occurs (Figure 2.8).

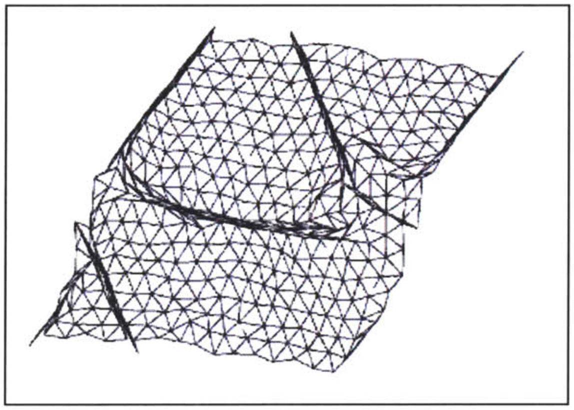

Fig. 2.8: *Wintz et al.'s network under compression (1997).*

Discher et al. (1998) worked on a network of molecular chains represented by the WLC model (Marko and Siggia, 1995). The WLC, characterized by two parameters, the presistance length, A and the locking stretch, λ_c, provides a better describtion of the network behavior than do the Hookean springs. The polymer network, unlike the spring network do not display collapse transformations under compression.

2.4 Constitutive Model

The constitutive model development for the general membrane stress-stretch behavior of the triangulated spectrin network follows the successful methodology of rubber elasticity (Trelor, 1958, Arruda and Boyce, 1993, Boyce and Arruda, 2000) and can be broken down as follows:

- Idealization of the networked microstructure and identification of a Representative Volume Element (RVE),
- Application of macroscopic deformation to the RVE,
- Assignment of mechanical behavior to constituent elements of the RVE,
- Determination of the RVE strain energy,
- Differentiation of the strain energy function to obtain the general multiaxial stress-stretch behavior.

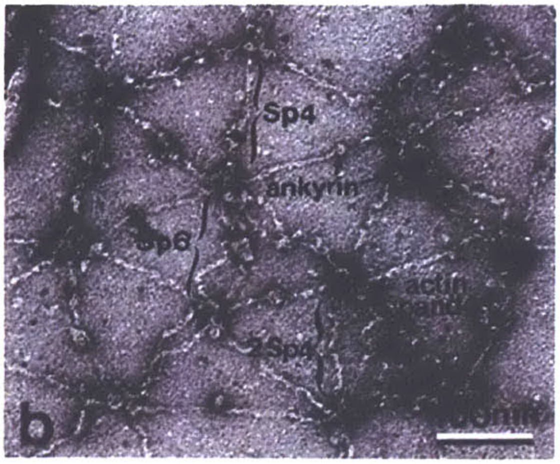

Fig. 2.9: *Electron micrograph of a spread human erythrocyte cytoskeleton (Liu et al., 1987).*

2.4.1 Microstructure Idealization and Corresponding Representative Volume Element

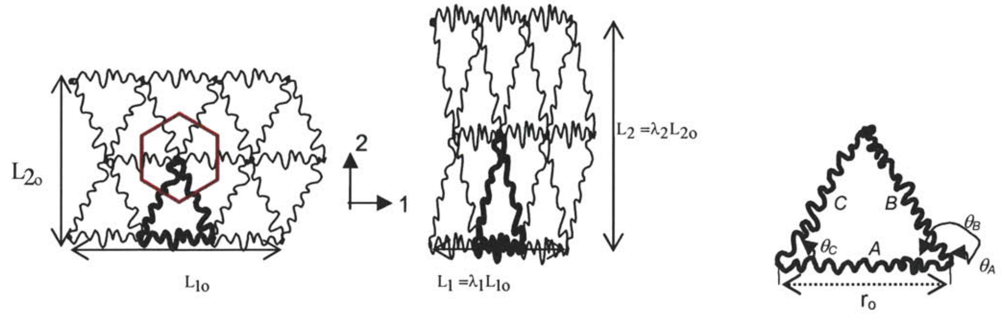

(A) ***(B)*** ***(C)***

Fig. 2.10: *Schematic of the planar triangulated network in* ***(A)*** *the undeformed state, also depicting Voronoi tessellation to identify the area of the RVE;* ***(B)*** *when stretched in the 2-direction (planar area is preserved);* ***(C)*** *the representative volume element.*

Examination of spread red blood cell membranes by high resolution negative staining electron microscopy reveals the microstructure of the spectrin network (Figure 2.9). A planar network is observed where typically 5-6 spectrin molecules emanate from each crosslink site forming a rather regular triangulated network. This structure has also been referred to as a hexagonal lattice structure (Boey et al., 1998), where we note six triangles form each hexagon. We idealize this microstructure as a regular planar triangulated network as shown in Figure 2.10. Therefore the representative unit cell to analyze the mechanical behavior is chosen to be an equilateral triangle (Figure 2.10, C). Noting that each chain in the unit cell triangle also contributes to its neighboring triangle, we use Voronoi tesselation to identify the area affiliated with the chosen unit cell RVE (Figure 2.10, A). Voronoi tesselation gives the area associated with the RVE constituents to be twice the area of the RVE triangle; this area will be needed for properly constructing the strain energy density of the network later.

2.4.2 Deformation of the Network RVE

An arbitrary planar deformation is applied to the unit cell equilateral triangle where the planar deformation gradient $\mathbf{F}_{2D}$ is defined in the 1-2 frame as:

$\mathbf{F}_{2D} = \frac{\partial \mathbf{x}}{\partial \mathbf{X}} = \begin{bmatrix} F_{11} & F_{12} \\ F_{21} & F_{22} \end{bmatrix}$ where x is the deformed position of a material point and X is the reference position. The RVE is subjected to an arbitrary deformation gradient (Figure 2.11), giving the stretch of constituent network chains A, B, C in terms of the macrosopic deformation gradient. The simplicity of the unit cell triangle RVE provides a unique, kinematically-determined mapping of the macroscopic deformation gradient to the microscopic network deformation. Denoting the current end-to-end distance of each chain as $r_i(i = A, B, C)$, the axial stretch of each chain in the network is, $\lambda_i = \frac{r_i}{r_0}(i = A,B,C)$ and can be expressed in terms of an arbitrary planar deformation gradient:

$$\begin{aligned} \lambda_A &= \left(F_{11}^2 + F_{21}^2\right)^{\frac{1}{2}} \\ \lambda_B &= \frac{1}{2}\left(\left(F_{11} - F_{12}\sqrt{3}\right)^2 + \left(F_{21} - F_{22}\sqrt{3}\right)^2\right)^{\frac{1}{2}} \qquad (2.8) \\ \lambda_C &= \frac{1}{2}\left(\left(F_{11} + F_{12}\sqrt{3}\right)^2 + \left(F_{21} + F_{22}\sqrt{3}\right)^2\right)^{\frac{1}{2}} \end{aligned}$$

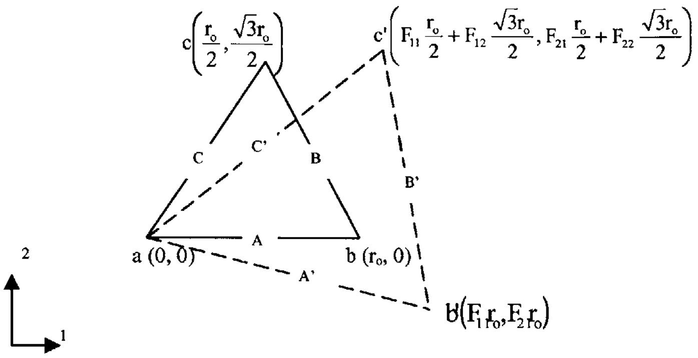

Fig. 2.11: Schematic of the RVE in undeformed configuration (solid lines) and when subjected to an arbitrary planar deformation gradient (dashed lines).

2.4.3 Constitutive Stress-Stretch Behavior of Chains

The stress vs. stretch relationship of the membrane will depend on the axial force-extension behavior of the constituent chains. In this paper, two representations of chain behavior will be studied: linear axial extension behavior and non-Gaussian freely-jointed molecular chain behavior.

2.4.3.1 Linear Chain

The linear force-extension behavior of a chain is given by:

$$P_{ch} = k_{ch} r_o (\lambda_{ch} - 1); \qquad (2.9)$$

with corresponding strain energy:

$$\mathcal{U}ch_{LC} = \frac{1}{2} k_{ch} r_o^2 (\lambda_{ch} - 1)^2; \qquad (2.10)$$

where k_{ch} is the chain axial stiffness in units of force/length and r_o is the initial chain length.

2.4.3.2 Molecular Chain

The force-extension behavior of a molecular chain is taken to follow that of a non-Gaussian freely-jointed chain obtained from statistical mechanics treatments of long chain molecules (see, for example, Treloar (1958)).

The Freely Jointed Chain

The freely jointed chain (FJC) model idealizes a molecular chain to be constructed of N rigid Kuhn segments of length l which are free to rotate with respect to one another at their joints; the fully extended contour length is then:

$$L_c = Nl. \tag{2.11}$$

The FJC can accommodate an end-to-end distance r by many different configurations of these connected links and the links will continuously sample this configuration space through thermal fluctutations. Statistics are used to study these configurations as a function of end-to-end distance and thus determine changes in entropy with extension.

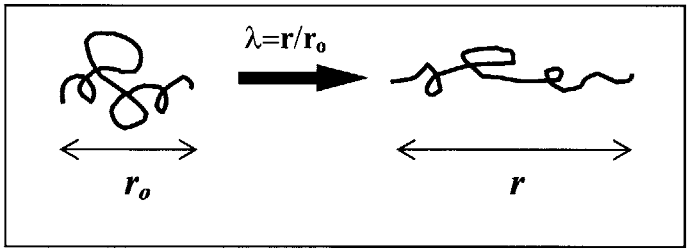

Fig. 2.12: *A schematic of the initial (r_o) and current (r) end-to-end distance of a long chain molecule under deformation.*

A. Gaussian Statistics

Kuhn and Grun (1942) derived the probability density function which shows the position of the end of a randomly jointed chain when the beginning point is held fixed. This function is only approximate because it assumes the end-to-end distance of a chain is much smaller than its contour length, i.e. $r << Nl$.

If a chain lies in a spherical shell of radius r, the probability density at a point r is:

$$P(r) = \left[\frac{3}{2\pi Nl^3}\right]^{\frac{3}{2}} \exp\left[\frac{-3r^2}{2Nl^2}\right] \quad (2.12)$$

Boltzmann developed the general principles of statistical thermodynamics where entropy (S) is proportional to the number of configurations of a system:

$$s = \kappa_B\left[\ln p(x, y, z)dV\right] = c - \frac{9}{4}\kappa_B N^2 l^4 r^2 \quad (2.13)$$

where κ_B is the Boltzmann's constant and c is an arbitrary constant.

The Helmholtz free energy for the chain is

$$\Delta\psi = -\theta\Delta s \quad (2.14)$$

where θ is the absolute temperature.

Average tensile force acting along the direction of r, f:

$$f = \frac{\Delta\psi}{dr} = -\theta\frac{dS}{dr} = \frac{9}{2}\kappa_B\theta N^2 l^4 r \quad (2.15)$$

B. Non-Gaussian Treatment of Single Molecules

Gaussian theory is for small to modest extensions of the chains since the Gaussian probability distribution function does not account for the fact that the number of configurations that can accommodate an end-to-end distance *r* will become severely limited when $r \geq \frac{1}{3}nl$ and will not follow equation (2.10). The non-Gaussian probability function, as derived by Kuhn and Grun (1942) is given by:

$$ln\,p(r) = c - N\left(\frac{r}{Nl}\beta + ln\frac{\beta}{sinh\,\beta}\right) = c - N\left\{\frac{3}{2}\left(\frac{r}{Nl}\right)^2 + \frac{9}{20}\left(\frac{r}{Nl}\right)^4 + \frac{99}{350}\left(\frac{r}{Nl}\right)^6 + \ldots\right\} \qquad (2.14)$$

where,

$$\mathcal{L}(\beta) = \frac{r}{Nl} = \coth\beta - \frac{1}{\beta}, \qquad (2.16)$$

$$\beta = \mathcal{L}^{-1}\left(\frac{r}{Nl}\right). \qquad (2.17)$$

The inverse Langevin function is a function of the ratio of current end-to-end distance of a single chain to the contour length of the chain. The inverse Langevin function is a mathematical explanation of the upturn in stress experienced at large stretches as the number of configurations of the rigid links to accommodate $r \rightarrow Nl$ becomes severely limited. For small extensions, $r \le \frac{1}{3}nl$, the non-Gaussian theory reduces to the Gaussian theory.

Non-Gaussian Freely Jointed Chain vs. Worm Like Chain

Macromolecular chains have been well-modeled by both the freely jointed chain (FJC) and the worm like chain (WLC) representations.

The FJC:

- Contains N bonds of fixed bond length l.
- The directions of the neighboring bonds are completely random.
- $L_c = Nl$, is the contour length of the chain.
- The persistance length is equal to the Kuhn segment length or so called "bond length".

The WLC:

- Includes the bending of the chains.

- The direction of the neighboring bonds change again, but in a continuous manner in this case.
- The model is characterized by L_c, the contour length of the chain and also the persistance length, A, which is the projection of a tangent to the chain lying along a given length of the chain prior to any strong change in direction from the tangent line. The change in direction due to the bending of the chain and thus the persistance length is related to the bending stiffness of the chain. Higher bending stiffness means longer persistance length.
- The force extension behavior of a single WLC, using the Marko and Siggia (1995) curve fitting expression, is given as:

$$P_{ch} = \frac{k_B\theta}{A}\left(\frac{r}{L_C} + \frac{1}{4(1-r/L_C)^2} - \frac{1}{4}\right), \tag{2.18}$$

with a corresponding strain energy:

$$\mathcal{U} = \frac{k_B\theta}{A} L_C \left[\frac{1}{2}\left(\frac{r}{L_C}\right)^2 + \frac{1}{4\left(1-r/L_C\right)} - \frac{1}{4}\left(\frac{r}{L_C}\right)\right], \tag{2.19}$$

where r is the end-to-end distance, A is the persistence length $(l = 2A)$.

For our spectrin network model, we use the FJC model for the force-extension behavior of each chain:

$$P_{ch_{NGC}} = \frac{Nk_b\theta}{L_c}\beta_{ch}; \tag{2.20}$$

with corresponding strain energy:

$$\mathcal{U}_{ch_{NGC}} = k_b\theta N\left(\frac{r}{L_C}\beta + \ln\left(\frac{\beta}{\sinh\beta}\right)\right); \tag{2.21}$$

where N is the number of Kuhn segments along the chain, k_b is Boltzmann's constant, θ is the absolute temperature, $L_c = Nl$ is the contour length of the chain, l is the Kuhn segment length, r is the chain end-to-end distance and β is the inverse Langevin function.

2.4.4 Strain Energy Density of the RVE

The strain energy of the RVE, U, is the summation of the strain energy in each chain:

$$\mathcal{U} = \mathcal{U}_A + \mathcal{U}_B + \mathcal{U}_C . \tag{2.22}$$

Strain energy density is typically defined as the strain energy divided by the initial volume of the material. The membrane is a planar network of essentially single molecule thickness. Therefore the strain energy density, U^*, is taken here to be strain energy per unit initial planar area. The initial planar area of the RVE is twice the area of the unit cell triangle following Voronoi tesselation :

$$\mathcal{U}^* = \frac{1}{2A_{triangle}} (\mathcal{U}_A + \mathcal{U}_B + \mathcal{U}_C) . \tag{2.23}$$

Using the strain energy expressions for each element found earlier together with the kinematics describing the deformation for each element, the following expression for the strain energy density function for the network of linear chains, U^*_{LC} is obtained:

$$\mathcal{U}^*_{LC} = \frac{1}{2A_{triangle}} \sum_{i=A,B,C} k_{ch} r_o^2 (\lambda_i - 1)^2 ; \tag{2.24}$$

Noting that the chain areal density, υ, is three chains per $(2A)_{triangle}$, the strain energy density may be written as:

$$\mathcal{U}_{LC}^{*} = \frac{\upsilon}{3} k_c h r_o^2 \sum_{i=A,B,C} (\lambda_i - 1)^2 \qquad (2.25)$$

Similarly, for the non-Gaussian network, the strain energy density is given by:

$$\mathcal{U}_{NGC}^{*} = \frac{\upsilon}{3}\left\{ k_b \theta N \sum_{i=A,B,C} \left[\frac{\lambda_i r_o}{L}\beta_i + \ln\left(\frac{\beta_i}{\sinh\beta_i}\right) - \left(\frac{r_o}{L}\beta_o + \ln\left(\frac{\beta_o}{\sinh\beta_o}\right)\right)\right]\right\} \qquad (2.26)$$

where r_o is the initial end-to-end distance (i.e. the initial chain length or distance between crosslinks), $\lambda_i (i = A, B, C)$ are the chain stretches defined earlier as a function of the macroscopic deformation gradient, and $\beta_i = \mathcal{L}^{-1}\left(\frac{\lambda_i r_o}{L_c}\right)$.

2.4.5 Stress- Stretch Relationships

The stress-stretch behavior is determined by proper differentiation of the strain energy density function. Given a strain energy density which is a function of the deformation gradient, the first Piola Kirchoff Membrane Stress* is derived as:

$$T_0 = \frac{\partial(\mathcal{U}^{*})}{\partial(F)}. \qquad (2.27)$$

The Cauchy Stress tensor is then obtained from:

$$T = \frac{1}{J} T_0 F^T, \qquad (2.28)$$

where J= det (**F**) is the planar area ratio (ratio of current area to original area). Here, we take J=1 due to the preservation of area constraint imposed by the lipid bilayer which then necessitates an additional energy-indeterminate equibiaxial stress term, *h***I**, giving:

---

* where we define membrane stress to be the product of stress and membrane thickness; thus membrane stress has units of force/length.

$$T = T_0 F^T + hI. \tag{2.29}$$

Noting that the U_i (i=A, B, C) are functions of λ_i (i=A, B, C), and λ_i (i=A, B, C) are functions of the deformation gradient, gives:

$$T_0 = \frac{\partial \mathcal{U}_A^*}{\partial \lambda_A} * \frac{\partial \lambda_A}{\partial F} + \frac{\partial \mathcal{U}_B^*}{\partial \lambda_B} * \frac{\partial \lambda_B}{\partial F} + \frac{\partial \mathcal{U}_C^*}{\partial \lambda_C} * \frac{\partial \lambda_C}{\partial F}. \tag{2.30}$$

The $\left(\frac{\partial \lambda_i}{\partial F}\right)$ terms are independent of chain constitutive behavior and are given in the Appendix.

For the linear chains:

$$\frac{\partial \mathcal{U}_i^*}{\partial \lambda_i} = \frac{\upsilon}{3} k_{ch} (\lambda_i - 1), \qquad \mathrm{i} = \mathrm{A,B,C} \quad ; \tag{2.31}$$

For the non-Gaussian chain model:

$$\frac{\partial \mathcal{U}_i^*}{\partial \lambda_i} = \frac{\upsilon}{3} k_b \theta N \frac{r_o}{L_c} \beta_i, \quad \mathrm{i} = \mathrm{A,B,C} \ ; \tag{2.32}$$

where $\beta = \mathcal{L}^{-1}\left(\frac{r}{L_c}\right)$. The effect of a finite planar area modulus can be incorporated into the strain energy function by addition of the strain energy corresponding to planar area changes in a manner analogous to the treatment of finite compressibility in rubber elasticity (e.g., Boyce and Arruda, 2000).

2.5 Determination of Material Properties

The planar shear modulus of the red blood cell membrane has been experimentally found to be between .006-0.010 *dyn/cm* (e.g. Mohandas and Evans, 1994). The initial end-to-end distance of chains in the spectrin network is taken to be r_o=75*nm* following Boal (1994) which, from geometry, gives an areal chain density of $\upsilon = 6.16(10^{14})/m^2$. The fully extended contour length of the network chains has been found to be nominally 180*nm* (Liu, et al., 1987). In order to meet a target initial shear modulus value of approximately 0.010 *dyn/cm*, the linear chain stiffness was found to be $k_{ch} = 0.033 dyn/cm$. In order to meet this same shear modulus value for the non-Gaussian chain network while simultaneously meeting the initial end-to-end length and the contour length, the Kuhn segment length was found to be l=10.5nm, giving N=18. Absolute temperature is taken to be, θ=300K, since the literature data are obtained at 300K.

2.6 Uniaxial Tensile Behavior

The axial stress (T_{11}) versus axial stretch (λ) relationships for uniaxial tension in the 1-direction for the linear chain network (LC) and the non-Gaussian chain network (NGC) are given by:

$$T11_{LC} = \frac{\upsilon}{3} k_{ch} r_o^2 \left\{ \lambda \left[\lambda - 1 + \lambda \left(\frac{1}{2} - \left(\lambda^2 + 3\lambda^{-2} \right)^{-\frac{1}{2}} \right) \right] - 3\lambda^{-2} \left(\frac{1}{2} - \left(\lambda^2 + 3\lambda^{-2} \right)^{-\frac{1}{2}} \right) \right\} \qquad (2.33)$$

$$T11_{NGC} = \frac{\upsilon}{3} k_B \theta N \frac{r_o}{L_c} \left\{ \lambda \left[\beta_A + \beta_B \lambda \left(\lambda^2 + 3\lambda^{-2} \right)^{-\frac{1}{2}} \right] - 3\beta_B \lambda^{-2} \left(\lambda^2 + 3\lambda^{-2} \right)^{-\frac{1}{2}} \right\} \qquad (2.34)$$

where: $\beta_i = \mathcal{L}^{-1}\left(\frac{\lambda_i r_o}{L_c} \right)$ and i= A, B, C.

The axial stress (T_{22}) versus axial stretch (λ) relationships for uniaxial tension in the 2-direction for the case of a network with constituent linear chains and the case of a network with constituent non-Gaussian chains, respectively, are given by:

$$T22_{LC} = \frac{\upsilon}{3} k_{ch} r_o^2 \left\{ 3\lambda^2 \left[\frac{1}{2} - \left(3\lambda^2 + \lambda^{-2} \right)^{-\frac{1}{2}} \right] - \lambda^{-1} \left[-1 + \lambda^{-1} + \lambda^{-1} \left(\frac{1}{2} - \left(3\lambda^2 + \lambda^{-2} \right) \right)^{-\frac{1}{2}} \right] \right\}$$

(2.35)

$$T22_{NGC} = \frac{\upsilon}{3} k B \theta N \frac{r_o}{L_c} \left\{ 3\lambda^2 \beta_B \left(3\lambda^2 + \lambda^{-2} \right)^{-\frac{1}{2}} - \lambda^{-1} \left[\beta_A + \beta_B \lambda^{-1} \left(3\lambda^2 + \lambda^{-2} \right)^{-\frac{1}{2}} \right] \right\} \quad (2.36)$$

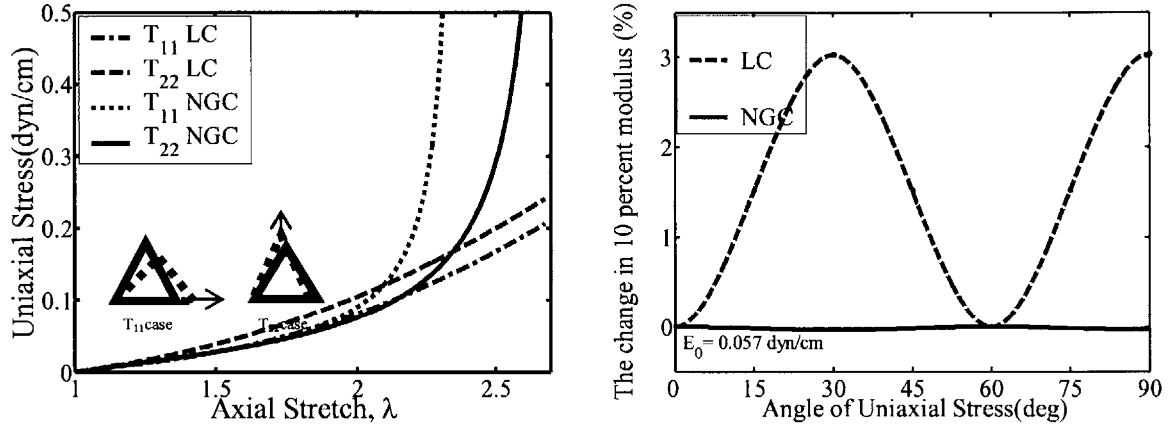

(A) *(B)*

Fig. 2.13: *(A) Uniaxial tensile stress vs stretch behavior in the 1-direction and the 2-direction for constituent Linear and constituent Non-Gaussian Chain Behaviors. (B) Percent change in the 10 percent strain secant modulus vs. the angle of the uniaxial tension applied for various angles with respect to axis 1 for Linear Chain and Non Gaussian Chain Behavior.*

Figure 2.13,A shows the uniaxial Cauchy stress vs stretch behavior for loading in the 1- and 2-directions, using LC and NGC representations. For small axial stretch (λ<*1.10*), both networks exhibit an essentially linear behavior. Nonlinear axial stress-stretch behavior becomes clearly apparent after a stretch of ~*1.50*. There are three different sources of nonlinearity in the stress-stretch response of the network:

1. Material nonlinearity due to evolution in the microstructure geometry (changes in length and angles of chains),

ii. Material nonlinearity arising from the nonlinear constituent chain behavior (for the non-Gaussian chain case)

iii. Geometric nonlinearity due to macroscopic shape change with deformation.

The sources of nonlinearity in the linear chain network arise from (i) and (iii), whereas, all three sources of nonlinearity are inherent in the non-Gaussian chain network behavior.

The uniaxial stress-stretch curves are direction dependent for both the LC and NGC cases as shown by the different stress-stretch behaviors obtained in the 1-and 2-directions. The six-fold symmetry of the initial (undeformed) microstructure results in isotropy of the very initial modulus. However, even at an axial strain as small as 10%, anisotropy begins to manifest itself as shown in Figure 2.13.B which shows the 10% strain secant modulus as a function of loading direction. The anisotropy is more apparent and important in the large strain behavior, where the stress-stretch curves of Figure 2.13.A show significant differences (especially for NGC network) at large stretches.

To understand the predicted stress-stretch behavior, we examine the evolution in the triangulated network microstructure. Figure 2.14.A shows the evolution of chain stretch and chain orientation during uniaxial tension in the 1-direction. Chains B and C respond identically to the applied loading because of the symmetry. As the network is deformed, chains stretch and orient to accommodate the imposed deformation. As shown in Fig 2.13.A, since chain A is aligned with the loading direction, it does not reorient (θ_A is constant) and simply stretches by the imposed macroscopic stretch. Chains B and C are seen to monotonically orient towards the 1-direction; one observation is that, although these chains rearrange themselves as the applied macroscopic stretch increases, they exhibit a non-monotonic change in chain stretch with imposed macroscopic stretch: the chains first undergo a small amount of contraction from their initial end-to-end distance and then undergo extension.

Figure 2.14.B shows chain force versus macroscopic stretch for uniaxial tension in the 1-direction. Here, for LC behavior, chain A is aligned with the loading direction and therefore shows a linear chain force vs. macroscopic stretch behavior. However chains B and C both stretch and rotate towards the loading direction, therefore their chain force values exhibit a nonlinear history with macroscopic stretch for the LC network. For the NGC, the force-extension curve for chain A shows the typical non-Gaussian behavior since it is directly axially stretched; chains B and C rotate and stretch with deformation and thus show a different nonlinear behavior and a later upturn in the chain force.

Chain force vs macroscopic stretch curves also provide insight regarding the direction-dependence of the evolution of macroscopic stress with macroscopic stretch. In Figure 2.14.A, the uniaxial stress behaviors in the 1-and the 2-directions are identical for NGC behavior until $\lambda > 1.50$. The curves depart at larger stretches and uniaxial membrane stress in the 1-direction curve gives an earlier upturn than uniaxial membrane stress in the 2-direction. Uniaxial tension in the 1-direction is dominated by chain A (Fig. 2.14.A,B),

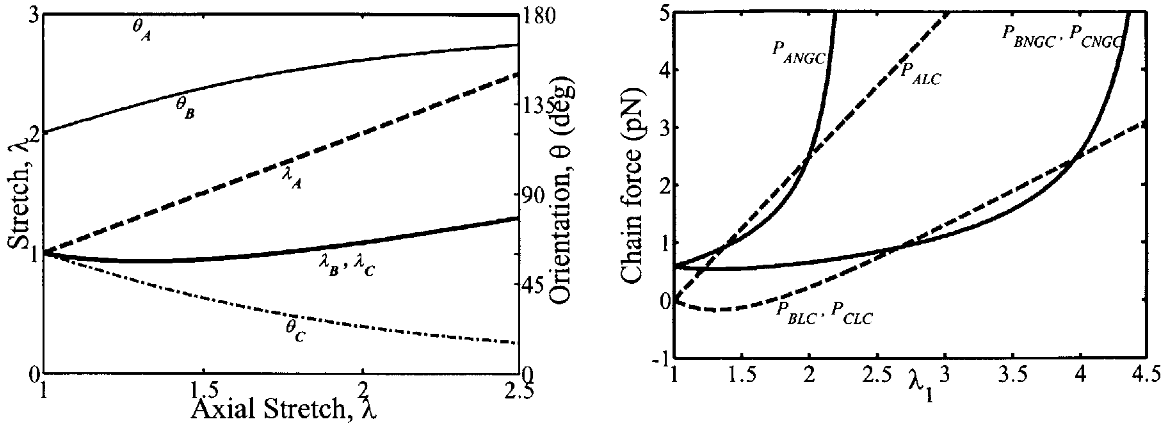

(A) *(B)*

Fig. 2.14: ***(A)*** *Evolution of chain orientation and chain stretch with respect to axis 1 for chains A, B and C for uniaxial tension in the 1-direction.* ***(B)*** *Evolution of force in chains A, B and C with axial stretch in the 1-direction.*

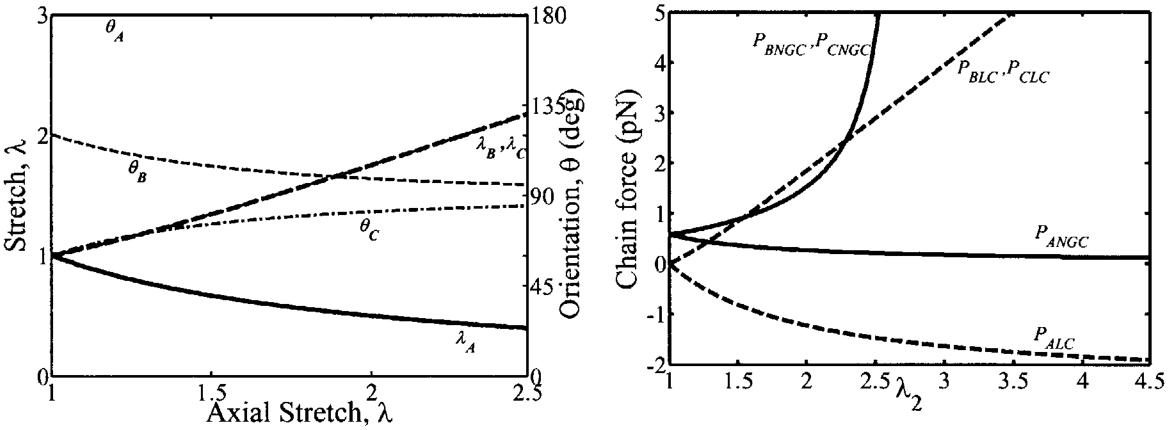

(A) *(B)*

Fig. 2.15: *(A) Evolution of chain orientation and chain stretch with respect to axis 1 for chains A, B and C for uniaxial stress in the 2-direction. (B) Evolution of force in chains A, B and C with axial stretch in the 2- direction.*

which is directly axially stretched resulting in the earlier upturn in the macroscopic stress-stretch curve. Uniaxial tension in the 2-direction is dominated by chains B and C (Fig. 2.15.A,B), which accommodate macroscopic stretch by both rotating and stretching, thus giving the upturn in macroscopic stress at a larger macroscopic stretch.

2.7 Simple Shear Behavior

The shear stress (T_{12}) versus the shear angle (tan γ) relationships for simple shear of the linear chain network and the non-Gaussian chain network are given by:

$$T12_{LC} = \frac{\upsilon}{2\sqrt{3}} k_{ch} r_o^{2} \left\{ \left(\frac{1}{2}\left(g_1^2+3\right)^{\frac{1}{2}} - 1 \right) g1 \left(g_1^2+3\right)^{-\frac{1}{2}} - \left(\frac{1}{2}\left(g_2^2+3\right)^{\frac{1}{2}} - 1 \right) g2 \left(g_2^2+3\right)^{-\frac{1}{2}} \right\},$$

(2.37)

$$T12_{NGC} = \frac{\upsilon}{2\sqrt{3}} k_B \theta N \frac{r_o}{L_c} \left\{ \beta_C g1 \left(g_1^2+3\right)^{-\frac{1}{2}} - \beta_B g2 \left(g_2^2+3\right)^{-\frac{1}{2}} \right\}, \qquad (2.38)$$

where, $g_1 = \left(1+\sqrt{3}\tan\gamma\right)$, $g_2 = \left(1-\sqrt{3}\tan\gamma\right)$ and $\beta_i = \mathcal{L}^{-1}\left(\frac{\lambda_i r_o}{L_c}\right)$, i= A, B, C.

The shear stress (T_{21}) versus the shear angle (tan γ) relationships for simple shear for the case of a network with constituent linear chains and the case of a network with constituent Non-Gaussian chains, respectively, are given by:

$$T21_{LC} = \frac{\upsilon}{6} k_{ch} r_o^2 \left\{ 2(f1 - 1) f_1^{-1} \tan\gamma + \left(\frac{1}{2}\left(1 + f_2^2\right)^{\frac{1}{2}} - 1 \right) f2 (1 + f2)^{-\frac{1}{2}} + \left(\frac{1}{2}\left(1 + f_3^2\right)^{\frac{1}{2}} - 1 \right) f3 (1 + f3)^{-\frac{1}{2}} \right\},$$

(2.39)

$$T21_{NGC} = \frac{\upsilon}{6} k_B \theta N \frac{r_o}{L_{contour}} \left\{ 2\beta_A f1^{-1} \tan\gamma + \beta_C f2 \left(1 + f_2^2\right)^{-\frac{1}{2}} - \beta_B f3 \left(1 + f_3^2\right)^{-\frac{1}{2}} \right\}, \quad (2.40)$$

where $f_1 = \left(1 + \tan\gamma^2\right)^{\frac{1}{2}}$; $f_2 = \left(\tan\gamma - \sqrt{3}\right)$; $and\, f_3 = \left(\tan\gamma + \sqrt{3}\right)$.

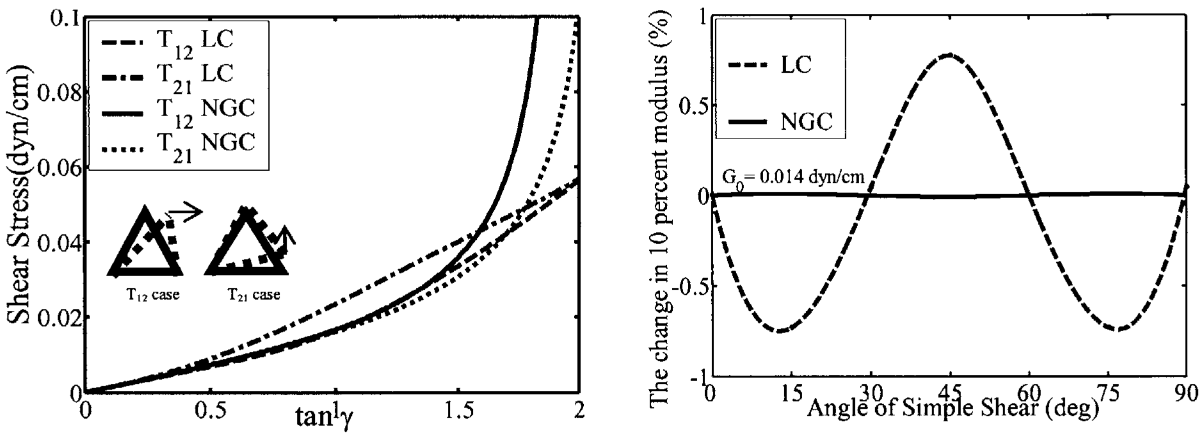

***Fig.2.16:** (A) Simple shear stress vs shear angle behavior in the 12-direction and in the 21-direction for constituent Linear and constituent Non-Gaussian Chain Behaviors. (B) Percent change in the 10 percent strain secant modulus vs. the angle of the simple shear applied for various angles with respect to axis 1 for Linear Chain and Non-Gaussian Chain Behavior.*

Figure 2.16.A shows the behavior of the network for simple shear in 12- and in 21-directions, using linear chain and non-Gaussian chain models up to a macroscopic stretch of tan γ =2. The initial slope of these four curves is the same, giving the shear modulus to be 0.014 *dyn/cm*. The larger deformation behavior is nonlinear and anisotropic.

Figure 2.17.A and 2.17.B show the evolutions in microscopic chain stretches/orientations and chain forces, respectively, for simple shear in the 12-direction. Chain A is neither stretched nor rotated in simple shear in the 12-direction. Chains B and C rotate and stretch. Both B and C monotonically rotate towards alignment with the shear flow; chain C monotonically extends whereas Chain B first contracts then extends. Note that, due to the pretension present in the NGC model, Chain B does not experience a compressive force during its contraction. Chain C extension governs the upturn in the macroscopic stress-strain behavior of the NGC model.

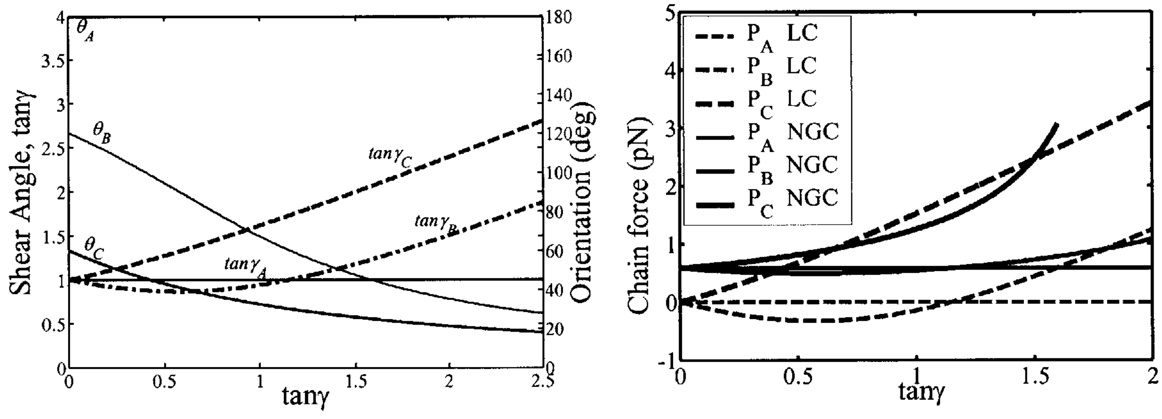

Fig. 2.17: (A) Evolution of chain orientation and chain shear angle with respect to axis 1 for chains A, B and C for simple shear in the 12-direction. (B) Evolution of force in chains A, B and C with simple shear in the 12-direction.

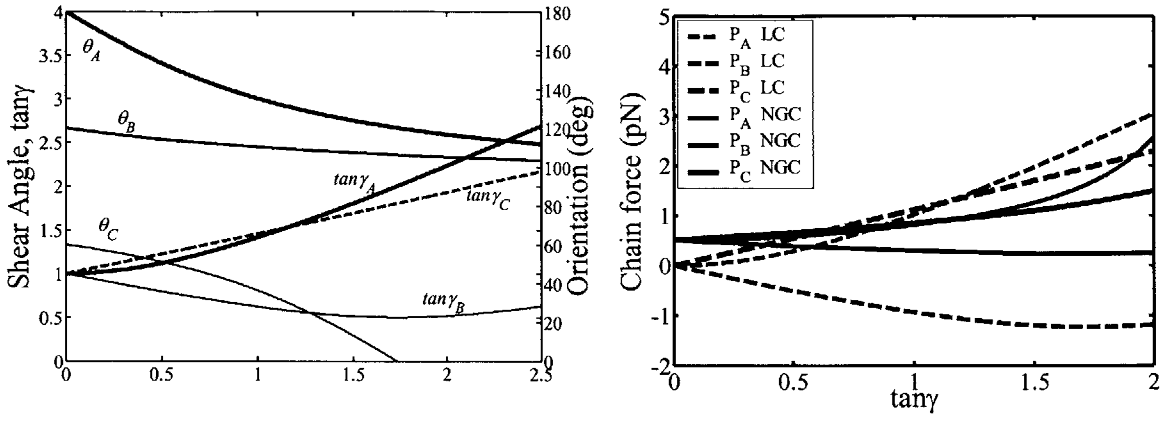

Fig. 2.18 *(A) Evolution of chain orientation and chain shear angle with respect to axis 1 for chains A, B and C for simple shear in the 21-direction. (B) Evolution of force in chains A, B and C with simple shear in the 21-direction.*

Figure 2.18. A and 2.18.B show the chain responses for simple shear in the 21-direction. All chains rotate towards alignment with the shear flow; chain A and C monotonically extend whereas Chain B first contracts then extends. The pretension prevents Chain B from experiencing compressive force during its contraction. Chain A extension governs the upturn in the macroscopic stress-strain behavior.

2.8 Pretension Effects

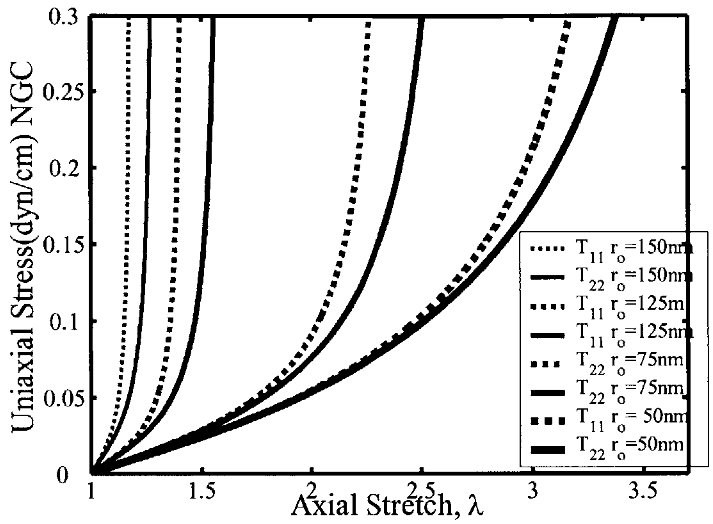

Fig. 2.19: *Effect of pretension on the uniaxial stress-stretch behavior.*

The initial end-to-end distance; $r_o = 75nm$ implies a pretension in the network (Qi et. al., 2005). The NGC behavior naturally captures this effect of pretension. Referring back to equation (11), we note that the chain force is zero when the end-to-end distance $r_o = 0$ and non-zero when $r_o \neq 0$; thus r_o sets the pretension of the network. To examine the influence of pretension on the membrane stress-stretch behavior, the value of r_o is varied. Changing r_o also corresponds to changing the areal density ν of the membrane. As r_o is increased, υ decreases. Figure 2.19 shows the uniaxial tensile behavior of the membrane for different r_o. Uniaxial tension in the 1-direction and in the 2-direction are both simulated for an r_o of 50*nm*, 75*nm*, 125*nm* and 150*nm*. As seen in Figure 2.20, as pretension is increased, the initial modulus of the membrane increases (even though the chain density decreases). Furthermore, increasing the pretension decreases the extensibility of the network as evidenced by the influence of increasing r_o on the macroscopic stretch at which an upturn in the stress-stretch curve is observed.

2.9 Summary

The mechanical behavior of the red blood cell membrane is governed by the lipid bilayer in the membrane and the spectrin network crosslinked to the bilayer. The lipid bilayer resists changes in planar area while posing little resistance to planar shear. The spectrin network provides shear stiffness to the membrane. In this chapter a continuum level constitutive model is proposed for the red blood cell membrane stress-stretch behavior for arbitrary general planar deformations. The cases of networks constituted of chains with linear force-extension behavior and for chains with non-Gaussian force-extension behavior are studied. The skeletal network of spectrin is approximated as a perfectly triangulated network. Uniaxial tension and simple shear behaviors of the membrane are simulated for the two different constituent chain behaviors in different directions. The macroscopic nonlinear stress-stretch behavior is found to be anisotropic at large deformations. The evolution in microstructure (chain stretches, forces, and orientations) is naturally monitored during macroscopic deformation thus capturing the effects of structural evolution on macroscopic mechanical loading behaviors and vice versa. The effect of pretension with stress-stretch behavior of the membrane is also studied; the initial modulus of the membrane is found to increase with chain pre-tension and the extensibility of the network is found to decrease with pretension. The proposed constitutive model can be used together with finite element modeling of the red blood cell to study complex deformation behaviors of the red blood cell; such cell deformation studies have been conducted by the Suresh group (Dao et al., 2003, Mills et al., 2004) utilizing the Evans, Skalak, Hochmuth neo-Hookean membrane model and, more recently, using a phenomenological higher-order I_1 (first stretch invariant) based constitutive model[1]. The proposed constitutive model also provides a framework to explore additional complexities on the mechanics of biomacromolecular network deformation including the effects of crosslinking proteins providing additional strain energy contributions during deformation, non-affine deformation in irregular triangulated networks (where mapping of macroscopic to microscopic deformation is not simply kinematically determined, but mechanical equilibrium must also be invoked), three-dimensional networked structures, and contributions of mechanically-induced unfolding. Unfolding of modular biomacromolecules such as spectrin has been experimentally observed to have dramatic consequences on the single molecule force-extension behavior (Rief et al., 1999, Law et al., 2003); the unfolding event has been incorporated into recent simplified "four-chain" network representations of membranes by Qi et al. (2005), whereby all chains experience the same stretching and thus unfold simultaneously. The triangulated network framework presented here provides a more physically-representative microstructure and will lead to unfolding in some sequential manner for the different chains as evidenced by the different evolutions in chain forces with macroscopic stretching presented in this work. The effects of incorporation of unfolding into the introduced triangulated network are presented in Chapter 3.

---

[1] We note that Arruda et al., (1993) and Boyce et al. (2000) and Boyce et al. (1996)have shown that higher order I_1-based models are phenomenological equivalents to non-Gaussian statistical models, in particular, to the 8-chain model of Arruda and Boyce (Arruda et al., 1993).

Chapter 3

Constitutive Modeling of the Stress-Stretch Behavior of 2-D Networks Containing Folded Domains

3.1 Introduction

The constituent spectrin chain molecules of the network consist of several folded modules. Each folded module will completely unfold with extension of the chains upon reaching a chain force between *25* to *35pN* depending on the extension rate and also the statistical distribution of the strength of the internal bonds of the module. Individual spectrin chains within the network will experience their first unfolding event at different levels of macroscopic strain depending on the loading conditions (uniaxial tension, compression, shear) and the orientation of each constituent chain with respect to the macroscopic loading. A microstructurally informed continuum level constitutive model is developed which tracks individual chain deformation behavior as well as the overall macroscopic network stress-strain behavior. In this chapter, using the introduced continuum approach and statistical mechanics based models of the chain force-extension behavior together with a transition state model of unfolding, a constitutive model for the membrane stress-stretch behavior is constructed. The stress-stretch behavior of the membrane under uniaxial tension and simple shear is simulated at large stretches. The evolving anisotropy of the network is shown. The influence of unfolding on the macroscopic stress-stretch behavior under various loading conditions is determined. The mechanical response of the network at different strain rates is compared.

3.2 Single Molecule Mechanics

Atomic Force Microscopy (AFM) and Optical Tweezers (Bustamante et al., 2003) make it possible to conduct direct measurements of single molecule force-extension behavior to track the evolution of deformation in the molecule (Figure 3.1.A). Length, extensibility and the folded vs. unfolded states of a folded domain are each important aspects of the function of a protein molecule. A protein molecule has a long chain repeating multi-domain structure. Spectrin is a cytoskeleton protein composed of repeats of *3* anti-parallel α-helices that form a coil-coil structure (Figure 3.1.B). Single molecule force-spectroscopy has been used to study the unfolding of spectrin-repeats by Rief et al. (1999) and by Law et al., (2003) (Figure 3.1.C).

Rief et al., (1999), Lenne et al., (2000), and Law et al., (2003) conducted mechanical experiments on single molecules to obtain the single molecule force-extension behavior and the force required to unfold the folded domains of the protein. Rief et al. (1999) worked with spectrin molecules, Immunoglobulin (Ig), the muscle protein titin and dextran. When spectrin molecules are extended beyond *100nm*, a characteristic pattern of peaks appears. The peak force is the unfolding force of a domain. The peak force is between *25-35 pN* when the spectrin modules are extended at a pulling speed of $0.3 \mu m/s$ (Rief et al., 1999). Rief et al. (1999) fit the unfolding traces to the WLC (worm-like-chain) force-extension equation to capture the force-extension behavior after each unfolding event (Figure 3.2.A); this fitting thus gave the length of molecular chain released with each unfolding event. The incremental increase in the molecular chain length was found to be *31.7nm*.

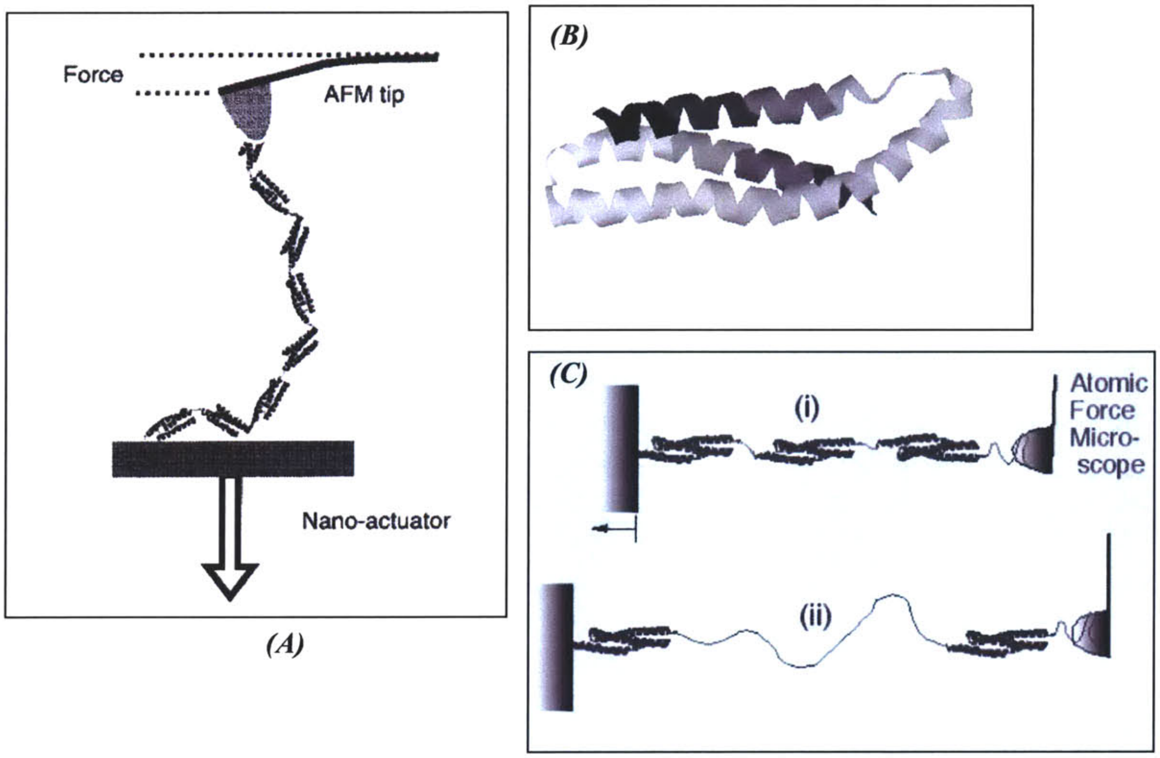

Fig. 3.1: ***(A)*** *Schematic of AFM (atomic force microscopy). Single proteins are attached to properly prepared surfaces and pulled with AFM tips (Rief et al., 1999),* ***(B)*** *Spectrin repeats consist of 3 anti-parallel α-helices (Pascual et al., 1997),* ***(C)*** *AFM experiment showing the unfolding of the spectrin repeats one by one in a all-or-non process (Discher et al., 2001).*

Rief et al. (1999) used a Monte Carlo simulation approach to capture the unfolding events. A combination of WLC to capture the force-extension behavior together with a thermodynamic two-state transition model to capture the rate-dependent unfolding force (and subsequent updating of the contour length of the WLC model) was used to capture the entire force-extension behavior.

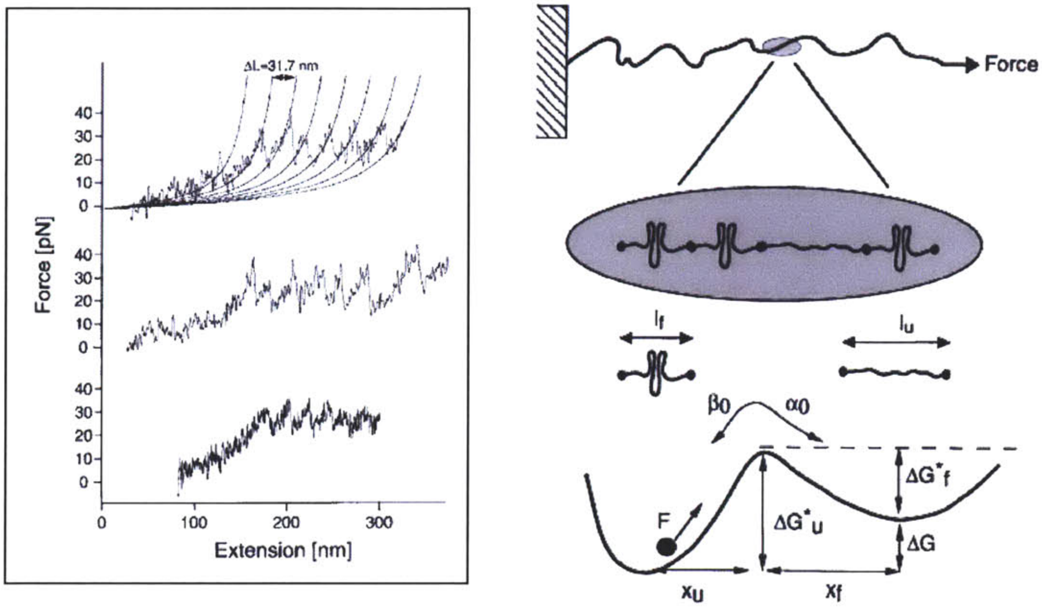

Fig. 3.2: ***(A)*** *Rief et al. (1999) fit the spectrin single molecule force spectroscopy experiments with a WLC fit,* ***(B)*** *Schematic of thermodynamic 2 state model. The applied force unfolds the folded domains along the chain one by one.* l_f *is the folded length of the module and* l_u *is its length when it is unfolded. There is an energy barrier of* ΔG^* *that the molecules have to overcome to unfold.* x_u *is the width of the activation barrier (Rief et al., 1998)*

According to the two state theory, spectrin modular domains can be modeled as being in one of two states; a module is either in the folded state, or it is in the unfolded state. To be able to transfer from the folded state to the unfolded state, an energy barrier of ΔG^* has to be overcome (Figure 3.2.B). Following Bell (1978), the energy barrier to translate from one state to the other is reduced by the applied force multiplied by the width of the activation barrier:

$$\omega(F) = \omega_o \exp\left(\frac{-(\Delta G - Fx_u)}{k_B\theta}\right) \tag{3.1}$$

where ω is the reciprocal of a diffusive relaxation time, F is the extension force on the molecule, x_u is the width of the activation barrier. For low forces (Izrailev et al., 1997), x_u and ω_o are assumed to be constant. In practice, terms in equation (3.1) can be lumped to give:

$$\omega(F) = \alpha \exp\left(\frac{Fx_u}{k_B\theta}\right) \tag{3.2}$$

where $\alpha = \omega_o\, exp(-\Delta G / k_B\theta)$; α and x_u are then obtained from the data of peak unfolding force as a function of the strain rate.

Rief applied the Monte Carlo Simulation algorithm to various molecules including dextran and spectrin to model the single molecule unfolding.

The Monte-Carlo algorithm to monitor the random unfolding events includes:

1. Stretching the single chain,
2. After each time step, determining the force using the WLC model force-extension expression as given in (2.17):

   $$f_C = \frac{k_B T}{A}\left(\frac{r}{L_C} + \frac{1}{4(1 - r/L_C)^2} - \frac{1}{4}\right) \tag{3.3}$$

   where r is the updated end-to-end distance, A is the persistence length, L_c is the initial contour length of the chain, k_B is the Boltzmann's constant and θ is the absolute temperature.
3. Calculating the unfolding frequency using (3.2): $\omega(F) = \alpha\, exp\,(Fx_u / k_B\theta)$,

4. Calculating domain unfolding probability, according to:

   $dP = m_t \omega \Delta t$ (always below 1)

where m_t is the number of folded modules in the chain during Δt.

5. Polling the domains to see their unfolding status.
6. If unfolding occurs, update the contour length of WLC and calculate the current force for that extension using the updated WLC parameters.
7. Repeat the steps by increasing the extension.

Upon extension of a molecule, unfolding of a single module occurs when the nonlinear rise in the force reaches a peak, where upon unfolding gives a load drop. The modules unfold one by one (Discher and Carl, 2001), giving the force-extension curve a "saw-tooth pattern" due to unfolding which gives a repeating sequence of a force rise with extension to a peak followed by a load drop, rise to a peak and drop etc.

3.3 Network Mechanics

The Rief et al. (1998) use of a transition state energy criterion for unfolding for single molecules can be incorporated to model the unfolding behavior of the chains in the spectrin network. This method has also been followed by Qi et al. (2005) in which an idealized "four-chain" two-dimensional planar network representation is used to model the spectrin network. The four chain network possesses a perfectly staggered arrangement of crosslinks as shown in Figure 3.3. Qi et al. (2005) mapped the macroscopic stretch state onto the network obtaining the chain stretch as a function of macroscopic membrane stretch. Given the chain stretch, they used FJC and WLC to obtain the chain force and the transition state model to trigger module unfolding when the chain force reached critical conditions.

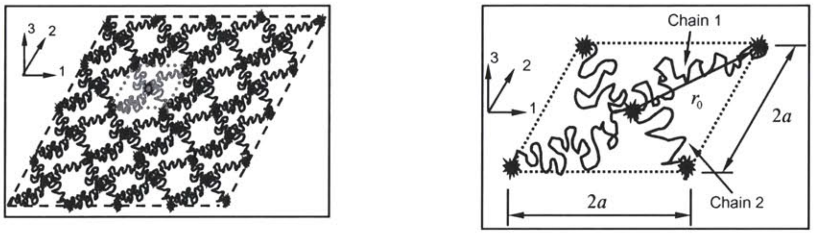

(A) ***(B)***

Fig.3.3: ***(A)*** *Qi et al.'s idealized planar network for modeling the spectrin network,* ***(B)*** *representative volume element (RVE) of the given network (Qi et al., 2005).*

Qi et al. (2005) introduced statistical distributions of sources of randomness in their simulations. For example, the range of the peak force at which unfolding happens has been found to vary in the experiments even at a given strain-rate. Law et al. (2003) observed spectrin unfolding to occur at forces ranging from *~10 pN* to *~37 pN* at extension rates of *1 μm/s*. Whereas Rief et al. (1998) noted that the peak force is between *25-35 pN* when the spectrin repeats unfold with a pulling speed of 0.3μm/s. This randomness can be introduced by considering a range in ΔG, the energy barrier required to overcome unfolding in the simulation. Or similarly, α can be chosen to vary over a range. This range is calculated to be $\alpha = .000125\text{-}.0079\ /s$ (Qi et al., 2005) using Law et al. (2003)'s experimental results.

The energy criterion can be implemented using a Monte Carlo simulation. Using Rief's approach for the single molecule simulation, in each time increment, the domain unfolding probability is calculated by:

$$dp = m_f \omega \Delta t \tag{3.4}$$

Here m_t is the number of folded modules, and Δt is the time increment.

For each macromolecule, an α is generated through a random Gaussian number generator based upon the distribution in unfolding force data of Law et al. (2003). In the Monte Carlo simulation, a random number, p, ($0<p<1$), is generated at each step. This random number is chosen out of a Gaussian distribution, using a predefined function in MATLAB. This number is then compared with dp. If $dp>p$, unfolding occurs. Unfolding acts to release additional rigid links. Therefore, the number of current folded modules, the number of effective links and the contour length are then updated when a module unfolds. A new α is generated. If unfolding does not happen, the loop goes to the top with the next time increment. The unfolding events are simulated to follow transition state theory with additional randomness imparted through a random selection of ΔG.

This method of using transition state theory as the unfolding criterion for single molecules can be incorporated into our triangulated network. After application of membrane deformation, the status of all three chains, chain A, chain B and chain C are monitored. The stretch (and force) in each chain will, in general, be different depending on the macroscopic deformation and therefore the three chains will not unfold at the same time. Therefore, the properties of each chain is updated separately. Because the deformation evolves much differently in all three molecules and because each molecule unfolds at different points during the overall deformation, this would result in a higher degree of anisotropy than observed when unfolding does not occur.

Prior to unfolding, the number of the effective rigid links along the chain is:

$$N(t=0) = n - m(t=0)(q-1), \tag{3.5}$$

where n is the total number of rigid Kuhn links, m is the number of folded modules and q is the number of links in a folded module (Qi et al., 2005). The equation suggests that, when the links in a module are folded, the module itself is taken as one effective link. When a module unfolds, the number of folded modules decrease by 1, since the unfolding process requires that a module completely unfold upon reaching a certain unfolding criterion. This argument implies:

$$m(t=t_1) = m(t=0) - 1. \tag{3.6}$$

After one module unfolds, the effective number of rigid links at $t = t_1$, $N(t=t_1)$ is updated according to:

$$N(t=t_1) = n - m(t=t_1)(q-1). \tag{3.7}$$

The contour length, L_C, of the molecule increases, giving a new contour length of :

$$L_C(t=t_1) = N(t=t_1)l, \tag{3.8}$$

where l is the length of the rigid links.

In this thesis work, all formulations are presented using the FJC to represent chain behavior.

3.4 Determination of Material Properties

Table 3.1: *Spectrin properties*

Model Parameters (FJC)	***Spectrin Network***
Initial end-to-end distance, r_o (nm)	75
The areal chain density, ν (1/m^2)	6.1 (10^{14})
Number of Kuhn segments along the chain, N	19
Absolute temperature, θ (K)	300
Persistence length, l (nm)	10.25
Initial contour length (nm), L_0	180
Increase in contour length due to unfolding, ΔL (nm)	28.8
Activation barrier width, x_u (nm)	1.7

The width of the activation barrier, x_u, is defined to be $x_u = 1.7nm$ from fitting the experimental data (Rief et al., 1999). The persistance length, l, has been used as $10.25nm$ (Discher et al., 1997) in *Chapter 2* for the spectrin network. It's worth here to note that, although $l = 10.25nm$ for the network proteins, because of the complications, such as complicated heterodimer structure or the spectrin interactions with other proteins, this number reduces to *l=1.6nm* in single molecule behavior experiment and calculations (Qi et al., 2005). Another parameter that is predefined is the increase in the contour length of the chains with each unfolding event. *ΔL= 28.8nm* is defined from the FJC fit to Rief's single molecule data, also and the number of folded modules prior to unfolding is found to be *m=7*, shown in Figure 3.4 (Qi et al., 2005). The range in which α varies is α = *0.000125 – 0.0079/s* (Qi et al., 2005). The properties are summarized in Table 3.1.

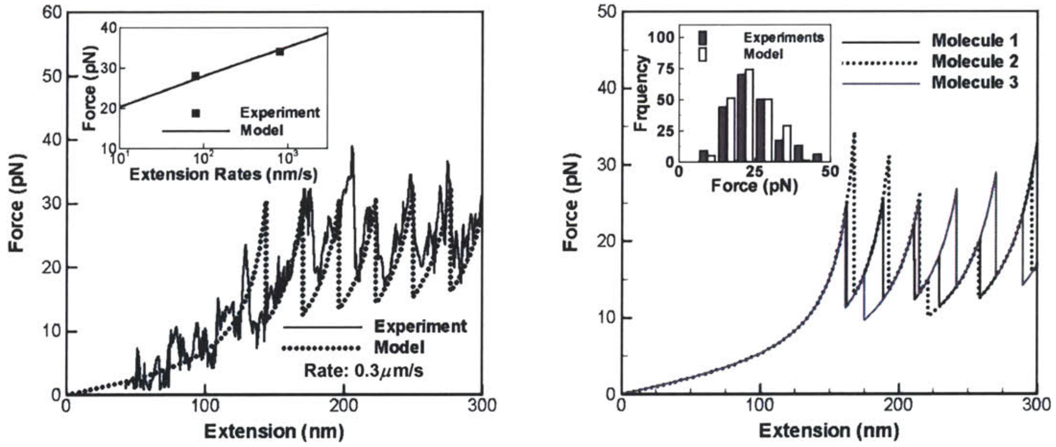

(A) ***(B)***

Fig. 3.4: *FJC fit to Rief et al. (1999)'s experimental data:* ***(A)*** *Spectrin force versus extension behavior; the inset shows the dependence of unfolding force on extension rate;* ***(B)*** *Predicted force versus extension behavior for spectrin (1 μm/s) using a distribution in unfolding barrier based on Law et al. (2003) data. (Qi et al., 2005)*

3.5 Uniaxial Tensile Behavior

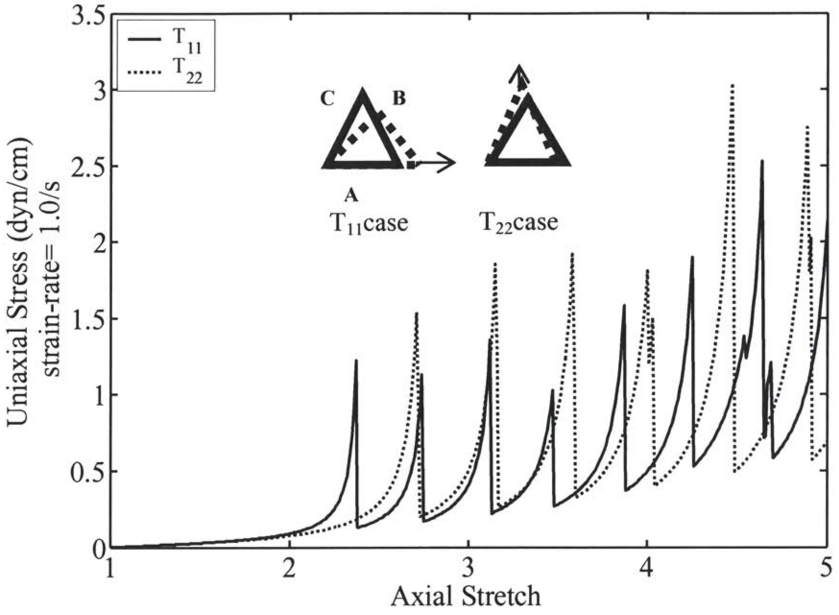

Fig. 3.5: *Stress-stretch behavior of the membrane under uniaxial tension in the 1- and 2-direction at a strain rate of 1.0/s. In the inset, is the loading conditions are shown with the deformed configuration depicted by the dashed lines.*

Figure 3.5 shows the stress-stretch behavior of the network under an application of uniaxial stress in the 1-direction and in the 2-direction at a strain-rate of *1.0/s*.

Under a uniaxial stress in the 1-direction, the first unfolding event happens at a macroscopic stretch of $\lambda_1=2.35$. The unfolding stress goes up to *1.2 dyn/cm*. Once unfolding occurs, the stress drops since the contour length of the chain(s) which have had a domain unfold increased and the configurational entropy of those chains have increased and their corresponding extensional force decreased. Then the stress starts increasing nonlinearly again with further extension, but this time with a slope less than the initial slope, again because of the contour length of the chains that unfolded acting to increase their compliance.

As the membrane is axially stretched, its cross-sectional area decreases which leads to an increased macroscopic stress level at which unfolding occurs. This nonlinear increase in the overall peak stress level is due to the macroscopic shape change (geometric nonlinearity) with increasing deformation. As the tensile stress in the 1-direction increases, the area over which the load is acting decreases (Figure 3.6, inset) which increases the stress on the network. Figure 3.6 shows the nominal stress behavior of the network in uniaxial stress in the 1-direction. The nominal stress curve has a plateau-like region at an unfolding stress of 0.3 dyn/cm.

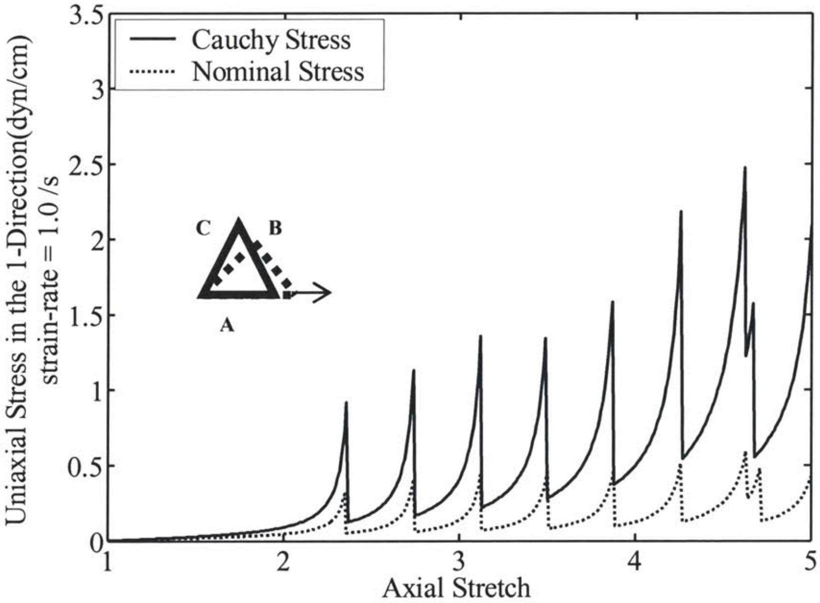

Fig. 3.6: *Stress-stretch behavior of the membrane under uniaxial tension in the 1-direction at a strain rate of 1.0/s. Cauchy Stress and Nominal Stress are compared.*

To understand the meaning of the macroscopic stress-stretch plot better, we examine the behavior of individual constituent chains of the network under the same loading: uniaxial tension in the 1-direction.

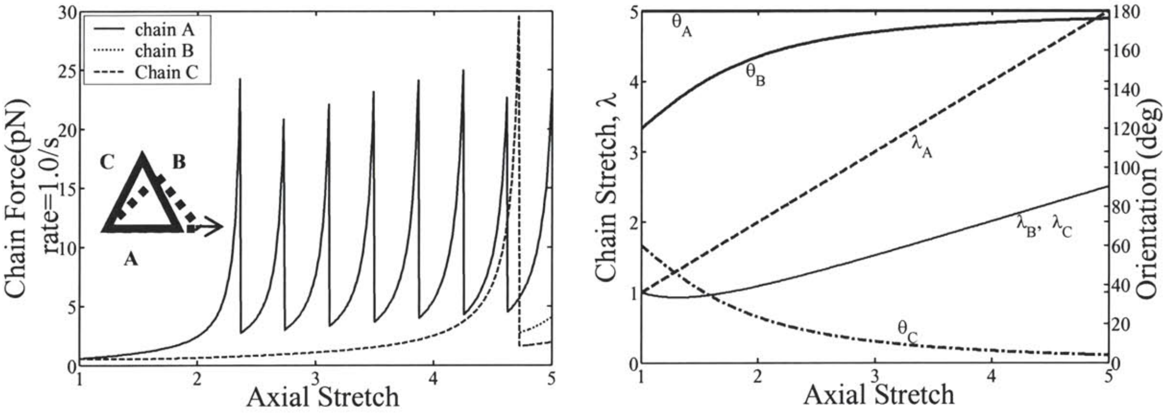

(A) **(B)**

Fig. 3.7: ***(A)*** *Chain force-extension behavior in the RVE under uniaxial tension in the 1-direction,* ***(B)*** *Chain stretch and orientation evolution with macroscopic stretch.*

Figure 3.7 shows the force vs. macroscopic stretch behavior of chains A, B, C, as well as the chain stretches and orientations under the applied deformation. Since chain A is aligned with the axis of deformation, it is the chain to first undergo unfolding. When the links of chain A align towards the 1-direction and the chain is fully-extended, $r_A = L_{contour} = 180nm$, the first unfolding event occurs. The chain stretch corresponding to the first unfolding event is:

$$\frac{r}{r_O} = \frac{180nm}{75nm} = 2.4 \qquad (3.9)$$

This estimation is true since chain A is nearly aligned with the axis of deformation. The folded molecules in chain A totally unfold, corresponding to 7 peak forces ($m = 7$), before reaching a stretch of $\lambda = 5$. The peak force at which unfolding events happen differs every time because of the random distribtion of unfolding barrier introduced in the simulation following the data of Law et al. (2003).

Chains B and C rotate and stretch with the applied macroscopic deformation because of the geometry of the RVE. The rotation of these chains accomodates much of the imposed deformation and therefore their chain stretch levels are substantially lower, thus delaying unfolding of these chains. The first unfolding of chains B and C occur at a macroscopic stretch of λ_1=4.65 and only one module unfolds under the applied deformation. Unfolding of chains B and C affect the overall stress-stretch behavior as seen in Figure 3.6. At a stretch level of λ_1=4.65, after the stress curve peaks up and before it drops a considerable amount , it rises up again and then drops much more this time because of the additional effects coming from the unfolding of chains B and C in addition to that of chain A.

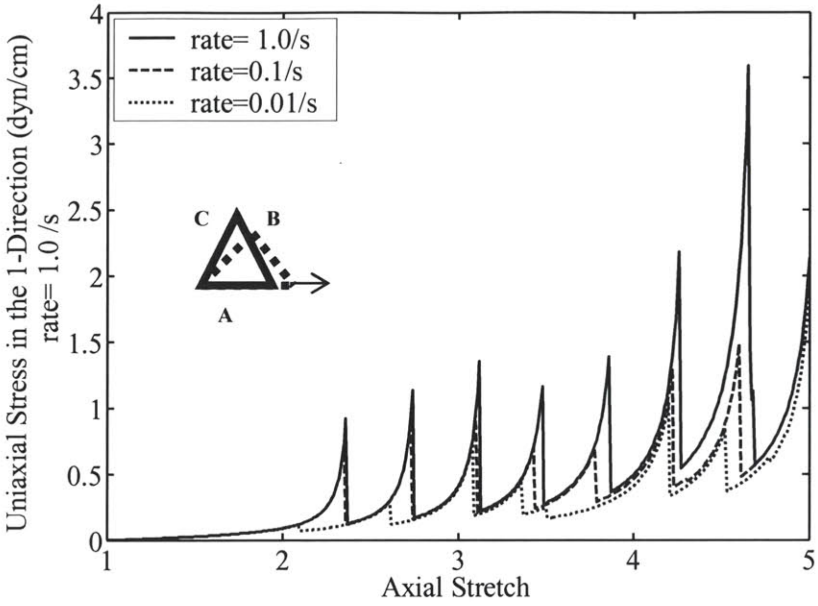

Fig. 3.8: *The strain-rate dependence of the stress-stretch behavior of the membrane under uniaxial tension in the 1-direction.*

Figure 3.8 shows the strain rate dependence of the stress-stretch curve under uniaxial tension in the 1-direction.

When the strain rate is decreased, as the maximum strain is the same and the number of steps are defined to be constant, according to:

$$strain\_rate = \frac{maximum\_strain}{\#steps * \Delta t}, \tag{3.10}$$

the time increment, Δt increases. When Δt increases, following:

$$\Delta t = \frac{dp}{m_t \omega_u} = \frac{dp}{m_t \alpha \, \mathbf{exp}\left(\frac{f_c x_u}{k_B \theta} \right)}, \tag{3.11}$$

the unfolding probability increases, which results in earlier unfolding. Therefore, the peak force of unfolding decreases and as a consequence, the stress for unfolding is lower.

When the strain rate is as low as 0.01/s, the stress peaks and drops are not very clear, the curve is more like a smooth nonlinear curve.

When a strain rate of 1.0/s is applied to the macromolecule, the individual extension rates of the chains can be calculated using geometry, also equations (2.8) and using:

$$Extension\_rate = \frac{maximum\_extension}{total\_time}. \qquad (3.12)$$

For uniaxial tension in the 1-direction, i.e. $\boldsymbol{F} = \begin{bmatrix} F_{11} & 0 \\ 0 & 1/F_{11} \end{bmatrix}$, for a maximum stretch of $\lambda = 5$, maximum extensions of the individual molecules are calculated from geometry following Equations (2.8):

$$\begin{aligned} &\lambda\mathbf{max}_A = \sqrt{F_{11}^2 + F_{21}^2} = F_{11}\mathbf{max} = 5, \\ &\lambda\mathbf{max}_B = \frac{1}{2}\sqrt{\left(F_{11} - F_{12}\sqrt{3}\right)^2 + \left(F_{21} - F_{22}\sqrt{3}\right)^2} \\ &= \frac{1}{2}\sqrt{F_{11}\mathbf{max}^2 + \frac{3}{F_{11}\mathbf{max}^2}} = \frac{1}{2}\sqrt{5^2 + \frac{3}{5^2}}, \\ &\lambda\mathbf{max}_C = \lambda\mathbf{max}_B. \end{aligned} \qquad (3.13)$$

Using these equations, since the total time of deformation is the same for all the molecules, the individual extension rates can be calculated. The individual extension-rates are given in Table 3.2.

Table 3.2: *Mapping individual extension-rates of chains under uniaxial tension in the 1-direction.*

Macroscopic Strain Rate (1/s)	***Chain A Extension Rate (μm/s)***	***Chain B Extension Rate (μm/s)***	***Chain C Extension Rate (μm/s)***
1.0	0.225	0.113	0.113
0.1	0.0225	0.0113	0.0113
0.01	0.0022	0.0011	0.0011

The initial contour length of the spectrin chains are observed to range from *150nm-210nm* (Qi et al., 2005). Therefore next approach will be to take this distribution into account. In the code constructed, the chains are randomly asigned contour lengths in the given range and the effects of that distribution on the stress-stretch curve are plotted (Figure 3.9) for two different simulations.

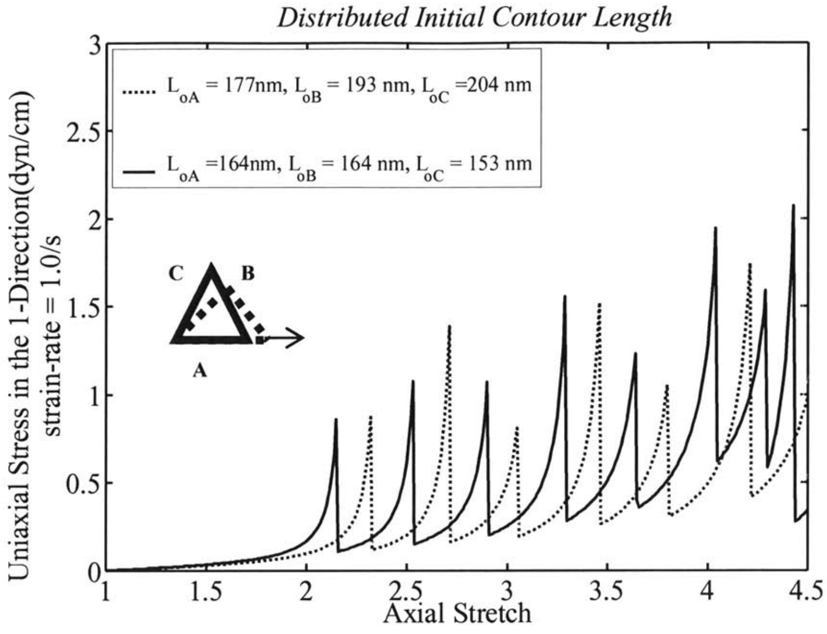

Fig. 3.9: *The initial contour length dependence of the stress-stretch behavior of the membrane under uniaxial tension in the 1-direction.*

The average initial contour length of the first simulation (dashed line in Figure 3.10) is *(177 nm + 193 nm + 204 nm) / 3 = 191 nm*. The average initial contour length of the second simulation (solid line in Figure 3.9) is *(164 nm + 164 nm + 153 nm) / 3 = 160 nm*. Unfolding occurs earlier in the shorter initial contour length (*160 nm*) case.

When uniaxial stress in the 2-direction is applied to the model, the dominating chains that govern the unfolding behavior are chains B and C. Chain A gets compressed under the applied deformations seen from the sketch in the inset of Figure 3.5. The stresses in Figure 3.5, for uniaxial tension in the 2-direction are twice as large as the stresses for uniaxial tension in the 1-direction. The reason behind this is in uniaxial tension in the 2-direction, the contributions to the overall stress comes from chains B and C whereas during uniaxial tension in the 1-direction, the contribution is primarily from chain A until very large stretches.

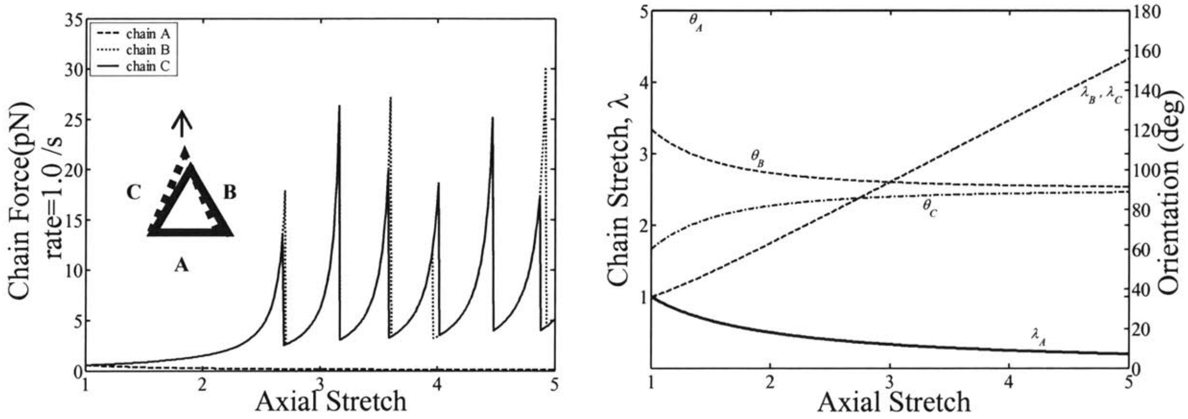

Fig. 3.10: ***(A)*** *Chain force-extension behavior in the RVE under uniaxial tension in the 2-direction,* ***(B)*** *Chain stretch and orientation evolution with macroscopic stretch.*

Figure 3.10 shows the force-extension behaviors of the chains under uniaxial tension in the 2-direction, as well as how the stretch evolves in individual chains. The first unfolding happens at a stretch of λ_2=2.7. This can also be seen in Figure 3.5. The unfolding for uniaxial tension in the 2-direction is delayed in comparison to the loading in the 1-direction since the dominating chains undergo rotation as well as stretching. This geometric consequence creates totally different responses in the stress-stretch behavior when the macromolecule is pulled in different directions. The reason why the responses of chains B and C are different is due to the random distribution of unfolding barrier introduced by unfolding events' nature.

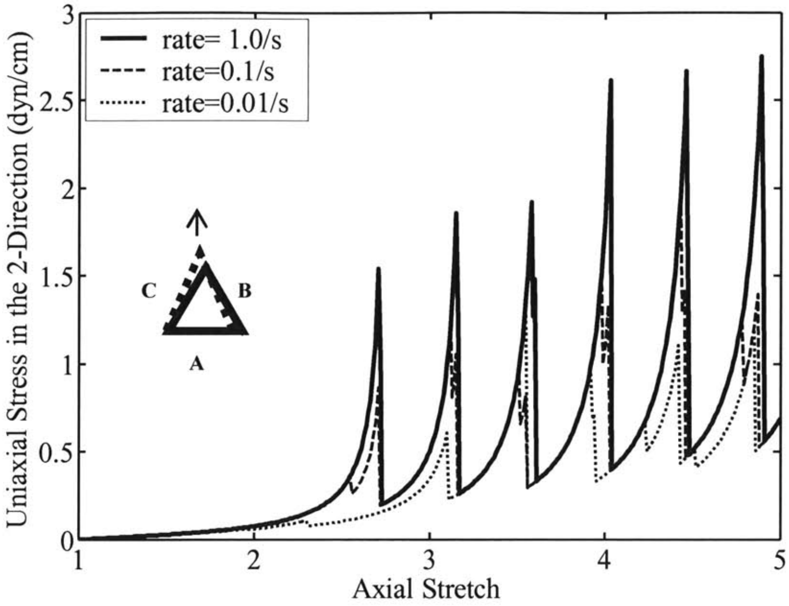

Fig. 3.11: *The strain rate dependence of the stress-stretch behavior of the membrane under uniaxial tension in the 2-direction.*

Figure 3.11 shows the different stress responses when the network is deformed at strain-rates of 0.01/s, 0.1/s, 1.0/s. Similar arguments about the strain rate apply to this case as well.

For uniaxial tension in the 2-direction, i.e. $\boldsymbol{F} = \begin{bmatrix} 1/F_{22} & 0 \\ 0 & F_{22} \end{bmatrix}$, for a maximum stretch of $\lambda = 5$, maximum extensions of the individual molecules are calculated from geometry following Equations (2.8):

$$\lambda max_A = \sqrt{F_{11}^2 + F_{21}^2} = \frac{1}{F_{22max}} = \frac{1}{5},$$

$$\lambda max_B = \frac{1}{2}\sqrt{\left(F_{11} - F_{12}\sqrt{3}\right)^2 + \left(F_{21} - F_{22}\sqrt{3}\right)^2}$$
$$= \frac{1}{2}\sqrt{\frac{3}{F_{22max}^2} + F_{22max}^2} = \frac{1}{2}\sqrt{\frac{3}{5^2} + 5^2}, \qquad (3.14)$$

$$\lambda max_C = \lambda max_B.$$

Using these equations, since the total time of deformation is the same for all the molecules, the individual extension rates can be calculated. The individual extension-rates are given in Table 3.3.

Table 3.3: *Mapping individual extension-rates of chains under uniaxial tension in the 2-direction.*

Macroscopic Strain Rate (1/s)	***Chain B Extension Rate ($\mu m/s$)***	***Chain C Extension Rate ($\mu m/s$)***
1.0	0.195	0.195
0.1	0.0195	0.0195
0.01	0.0019	0.0019

The individual extension-rates under the same macroscopic strain rate are lower in the case of Uniaxial Tension in the 2-direction (~ *0.195* $\mu m/s$) than in Uniaxial Tension in the 1-direction (~ *0.225* $\mu m/s$) as given in tables 2 and 3 . The reason is because the chains which govern the motion; B and C, in Uniaxial Tension in the 2-direction case, not only stretch but also rotate with the applied deformation. However, in Uniaxial Tension in the 1-direction, chain A, which is the chain basically dominating the deformation of the membrane, only stretches with the applied deformation.

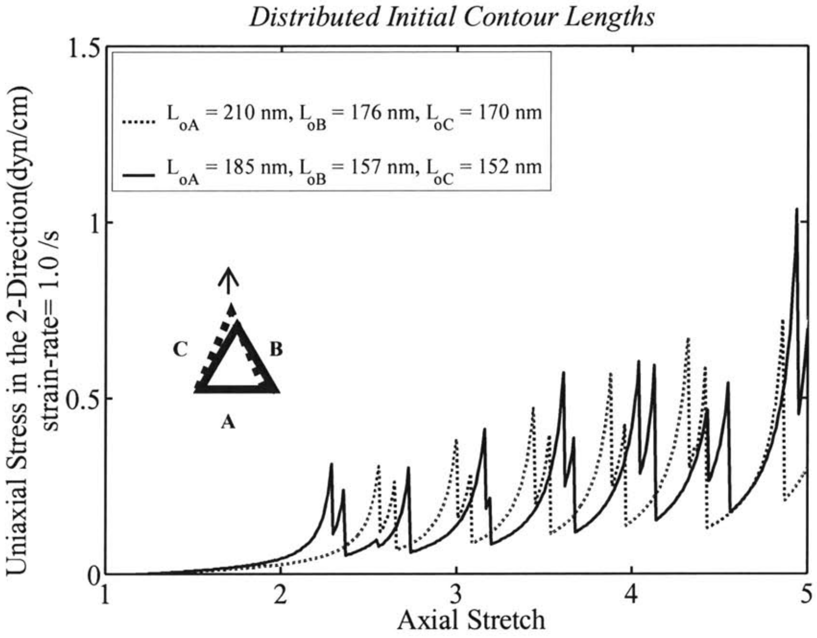

Fig. 3.12: *The initial contour length dependence of the stress-stretch behavior of the membrane under uniaxial tension in the 2-direction.*

Figure 3.12 shows the effects of possible distributions in the initial contour lengths of the chains on the stress-stretch behavior of the network. Average initial contour lengths of *(210 nm + 176 nm + 170 nm) / 3 = 185 nm* and *(185 nm + 157 nm + 152 nm) / 3 = 165 nm* are compared. When the average initial contour length is decreased, the stretch at which unfolding occurs is lower.

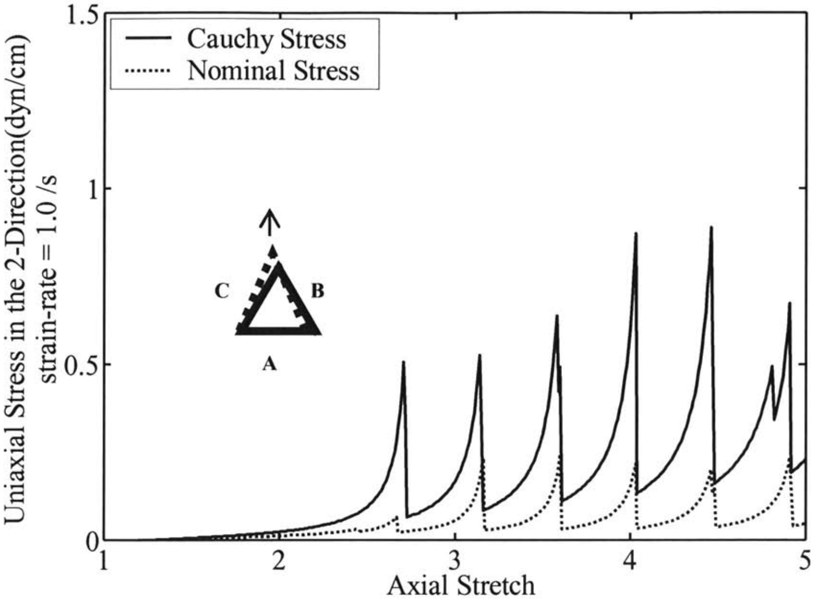

Fig. 3.13: *Stress-stretch behavior of the membrane under uniaxial tension in the 2-direction at a strain rate of 1.0/s. Cauchy Stress and Nominal Stress are compared.*

Figure 3.13 shows the nominal stress vs. stretch and compares it to Cauchy stress vs. stretch curve. The peak stresses are almost the same for the nominal stress curve (~ *0.2 dyn/cm*).

3.6 Simple Shear Behavior

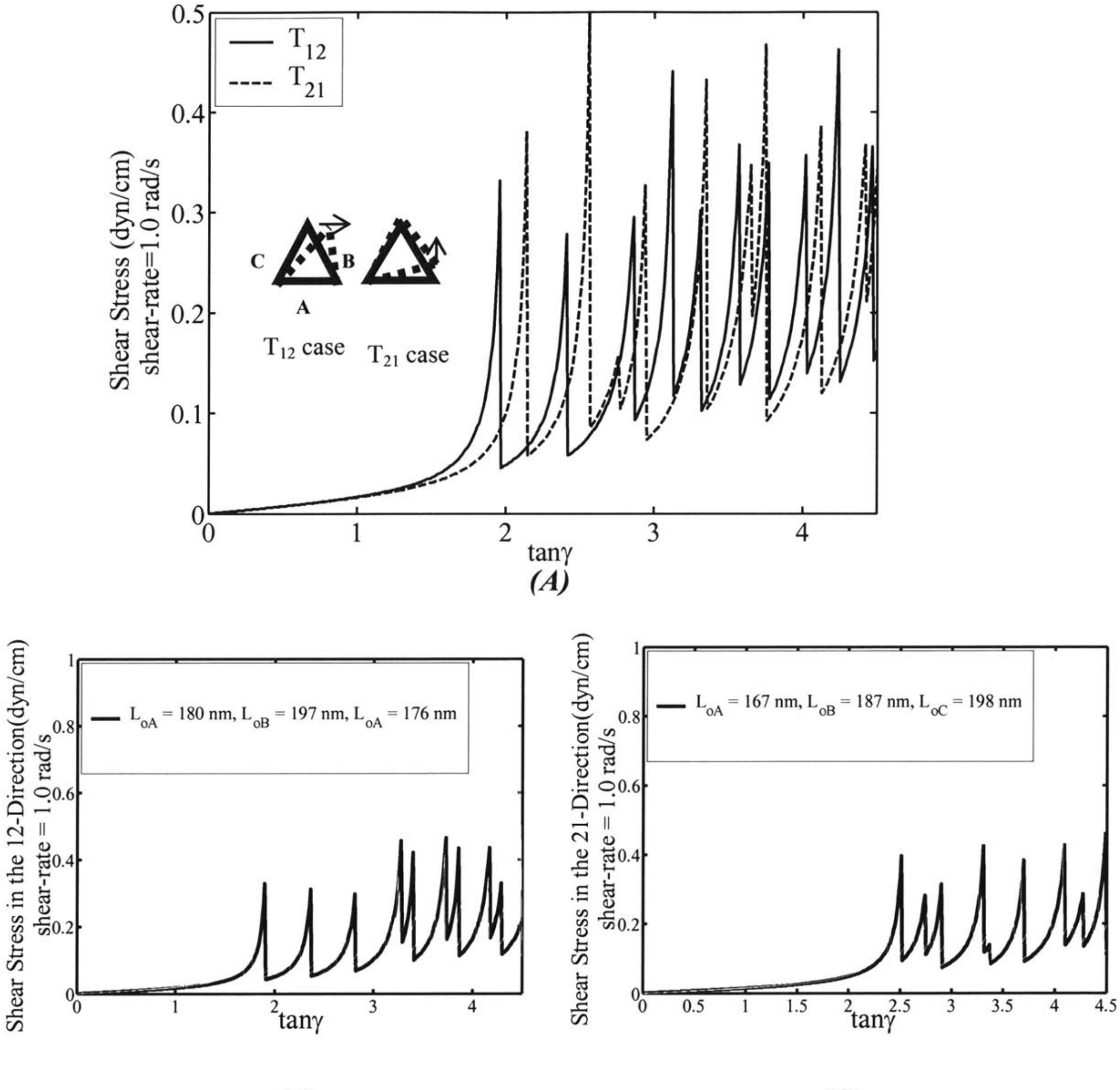

(A)

(B) *(C)*

Fig.3.14: ***(A)*** *Shear Stress vs. Shear angle behavior of the membrane under shear in the 12- and 21-directions at a strain rate of 1.0 rad/s. In the inset, is the loading conditions are shown with the deformed configuration depicted by the dashed lines,* ***(B)*** *Shear Stress vs. Shear angle behavior of the membrane under shear in the 12-direction using distributed initial contour lengths,* ***(C)*** *Shear Stress vs. Shear angle behavior of the membrane under shear in the 21-direction using distributed initial contour lengths.*

Figure 3.14 shows the shear stress vs. shear angle, $\tan\gamma$, behavior of the network at a shear rate of 1.0 rad/s. At this shear rate, in the case of uniform initial contour lengths, when shear is applied in the 12-direction, the first unfolding happens at $\mathbf{tan}\,\gamma = 1.97$, while for shear in the 21-direction, the first unfolding happens at $\mathbf{tan}\,\gamma = 2.2$. The shear angles at which the network experiences initial unfolding is very close for shearing in different directions, meaning, the anisotropic response in the shear case is less than the anisotropy in the tension case, as mentioned in Chapter 2.

In order to look into the network shearing behavior in more detail, one can study the force-extension behavior of the individual chains.

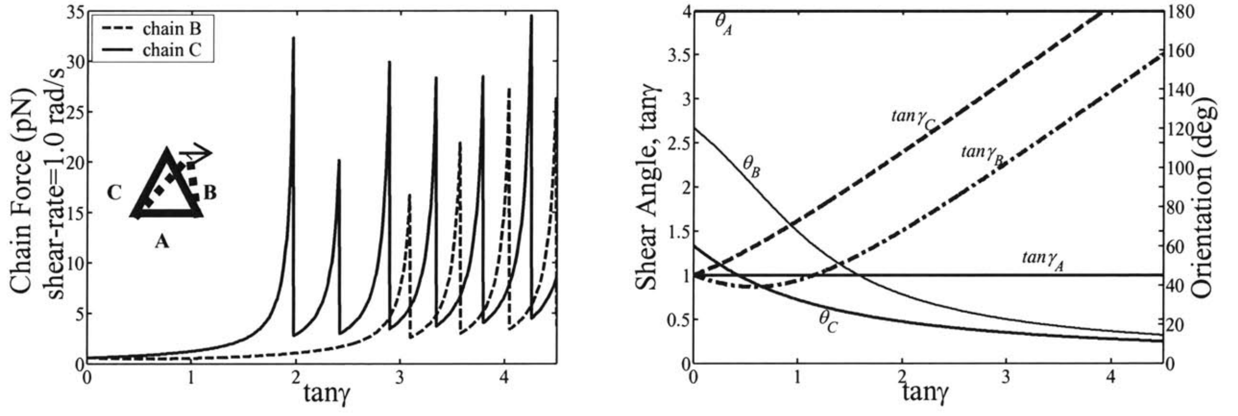

(A) ***(B)***

Fig. 3.15: *(A) Chain force-extension behavior in the RVE under shear in the 12-direction,* ***(B)*** *Shear angle and chain orientation evolution with macroscopic shear deformation.*

Figure 3.15 shows how the chain force (A), chain stretch and chain orientation (B) varies with the macroscopic deformation for shearing in the 12-direction. When shear is applied in the 12 direction, only chains B and C are deformed, they stretch and rotate with the deformation. Chain B compresses until it makes an angle of $\theta_B=90^0$ with the 1 direction. Therefore chain B starts to stretch after $\mathbf{tan}\,\gamma_B = 0.6$ as seen Figure 3.15 (B). This delayed stretching behavior results in chain C initiating the unfolding in the overall RVE. Therefore, the stress-shear angle plot shows an initial unfolding behavior which is identical to chain C's unfolding behavior. Chain B starts unfolding at a shear angle of $\mathbf{tan}\,\gamma = 3.1$ which results that the stress-shear angle curve (Figure 3.15.A) to fluctuate around the same shear angle.

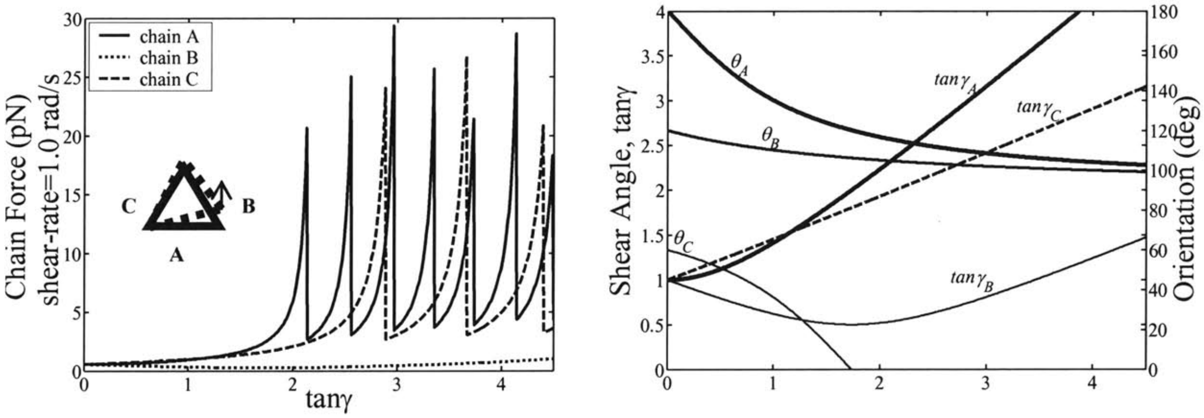

(A) ***(B)***

Fig. 3.16: ***(A)*** *Chain force-extension behavior in the RVE under shear in the 21-direction,* ***(B)*** *Shear angle and chain orientation evolution with macroscopic shear deformation.*

In shear 21 case, all the chains deform, but they unfold at different times. Chain A is the first molecule to unfold (Figure 3.16), therefore dominates the initiation of the peak stress in shear stress-shear angle profile (Figure 3.14.A). Chain B, whose behavior is shown in the inset, compresses under the applied deformation until a deformation of $\mathbf{tan}\,\gamma = 1.75$

and until it makes an angle of $\theta_B=180^0$ with the 1 direction as seen in Figure 3.16.B. Chain B does not unfold under the applied deformation.

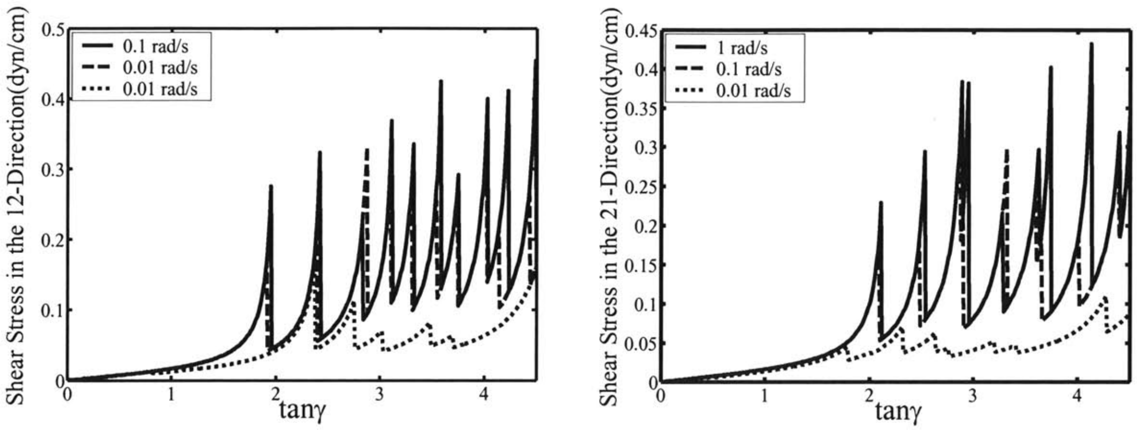

(A) ***(B)***

Fig. 3.17: *The strain rate dependence of the stress-stretch behavior of the membrane under shear in the* ***(A)*** *12- and* ***(B)*** *21-directions.*

Figures 3.17 shows the shear rate dependence of the shear stress vs. shear angle, $\mathbf{tan}\,\gamma$, of the network for shear rates of 0.01 rad/s, 0.1 rad/s and 1 rad/s for shear in 12 (A) and in 21 (B) directions.

3.7 Summary

The constituent chains of the spectrin network consist of several folded modules. Unfolding of these folded modules can be triggered by the application of large deformation to the macromolecular network, depending on the extension rate and also the statistical distribution of the strength of the internal bonds of the module. The force-extension behavior of a single modular macromolecule exhibits a "saw-tooth" pattern due to unfolding giving a sequence of force rise to a peak followed by a load drop, rise to a peak and drop etc. In this chapter, using the introduced continuum approach together with single molecule force-extension behavior and with a transition state model of unfolding, large deformation behavior of two-dimensional networks of biomacromolecules is studied. Uniaxial tension and simple shear behaviors of the membrane are simulated incorporating the unfolding of the individual chains. The three chains do not unfold at the same time since the stretch (and force) in each chain is different depending on the macroscopic deformation. Because the deformation evolves much differently in all three molecules and because each molecule unfolds at different points during the overall deformation, this results in a higher degree of anisotropy than observed when unfolding does not occur. The effect of the strain-rate on the mechanical response is also investigated in this chapter. When the strain-rate is as low as 0.01/s, the stress peaks and drops do not come out to be very clear. The variation in the extension-rates of the individual chains under different loading conditions is presented. The extension-rate of the dominating chain in that specific loading condition is found to be higher than that of the other chains in the RVE under a given macroscopic strain-rate. The proposed model includes a combination of FJC to capture the force-extension behavior together with a thermodynamic two-state transition model to capture the rate-dependent unfolding force. The force-extension behaviors of individual chains of the RVE incorporated to define the stress-stretch behavior of the spectrin network, can be used to serve as a model for three-dimensional solids that have a similar microstructure, such as the cytoskeleton and the networked microstructure of soft tissues.

Chapter 4

Summary and Future Work

Many biological, natural and synthetic materials possess a networked and/or micro/nano-truss-like microstructure. In this thesis work, a general microstructurally-informed continuum level constitutive model of the large stretch behavior of membranes possessing a triangulated network or truss-like structure is developed. As a specific example, a constitutive model of the stress-strain behavior of the red blood cell membrane is developed; this model directly incorporates the microstructure of the spectrin network. The skeletal network of spectrin is approximated as a perfectly triangulated network. The cases of networks constituted of chains with linear force-extension behavior, for chains with non-Gaussian force-extension behavior, and for modular chains which exhibit a non-Gaussian behavior together with unfolding of the folded modules are studied. The model provides a description of the deformation behavior of the membrane when subjected to an arbitrary planar deformation gradient. Furthermore, the proposed model monitors the evolution of force, stretch and orientations of the microscopic constituent chains of the network under large deformations. The approach undertaken was to define the RVE (Representative Volume Element) of the triangulated network to track the microscopic deformation in each constituent chain as a function of imposed macroscopic deformation. The strain energy contribution for each chain is then determined and contributes to the strain energy density function of the membrane. Using continuum mechanics, the macroscopic stress-stretch behavior of the network is derived from the strain energy density function. The constituent chains of the spectrin network exhibit a highly nonlinear force-extension behavior. Therefore, the force-extension behavior of the chains is modeled using the FJC (Freely Jointed Chain) model (see, for example, Treloar (1958)). Deviation from the linear chain model is also highlighted in the studies. The macroscopic nonlinear stress-stretch behavior is found to be anisotropic at large deformations. The effect of the pretension in the undeformed configuration of the network on the stress-stretch behavior of the membrane is also studied in Chapter 2 of this thesis work.

In Chapter 3, the "saw-tooth pattern" observed in single molecule studies (Rief et al., 1999, Law et al., 2003) of the spectin repeats is incorporated into the model presented in Chapter 2. Unfolding of the folded modules of the constituent chains of the spectrin network can be triggered by extension of the molecules. Unfolding depends on the extension rate and also the statistical distribution of the strength of the internal bonds of the module. Using the introduced continuum approach together with single molecule force-extension behavior and with a transition state model of unfolding, large deformation behavior of two-dimensional networks of biomacromolecules is studied, monitoring the effects of the individual module unfolding of the constituent chains of the RVE. The effect of the strain-rate on the mechanical response is also investigated in Chapter 3.

The deformation of the proposed perfectly triangulated network model is an affine deformation, and is completely kinematically prescribed by the applied deformation gradient. The proposed constitutive model also provides a framework to explore additional complexities on the mechanics of biomacromolecular network deformation such as; non-affine deformation in irregular triangulated networks, where mapping of macroscopic to microscopic deformation is not simply kinematically determined, but mechanical equilibrium must also be invoked. The RVE of the irregular triangulated network, composed of chains with different lengths, can be chosen to be an irregular hexagon with periodic boundary conditions. The constitutive chains of this RVE have different axial stiffness' to be able to accommodate the pretension in the spectrin network. Using the periodic boundary conditions together with force equilibrium equations, a constitutive model can be introduced for this network with an RVE composed of irregular triangles. The constitutive model proposed in Chapter 2 can be incorporated with the material behavior of the irregular triangulated network, to be able to define the mechanical behavior of a random microstructured network of triangles. This incorporation would serve as a more realistic approximation of the mechanical behavior of the spectrin network.

The methodology introduced in this work can also serve as the basis for deriving the constitutive models for three-dimensional microtruss structured materials. These three dimensional structures should be space filling to be able to be used to generate a tessellation of space. One of the examples of these structures is R. Buckminster Fuller's octet-truss (Fuller, 1961). In his book Fuller writes: " Nature's simplest structural system in the universe is the tetrahedron. The regular tetrahedron does not fill all-space by itself. The octahedron and tetrahedron complement one another to fill all space. Together they provide the simplest, most powerful structural system in the universe..." Based on the patent of Fuller (1961), the "octet-truss" system represents a structure sustaining loads by axial deformations of the constituent members. The effective mechanical properties of the octet-truss have been investigated in the literature (Deshpande et al., 2001, Evans et al., 2001, Christensen, 2004, Mohr 2004). The methodology presented in this thesis work can be modified to fit a three-dimensional frame. By the use of an RVE composed of two tetrahedrons connected by an octahedron, a general large deformation constitutive model for the octet-truss can be developed.

Appendix

The derivatives related:

For member A:

$$\frac{\partial \lambda_A}{\partial F_{11}} = \frac{F_{11}}{\sqrt{\left(F_{11}^2 + F_{21}^2\right)}}$$

$$\frac{\partial \lambda_A}{\partial F_{12}} = \frac{F_{21}}{\sqrt{\left(F_{11}^2 + F_{21}^2\right)}}$$

$$\frac{\partial \lambda_A}{\partial F_{21}} = \frac{F_{21}}{\sqrt{\left(F_{11}^2 + F_{21}^2\right)}}$$

$$\frac{\partial \lambda_A}{\partial F_{22}} = \frac{F_{21}}{\sqrt{\left(F_{11}^2 + F_{21}^2\right)}}$$

For member B:

$$\frac{\partial \lambda_B}{\partial F_{11}} = \frac{1}{2}\left(F_{11} - F_{12}\sqrt{3}\right)^2 \left((F_{11} - F_{12}\sqrt{3})^2 + (F_{21} - F_{22}\sqrt{3})^2\right)^{-\frac{1}{2}}$$

$$\frac{\partial \lambda_B}{\partial F_{12}} = \frac{-\sqrt{3}}{2}\left(F_{11} - F_{12}\sqrt{3}\right)\left(\left(F_{11} - F_{12}\sqrt{3}\right)^2 + \left(F_{21} - F_{22}\sqrt{3}\right)^2\right)^{-\frac{1}{2}}$$

$$\frac{\partial \lambda_B}{\partial F_{21}} = \frac{1}{2}\left(F_{21} - F_{22}\sqrt{3}\right)\left(\left(F_{11} - F_{12}\sqrt{3}\right)^2 + \left(F_{21} - F_{22}\sqrt{3}\right)^2\right)^{-\frac{1}{2}}$$

$$\frac{\partial \lambda_B}{\partial F_{22}} = \frac{-\sqrt{3}}{2}\left(F_{21} - F_{22}\sqrt{3}\right)\left(\left(F_{11} - F_{12}\sqrt{3}\right)^2 + \left(F_{21} - F_{22}\sqrt{3}\right)^2\right)^{-\frac{1}{2}}$$

For member C:

$$\frac{\partial \lambda C}{\partial F11} = \frac{1}{2} * \left(F11 + F12\sqrt{3}\right)\left(\left(F11 + F12\sqrt{3}\right)^2 + \left(F21 + F22\sqrt{3}\right)^2\right)^{-\frac{1}{2}}$$

$$\frac{\partial \lambda C}{\partial F12} = \frac{\sqrt{3}}{2}\left(F11 + F12\sqrt{3}\right)\left(\left(F11 + F12\sqrt{3}\right)^2 + \left(F21 + F22\sqrt{3}\right)^2\right)^{-\frac{1}{2}}$$

$$\frac{\partial \lambda C}{\partial F21} = \frac{1}{2}\left(F21 + F22\sqrt{3}\right)\left(\left(F11 + F12\sqrt{3}\right)^2 + \left(F21 + F22\sqrt{3}\right)^2\right)^{-\frac{1}{2}}$$

$$\frac{\partial \lambda C}{\partial F22} = \frac{\sqrt{3}}{2}\left(F21 + F22\sqrt{3}\right)\left(\left(F11 + F12\sqrt{3}\right)^2 + \left(F21 + F22\sqrt{3}\right)^2\right)^{-\frac{1}{2}}$$

References

Ashby, M.F., Evans, A.G., Fleck, N.A., Gibson, L.J., Hutchinson, J.W., Wadley, H.N.G., 2000, *Metal Foams: A Design Guide,* Cambridge University Press, Cambridge.

Arruda, E.M., and Boyce, M.C., 1993, "A Three-dimensional Constitutive Model for the Large Stretch Behavior of Elastomers", J. Mech. Phys. Solids, **41**, pp.389-412.

Becker, W.M., Kleinsmith, L.J., and Hardin, J., 2000, *The world of the cell* , fourth ed., The Benjamin /Cummings Pub. Co., Inc.

Bell, G.I., 1978, "Models for the Specific Adhesion of Cells to Cells", Science, **200**, pp. 618-627.

Boal D., 2003, *Mechanics of the Cell, second ed.,* Cambridge University Press, Cambridge.

Boal, D.H., 1994, "Computer Simulation of a Model Network for the Erythrocyte Cytoskeleton", Biophys. J., **67**, pp. 521-529.

Boey, S.K., Boal, D.H., and Discher D.E., 1998, "Simulations of the erythrocyte cytoskeleton at large deformation, I. Microscopic models", Biophys. J., 75, pp. 1573-1583.

Boyce, M.C., 1996, "Direct Comparison of the Gent and the Arruda-Boyce Constitutive Models of Rubber Elasticity", Rubb. Chem.Tech., **69**, pp. 781-785.

Boyce, M.C., and Arruda, E.M., 2000, "Constitutive Models of Rubber Elasticity: A Review", Rubb. Chem. Tech., **73**, pp. 504-523.

Brittain, S.T., Sugimura, Y., Schueller, O.J.A., Evans, A.G., and Whitesides, G.M., 2001, " Fabrication and Mechanical Performance of a Mesoscale Space-Filling Truss System", J. Microelectromechanical Sys., **10**, 1, pp. 113-120.

Bustamante, C., Bryant, Z., Smith, B.S., 2003, “Ten years of tension: single-molecule DNA mechanics”, Nature, **421**, pp. 423-427.

Campbell, M., Sharp, D.N., Harrison, M.T., Denning, R.G. and Turberfield, A.J., 2000, "Fabrication of photonic crystals for the visible spectrum by holographic lithography", , Nature, **404**, pp. 53-56.

Chiras, S., Mumm, D.R., Evans, A.G., Wicks, N., Hutchinson, J.W., Dharmasena, K., Wadley, H.N.G., and Fitcher, S., 2002, “The Structural Performance of Near-Optimized Truss Core Panels”, Int. J. Sol. and Struct., **39**, 4093-4115.

Choi, T., Arslan, M., Jang, J.H., Pate, B.D., Lemieux, M.C., Tsukruk, V.V., Boyce, M.C., Thomas, E.L., 2005, “Ultra Lightweight Nanorelief Networks: Photopatterned Nanotrusses and Infiltrated Nanocomposites”, Poster, Institute for Soldier Nanotechnologies Day.

Christensen, R.M., 2004, “The three-dimensional analog of the classical two-dimensional truss system”, J. Appl. Mech., **71**, pp.285-287.

Dao, M., Lim, C.T., and Suresh, S., 2003, “Mechanics of the Human Red Blood Cell Deformed by Optical Tweezers”, J. Mech. Phys. Solids, **51**, pp. 2259-2280.

Deshpande, V.S., Fleck, N.A., and Ashby, M.F., 2001, “Effective properties of the octet-truss lattice material”, J. Mech. Phys. Sol., **49**, pp. 1747-1769.

Discher D.E., Boey, S.K, and Boal, D.H., 1997, “Phase transitions and anisotropic responses of planar triangular nets under large deformation”, Physical Review E **55**, 4, pp. 4762-4772.

Discher D.E., Boal, D.H., and Boey, S.K, 1998, “Simulations of the erythrocyte cytoskeleton at large deformation, II. Micropipette Aspiration”, Biophys. J., **75**, pp. 1584-1597.

Discher, D.E., and Carl, P., 2001, “New Insights into Red Cell Network Structure, Elasticity and Spectrin Unfolding- A Current Review”, Cell. Mol. Bio. Lett., **6**, pp. 593-606.

Easterling, K.E., Harrysson, R., and Gibson, L.J., 1982, "On the Mechanics of Balsa and Other Woods", Proc. R. Soc. Lond. A, **383**, pp. 31-41.

Evans, E.A., 1973, "A New Material Concept for the Red Cell Membrane", Biophys. J., **13**, pp. 926-940.

Evas, E.A., 1973, "New Membrane Concept Applied to the Analysis of Fluid Shear and Micropipet Deformed Red Blood Cells", Biophys. J., **13**, pp. 941-954.

Evans, E.A., and Hochmuth, R. M., 1977, "A Solid-Liquid Composite Model of Red Cell Membrane", J. Membrane Biol., **30**, pp. 351-362.

Evans, E.A., Skalak R., 1980, "Mechanics and Thermodynamics of Biomembranes", pp. 1-254, Boca Raton, Florida, CRC Press.

Evans, E.A., and Hochmuth, R.M., 1977, "A solid-liquid composite model of red cell membrane", J. Membrane Biol., **30**, pp. 351-362.

Evans, A.G., Hutchinson, J.W., Fleck, N.A., Ashby, M. F., and Wadley, H. N. G., 2001, "The Topological Design of Multifunctional Cellular Metals", Prog. In Mat. Sci., **46**, 309-327.

Evans, A.G., Hutchinson, J.W., Fleck, N.A., Ashby, M.F., and Wadley, H.N.G., 2001, "The topological design of multifunctional cellular materials", Prog. Mater. Sci., **46**, pp. 309-327.

Flory, P.J., 1953, *Principles of Polymer Chemistry,* Cornell University Press, Ithaca, New York.

Fung, Y.C., 1993, *Biomechanics: Mechanical Properties of Living Tissues*, second ed., Springer-Verlag, New York, Inc.

Fuller, R.B., 1961, *Octet Truss*, U.S. Patent Serial No. 2, 986, 241.

Fuller, R.B., 1983, *Inventions: The Patented Works of R. Buckminster Fuller*, St. Martin's Press, New York.

Furness, D.N., and Hackney C.M., 1990, "Comparative ultrastructure of subsurface cisternae in inner and outer hair-cells of the guinea-pig cochlea", European Archives of Oto-rhino-laryngology, **247** (1), pp. 12-15.

Gelse, K., Poschl, E., and Aigner, T., 2003, "Collagens: Structure, function and biosynthesis", Adv. Drug. Del. Rev., **55**, pp. 1531-1546.

Gibson, L.J., and Ashby, M.F., 1997, *Cellular Solids: Structure and Properties*, second ed., Cambridge University Press, Cambridge.

Gibson, L.J., and Ashby, M.F., 1982, "The Mechanics of Three-Dimensional Cellular Materials", Proc. R. Soc. Lond. A, **382**, pp. 43-59.

Gibson, L.J., Ashby, M.F., and Easterling, K.E., 1988, "Structure and Mechanics of the Iris Leaf", J. Mat. Sci., **23**, pp. 3041-3048.

Gibson, L.J., Ashby, M.F., Karam, G.N., Wegst, H.R. and Shercliff, H. R., 1995, "The Mechanical Properties of Natural Materials. II. Microstructures for Mechanical Efficiiency", Proc. R. Soc. Lond. A, **450**, pp. 141-162.

Gibson, L.J., Ashby, M.F., Schajer, G.S., and Robertson, C.I., 1982, "The Mechanics of Two-Dimensional Cellular Materials", Proc. R. Soc. Lond. A, **382**, pp. 25-42.

Gibson, L.J., Easterling, K.E., and Ashby, M.F. 1981, "The Structure and Mechanics of Cork", Proc. R. Soc. Lond. A, **377**, pp. 99-117.

Gibson, L. J., 2005, "Biomechanics of Cellular Solids", J. Biomech., **38**, pp. 377-399.

Hayes, W.C., and Carter, D. R., 1976, "Postyield Behavior of Subchondral Trabecular Bone", J. Biomed. Mat. Res. Symp., **7**, pp. 537-544.

Hochmuth, R.M., and Mohandas, N., 1972, "Uniaxial Loading of the Red-Cell Membrane" J. Biomech., **5**, pp. 501-509.

Izrailev, S., Stepaniants, S., Balsera, M., Oono Y., and Schulten, K., 1997, " Molecular Dynamics Study of Unbinding of the Avidin- Biotin Complex", Biophys. J., **72**, 1568-1581.

Jones, W.R., Ting-Beall, H.B., Lee, G.M., Kelley S.S., Hochmuth, R.M., Guilak F., 1999, "Alterations in the Young's Modulus and Volumetric Properties of Chondrocytes Isolated from Normal and Osteoarthritic Human Cartilage", J. Biomech., **32**, pp. 119-127.

Kuhn, W., and Grun, F., 1942, "Beziehungen zwischen elastischen Konstanten und Dehnungsdoppelbrechung hochelastischer Stoffe", Kolliod Z., **101**, pp. 248-271.

Law, R., Carl, P., Harper S., Dalhaimer P., Speicher, D., and Discher, D. E., 2003, "Cooperativity in Forced Unfolding of Tandem Spectrin Repeats", Biophys. J., **84**, pp. 533-544.

Lenne, P.F., Raae, A.J., Altmann, S.M., Saraste, M., Horber, J.K.H., 2000, " States and Transitions During Forced Unfolding of a Single Spectrin Repeat", FEBS Lett., **476**, pp. 124-128.

Liu, S., Derick, L.H. and Palek J., 1987, "Visualization of the Hexagonal Lattice in the Erythrocyte Membrane Skeleton", J. Cell Biol., **104**, pp. 527-536.

Marko, J.F., and Siggia, E.D., 1995, "Stretching DNA" Macromolecules, **28**, pp. 8759-8770.

Miller, D., and Benedek, G., 1973, *Intraocular light scattering: Theory and clinical application*, C.C. Thomas, Springfield.

Mills, J.P., Qie, L, Dao, M., Lim, C.T., and Suresh, S., 2004, "Nonlinear Elastic and Viscoelastic Deformation of the Human Red Blood Cell with Optical Tweezers", Mech. Chem. Biosystems, **1**, pp. 169-180.

Mohandas, N., and Evans, E., 1994, "Mechanical Properties of the Red Cell Membrane in Relation to Molecular Structure and Genetic Effects", Annu. Rev. Biophys. Biomol. Struct., **23**, pp. 787-818.

Mohr, D., 2005, "Mechanism-based multi-surface plasticity model for ideal truss lattice materials", Int. J. Sol. and Struct., **42**, pp. 3235-3260.
Nakamura, F., 2001, "Biochemical, electron microscobic and immunohistological observations of cationic detergent-extracted cells: detection and improved preservation of microextensions and ultramicroextensions", BMC Cell Bio., 2 (10).

Pascual J., Castresana J., and Saraste M., 1997, "Evolution of the spectrin repeat", Bioessays., **19**, 9, 811-817.

Picart, C., Dalhaimer, P., Discher, D. E., 2000, "Actin Protofilament Orientation in Deformation of the Erythrocyte Membrane Skeleton", Biophys. J., **79**, pp. 2987-3000.

Ponder, E., 1948, *Hemolysis and Related Phenomena*, Grune and Stretton, New York.

Qi H. J., Ortiz, C. and Boyce M.C., 2005, "Constitutive Model for the Stress-Strain Behavior of Biomacromolecular Networks Containing Folded Domains", Biophys. J., submitted.

Rief, M., Fernandez, J.M. and Gaub H.E. , 1998, "Elastically coupled two-level systems as a model for biopolymer extensibility", Phys. Review Lett., **81**, pp. 4764-4767.

Rief, M., Pascual, J., Saraste, M. and Gaub H.E., 1999, "Single Molecule Force Spectroscopy of Spectrin Repeats: Low Unfolding Forces in Helix Bundles", J. Mol. Biol., **286**, pp. 553-561.

Roper, E., Weinberg, W., Watt, F.M., and Land, H., 2001, "P19ARF- independent induction of p53 and cell cycle arrest by Raf in murine keratinocytes", EMBO Reports, **2**, pp. 145-150.

Skalak, R., Tozeren, A., Zarda, R.P. and Chien, S., 1973, "Strain Energy Function of Red Blood Cell Membranes", Biophys. J., **13**, pp. 245-264.

Treloar, L.R.G., 1958, *The Physics of Rubber Elasticity*, Oxford, Clarendon Press.

Ullal, C.K., Maldovan, M., Thomas E.L., Chen G., Han, Y., and Yang, S., 2004, "Photonic crystals through holographic lithography: Simple cubic, diamond-like, and gyroid-like structures", Appl. Phys. Lett., **84**, pp. 5434-5436.

Vajjhala, S., Kraynik, A.M., and Gibson, L.J., 2000, "A Cellular Model for Modulus Reduction due to Resorption of Trabeculae in Bone", J. Biomech., **122**, pp. 511-515.

Wallach, J.C., and Gibson, L.J., 2001, "Mechanical Behavior of a Three-Dimensional Truss Material", Int. J. Sol. and Struct., **38**, pp. 7181-7196.

Wicks, N., and Hutchinson, J.W., 2001, "Perfomance of Sandwich Plates with Truss Cores", Mech. Mater. **36**, 739-751.

Wicks, N., and Hutchinson, J.W., 2001, "Optimal Truss Plates", Int. J. Sol. and Struct., **38**, pp. 5165-5183.

Wintz, W., Everaers, R. and Seifert U., 1997, "Mesh Collapse in Two Dimensional Elastic Networks under Compression", J. Phys. I France, **7**, pp. 1097-1111.

Yang, S., Ullal, C.K., Thomas, E.L., Chen, G., and Aizenberg, J., 2005, "Microlens arrays with integrated pores as a multipattern photomask" Applied Physics Letters, **86**, pp. 201121,1-3.